

INVESTIGATION OF THE DYNAMICS
OF RADIATION FRONTS

by

WILLIAM W. ZUZAK

B.E. (Eng.Sc.Phys.) University of Saskatchewan, 1963

M.Sc., University of Saskatchewan, 1965

A THESIS SUBMITTED IN PARTIAL FULFILMENT OF
THE REQUIREMENTS FOR THE DEGREE OF

DOCTOR OF PHILOSOPHY

in the department

of

PHYSICS

We accept this thesis as conforming to
the required standard

THE UNIVERSITY OF BRITISH COLUMBIA

August, 1968

In presenting this thesis in partial fulfilment of the requirements for an advanced degree at the University of British Columbia, I agree that the Library shall make it freely available for reference and Study. I further agree that permission for extensive copying of this thesis for scholarly purposes may be granted by the Head of my Department or by his representatives. It is understood that copying or publication of this thesis for financial gain shall not be allowed without my written permission.

Department of PHYSICS

The University of British Columbia
Vancouver 8, Canada

Date AUG 23, 1968

ABSTRACT

A theoretical investigation of steady radiation fronts was carried out for the experimentally realistic situation in which ionizing or dissociating radiation passes through a transparent window into an absorbing gas. It was shown that five different types of radiation fronts may occur depending on the ratio of photon flux to absorber density. It was possible to calculate the flow in each case provided the final temperature behind the radiation front was assumed. This final temperature may be calculated if the structure and all reactions within the radiation front are taken into account.

An analytic expression can be obtained if particle motion and recombination are neglected, and the radiation is assumed to be monochromatic. This ideal case corresponds closely to a weak R-type radiation front. A first order relativistic correction indicates that the width of the front decreases as the velocity of the front approaches the speed of light.

In an associated experiment, radiation fronts in oxygen and iodine were produced by an intense light pulse from a constricted arc. The experiment in iodine demonstrated the beginning of the formation of a radiation

front during the $10 \mu\text{sec}$ light pulse. Radiation induced shock waves were observed in oxygen after the decay of the light pulse. These Mach 1.1 shocks were considered theoretically as unsteady one-dimensional flow and were treated by the method of characteristics, which was modified to include the energy input. The agreement between the theoretical and experimental results was satisfactory.

TABLE OF CONTENTS

	page
Chapter 1 INTRODUCTION	1
1.1 The problem	1
1.2 An outline of the thesis	7
Chapter 2 BASIC EQUATIONS AND ASSUMPTIONS	9
2.1 The possible types of flow	9
2.2 Conservation equations for a dis- continuity in one-dimensional flow	13
2.3 Rarefaction waves in a one-dimensional flow	17
2.4 The equations of state	20
2.5 Estimation of the temperature behind the radiation front	23
Chapter 3 PROPERTIES OF STEADY RADIATION FRONTS	29
3.1 Idealized propagation of a radiation front	29
3.1.1 Case of one frequency and one absorption cross section, α	30
3.1.2 Case of black body radiation $F(\nu)$ and continuous absorption cross section, $\alpha(\nu)$	36
3.2 Relaxation of restrictions on particle motion and recombination	42
3.2.1 The coefficient, ξ	42
3.2.2 The energy input, $W/\rho v$	43
3.3 Weak R-type front	44
3.4 R-critical front	48
3.5 Weak D-type front preceded by a shock wave	52
3.5.1 General relations	53
3.5.2 Iterative procedure for calcula- tions	55

Table of Contents --Continued

	page
3.6 D-critical front preceded by a shock	59
3.7 M-critical front preceded by a shock	64
Chapter 4 THE STRUCTURE OF STEADY RADIATION FRONTS	69
4.1 Conservation equations of mass, momentum, and energy within the radiation front	70
4.2 Reactions within a radiation front	71
4.3 Special case of a dissociation front in oxygen	74
4.3.1 Conservation equations for absorbing particles	75
4.3.2 The rate of energy input per unit volume, $\mathcal{P}(x, t)$ $q(x, t)$	78
4.3.3 Calculation of the front structure	80
4.4 Concluding remarks on Chapters 2, 3 and 4	82
Chapter 5 THE BOGEN LIGHT SOURCE	85
5.1 Description of light source	86
5.2 Measurement of intensity	88
5.2.1 Absolute intensity at 5000 Å with discharge voltage at 3.0 kV	89
5.2.2 Intensity as a function of wavelength at 3.0 kV	92
5.2.3 Intensity as a function of discharge voltage	92
Chapter 6 EXPERIMENTS AND RESULTS	94
6.1 Beginning of formation of dissociation front in iodine	95
6.2 Shock fronts in oxygen	101
6.3 Attempts to measure ionization in the test chamber	107

Table of Contents -- Concluded

	page
Chapter 7 UNSTEADY ONE-DIMENSIONAL FLOW WITH ENERGY INPUT	108
7.1 Method of characteristics	109
7.1.1 Physical characteristics in Eulerian and Lagrangian co- ordinates	111
7.1.2 State characteristics	112
7.2 Method of finite differences	114
7.3 Application of the two methods to dis- sociate fronts in oxygen	116
7.3.1 Shock formation for time depend- ant radiation from Bogen source	117
7.3.2 Structure of a steady dissociation front	119
Chapter 8 SUMMARY AND CONCLUSIONS	120
Appendices	
A NUMERICAL CALCULATION OF A STEADY RAD- IATION FRONT IN OXYGEN	124
B SCALED DRAWINGS AND DATA FROM LITERATURE	125
C EQUATIONS FOR SPECIAL REACTION SCHEME	127
D METHOD OF CHARACTERISTICS AT FIXED TIME INTERVALS	132
E METHOD OF FINITE DIFFERENCES	139
REFERENCES	144

LIST OF FIGURES

Figure		page
1.1	Classification of conditions encountered by radiation fronts	4
1.2	Hypothetical experimental situation	5
2.1	Schematic representation of flow velocities for various values of F_0/N_0	11
2.2(a)	Steady discontinuities in an R-critical front	14
2.2(b)	Steady discontinuities in an M-critical front	14
2.3	Propagation of a rarefaction wave	19
3.1	Radiation front travelling in + x direction with velocity v_F	31
3.2	Plot of the radiation equations for various values of F_0/CN_0	35
3.3	Idealized radiation front in oxygen for black body radiation $F(\neq)$	40
3.4	Weak R-type radiation front	47
3.5	R-critical radiation front	51
3.6	Weak D-type radiation front preceded by a shock	58
3.7	D-critical radiation front preceded by a shock	63
3.8	M-critical radiation front preceded by a shock	68
4.1	Plot of velocities versus N_0/F_0	83
5.1	Schematic representation of light source	87
5.2	Light pulse from Bogen source	89
5.3	Experimental setup for absolute intensity measurements	90
5.4	Intensity of Bogen source as function of discharge voltage	93
6.1	Schematic representation of experiment with iodine	96
6.2	Typical oscilloscope traces for measurements in iodine	100

List of Figures -- Concluded

Figure		page
6.3	Increase in light intensity during time of light pulse	100
6.4	Schematic of experiment in oxygen	102
6.5	Oscilloscope traces of piezoelectric probe	105
6.6	Shock strength as function of d at 400 Torr oxygen	105
6.7	Velocity of shock at 400 Torr oxygen	106
7.1	Mach lines and path lines of characteristic net	109
7.2	Computer profiles, 1.0 atm	118
7.3	Computer profiles, 0.1 atm	118
7.4	Computer profiles, 0.01 atm (method of finite differences)	119
B.1	Scale drawing of Bogen light source	125
B.2	Iodine absorption cross sections (Rabinowitch and Wood (1936))	126
B.3	Oxygen absorption cross sections (Metzger and Cook (1964))	126
D.1	Calculation of an ordinary point D	132
E.1	Lagrangian mesh for finite difference calculations	139

LIST OF SYMBOLS

A list of the symbols which appear several times throughout the thesis is given below. Symbols used only in isolated instances and those appearing in the appendices are not listed.

a	velocity of sound defined by $a \equiv (gp/\rho)^{1/2}$
c	velocity of light
c_s	velocity of sound defined by $c_s = (\partial p/\partial \rho)_s^{1/2}$
D	dissociation energy
E	ionization energy
\mathcal{E}	internal energy per gram
F	$\equiv F(x,t) \equiv \int (F(\nu,x,t) d\nu)$, photon flux (eq'n (3.16))
F_0	$\equiv F(0,t)$
g	$\equiv h/\mathcal{E}$, the effective adiabatic exponent (eq'n (2.12))
G(t)	$\equiv F(x,t)/F'(x)$, the time dependance of the photon flux
h	enthalpy per gram; Planck's constant
i	subscript index
j	subscript index
k	recombination coefficient; Boltzmann's constant
k_d	collisional dissociation coefficient

List of Symbols -- Continued

k_{32}	three body recombination coefficient
m	mass
M	mass (usually O_2 molecule); third particle in 3 body recombination
N	$= N(x,t)$, particle density
N_0	particle density if no dissociation were present; $= N(x,0)$, particle density at time zero
p	pressure
q	$= q(x,t)$, rate of energy input per unit mass
Q_s	artificial viscosity (see eq'n 7.12)
t	time
T	temperature
u	particle velocity in lab frame of reference
v	particle velocity in frame of reference of the closest discontinuity
v_F	velocity of radiation front (eq'ns (3.2), (3.25'))
W	energy flux
x	Eulerian spatial co-ordinate
y	degree of dissociation
	Lagrangian spatial co-ordinate; (see eq'n (3.20))

List of Symbols -- Concluded

α	photoabsorption coefficient
γ''	isentropic exponent (see eq'n (2.7))
η	right flowing Mach line
κ	coefficient of thermal conductivity
λ	wavelength
μ	coefficient of viscosity
ν	frequency
ξ	left flowing Mach line; coefficient (see eq'n (1.1))
ρ	density
χ	ionization or dissociation energy
*	denotes a molecule in a vibrationally excited state

ACKNOWLEDGMENTS

The author wishes to acknowledge the stimulating supervision of Dr. B. Ahlborn for the past three years.

Special thanks are due to Dr. J. H. Williamson for his assistance in preparing the thesis and especially for suggesting the calculation procedure used in section 3.1.2. Finally, the author is indebted to Ricardo Ardila who carried out most of the measurements in section 6.2.

It has been a pleasure being associated with friendly and stimulating people comprising the Plasma Physics group at the University of British Columbia.

C H A P T E R I

INTRODUCTION

1.1 The Problem

In most plasmas produced in the laboratory, radiation is considered an undesirable energy loss mechanism, of interest only to spectroscopists for analysis of the conditions within the plasmas. However, absorption of radiation may be used to produce plasmas. This was first illustrated by Stromgren (1939) in his investigation of expanding H II regions in interstellar space. These H II regions are produced by a hot star emitting ionizing radiation into a rarified cloud of hydrogen atoms. Kahn (1954) and Axford (1961) have made extensive theoretical studies of the radiation fronts which presumably occur at the edges of these H II regions.

With the advent of the giant pulsed lasers, it has become possible to study radiation produced laser spark plasmas in the laboratory. Following the early work of Ramsden and Savic (1964) there has been a flood of investigations of the breakdown mechanisms and dynamics of these laser sparks. The absorption of the radiation in this case is of a special nature and does not correspond

to the single photon absorption mechanism. It is, therefore, perhaps, surprising that these laser sparks exhibit properties of detonations or Chapman-Jouguet waves which is a singular point on the manifold of radiation fronts which Kahn predicted to exist.

Let us consider the single photon absorption mechanisms which occur at the edge of a radiation produced plasma. When ionizing or dissociating radiation is incident upon an absorbing gas, a radiation front tends to form and propagate into the gas such that ahead of the front the gas is in its original state while behind it the gas is ionized or dissociated (i.e. a plasma). Behind the radiation front the gas is at a considerably higher temperature and there are more particles per unit mass than ahead of the front. The resulting pressure gradient across the radiation front may result in considerable motion of the plasma.

Most of the theoretical work in the literature on radiation fronts deals with interstellar H II regions and consequently, the equations used are expressly adopted for conditions found in interstellar space. One of these equations which is used by many workers is a relation between the particle density N_0 , the photon flux F_0 , and the velocity of the radiation front, v_F (e.g. Goldsworthy (1961)).

$$v_F = F_0/N_0$$

This relation assumes that each photon ionizes (or dissociates) exactly one particle and $v_F \ll c$, where c is the speed of light (see section 3.1). Since we wish to

consider recombination and collisional ionization, we introduce a coefficient, ξ , which is the average number of photons required to ionize one particle. (We shall consider this coefficient in more detail in section 3.2).

$$\text{We thus write } v_F \equiv \frac{F_0}{\xi N_0} \quad . \quad 1.1$$

The terminology in this thesis has been adopted from the definitive work of Kahn (1954): Supersonic radiation fronts which compress the gas weakly are called weak R-type fronts since they occur if the radiation front propagates into a Rarified gas. Subsonic radiation fronts which heat and expand the gas are called weak D-type fronts since they occur if the radiation front propagates into a Dense gas. Radiation fronts across which the flow switches from supersonic to subsonic are called strong R-type, whereas radiation fronts across which the flow switches from subsonic to supersonic are called strong D-type fronts. These only occur under very specialized conditions, and are not encountered for the conditions described in this thesis. In general, weak R-type radiation fronts occur when the ratio of radiation flux to particle density, F_0/N_0 is large compared to the speed of sound behind the radiation front and weak D-type fronts occur when this ratio F_0/N_0 is small. Conditions in the Middle between these two extremes where the ratio F_0/N_0 is of the order of the speed of sound of the gas behind the radiation front are referred to as M-type. The singular point which separates the M-type and weak R-type conditions is called R-critical and the point which separates the M-type and weak D-type conditions is called

D-critical. In both of these singular cases, the radiation fronts propagate at exactly sonic speed with respect to the gas behind them. This scheme is illustrated in Fig. 1.1 below.

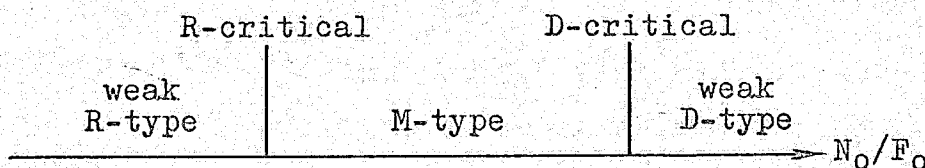


Fig. 1.1 Classification of conditions encountered by radiation fronts

The reader may be familiar with a classification of isolated discontinuities in the literature in which the relative velocity*, v , is compared with the local speed of sound, a . Using the subscripts 1 and 2 to refer to conditions ahead of and behind the radiation front respectively, this classification may be conveniently tabulated as follows:

	weak	critical	strong
D-type	$v_1 < a_1$ $v_2 < a_2$	$v_1 < a_1$ $v_2 = a_2$	$v_1 < a_1$ $v_2 > a_2$
R-type	$v_1 > a_1$ $v_2 > a_2$	$v_1 > a_1$ $v_2 = a_2$	$v_1 > a_1$ $v_2 < a_2$

In this thesis, we wish to make further theoretical and experimental investigations of the development and propagation of radiation fronts and phenomena associated with such fronts. For this purpose, we consider an experimentally realistic situation in which ionizing or dissociating radiation passes through a transparent window into a semi-infinite tube containing the absorbing gas. The boundary conditions for this situation permit unique solutions to be obtained. These experimental conditions differ from laser spark experiments in two ways. First,

* Measured in the frame of reference of the closest discontinuity.

the radiation front is considered in plane geometry. Secondly, the incident radiation may have any frequency distribution and is of long time duration.

Corresponding to this idealized experimental situation, let us consider a tube containing N_0 absorbers per unit volume with absorption cross section $\sigma(\nu)$, which are dissociated (we use the term dissociation generally to include ionization) by photons in the frequency interval ν_1 to ν_2 . At time $t = 0$, a steady parallel beam of F_0 photons/cm²sec in the interval ν_1 to ν_2 and with average energy $\langle h\nu \rangle$ is directed into the absorbing gas, see Fig. 1.2.

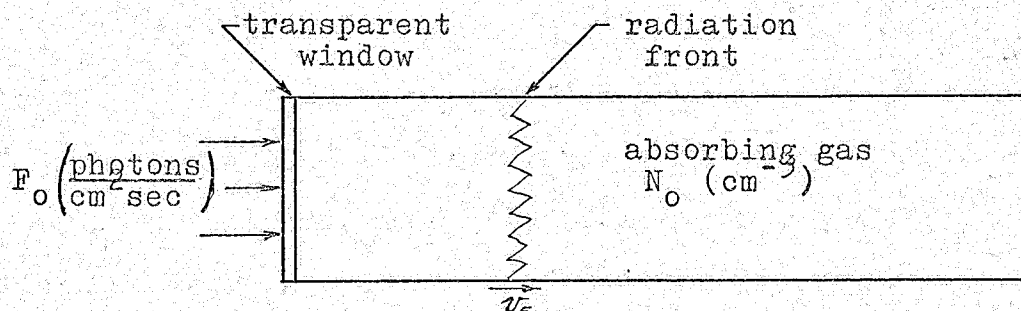


Fig. 1.2 Hypothetical experimental situation.

A radiation front will form and propagate away from the window into the undisturbed gas. According to eq'n (1.1) the velocity v_f of the front will be proportional to the ratio of the photon flux F_0 to the particle density N_0 of the absorbing gas. It is one aim of this thesis to show that the properties of the radiation front which develops depend critically upon the magnitude of $\frac{F_0}{N_0}$ compared with the speed of sound behind the front.

We feel that with the completion of this thesis, we have achieved three major points. First, it is now possible to predict the flow pattern for any value of F_0/N_0 in this experimental situation and (by assuming a reasonable temperature behind the radiation front) to calculate the velocities and thermodynamic quantities associated with the steady radiation front. This was not possible from the existing literature, where due to the lack of definite boundary conditions only general statements about the possible fronts had been obtained. Secondly, we have pointed out that the final temperature behind steady radiation fronts can (at least, in principle) be obtained from a detailed analysis of the structure of and mechanisms occurring within the radiation front. A knowledge of this temperature makes unique solutions possible. Thirdly, the experiments performed here, indicate the existence of radiation fronts in agreement with our theoretical investigations. For this, we have modified the theory of unsteady one-dimensional flow to include energy input. The method of characteristics at fixed time intervals or the method of finite differences may now be applied to predict the flow for any developing or unsteady radiation front and for any time varying photon flux, F_0 .

The main requirement for an experiment to observe radiation fronts in the laboratory is an extremely intense light source which radiates a large number of photons in the frequency interval in which the test gas has a high photoionization or photodissociation cross section and which radiates for as long a period of time as possible. Our light source was an arc which was forced to pass through a narrow channel in a polyethylene rod similar to that described by Bogen et al (1965). This source radiated with an effective black body temperature of the order of 10^5 °K for a period of 10 μ sec. Iodine and oxygen which have large photodissociation cross sections in the region 5000 Å and 1420 Å respectively were used as the absorbing gases.

1.2 An outline of the thesis

The thesis consists of two main sections: a theoretical investigation of steady radiation fronts and an experimental part.

In Chapter 2, we list the various steady radiation fronts which we expect to occur and then we develop the equations necessary to describe the flow for each case. There is always one more unknown than equations. Thus, in order to obtain unique solutions, it is either necessary to assume the final temperature behind the radiation front or to calculate the detailed structure of the front.

In Chapter 3, we carry out the calculations for a simplified model. Also, by assuming the final temperature, we calculate the flow for each of the cases which are expected to occur. In Chapter 4, we outline how to obtain the

detailed structure of a radiation front and the temperature behind it.

The radiation source is described in Chapter 5. Experiments and results are discussed in Chapter 6.

In order to understand details of the experimental results, in Chapter 7, we develop the theory of unsteady one-dimensional flow with energy input and apply it to the temporal development of the shock fronts observed experimentally.

The main results of the thesis are summarized in Chapter 8.

CHAPTER 2

BASIC EQUATIONS AND ASSUMPTIONS

Let us now consider in more detail, the experimental situation illustrated in Fig 1.2 for various values of F_0/N_0 .

2.1 The possible types of flow

We assume that after a certain length of time, a radiation front forms and that the flow associated with it approaches a steady state.* We then may treat the radiation front as a discontinuity across which the standard conservation equations of mass and momentum may be applied. The energy equation must be modified to include the radiant energy absorbed within the front. Thus, the problem may be treated as steady one-dimensional flow with energy input.

For values of F_0/N_0 either large or small compared with the speed of sound behind the radiation front, a_4 (we always use the subscript 4 to refer to quantities behind the radiation front) there is no difficulty in predicting the type of flow which will occur. For $F_0/N_0 \gg a_4$, the radiation front propagates so rapidly that the particles do not have an opportunity to react to the pressure

* This assumption is never strictly true; its validity will be discussed in section 2.5 and the following two chapters.

gradient across the front and consequently, there is only weak compression and little particle motion behind the front. At the other extreme, $F_0/N_0 \ll a_4$, the particles can, and do, react to the pressure gradient. The compression wave overtakes the radiation front and becomes a shock which propagates ahead of the radiation front. The radiation front in this case is an expansion wave since the gas entering it is in a compressed state and is heated and expanded as it passes through the front.

However, conceptual difficulties arise in the transition region where $F_0/N_0 \approx a_4$. Let us envisage what occurs as we decrease the radiation flux F_0 from a value at which $v_F = F_0/\rho N_0 \gg a_4$. The various cases are illustrated in Fig. 2.1. Initially, the radiation front will propagate supersonically with weak compression and little particle motion, as discussed above. Since there is a small drift velocity v_p imparted to the particles passing through the front a rarefaction wave will be set up (see Fig. 2.1) which eventually brings the particles to rest. The head of the rarefaction wave travels at the speed of sound relative to the particles entering ($v_H = v_p + a_4$), while the tail travels at the speed of sound of the stationary particles behind it ($v_T = a_5$, where the subscript 5 refers to quantities behind the rarefaction wave). Following Kahn (1954) we describe such a front as weak R-type (weak compression wave) followed by a rarefaction wave.

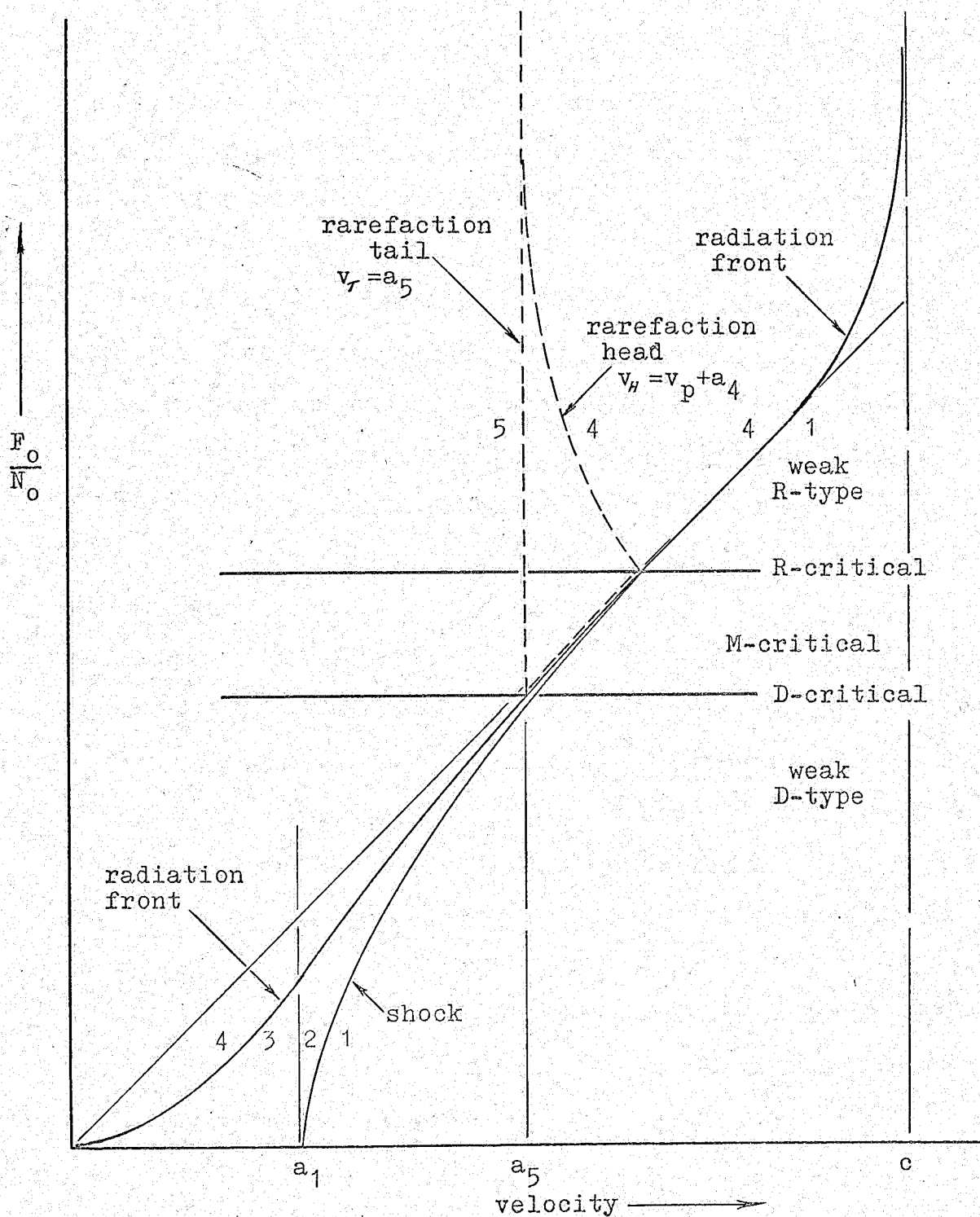


Fig. 2.1 Schematic representation of flow velocities for various values of F_0/N_0

As the incident radiation flux is decreased, we eventually reach a point where the front travels at the speed of sound relative to the gas behind it ($v_f = v_p + a_4$, where v_p is the particle drift velocity). The head of the rarefaction wave travels with the same speed and is in conjunction with the radiation front. This is called an R-critical front.

If the intensity of the incident radiation is decreased still further, a shock wave travels ahead of the front causing the gas between the shock and radiation front to be compressed and heated. The slower moving radiation front now enters a gas of higher density; the gas passing through the front is heated and expanded. We expect the rarefaction wave to follow the radiation front in the same manner as in the R-critical case. In this case, we adopt the terminology "M-critical front preceded by a shock wave".

As we further decrease the radiation intensity, the velocity of the radiation front decreases until it equals the velocity of the tail of the rarefaction wave. The rarefaction wave is thus merged with the radiation front. The front travels with the speed of sound, a_4 , relative to the gas behind it which itself is stationary in the lab frame of reference ($v_f = a_4$). This case is called a D-critical front preceded by a shock wave.

Finally, for still lower values of F_0 , we have the low velocity extreme $F_0/N_0 \ll a_4$, in which the radiation front

travels at subsonic speed relative to the stationary particles behind it ($v_F < a_4$) and a shock front propagates ahead of it. The discontinuities appear in the same order as for the D-critical case. We call this a weak D-type front preceded by a shock wave.

We note that in the above scheme, there are three regions of solution (weak R-type, M-critical, weak D-type) separated by two point solutions (R-critical and D-critical). Two other types of fronts, the strong R-type and strong D-type, which we mentioned previously and which are mentioned in the literature (Kahn (1954), Axford (1961)) do not occur in our case.

2.2. Conservation equations for a discontinuity in one-dimensional flow

We have assumed that the flow associated with the radiation front reaches a steady state such that the radiation front may be considered as a discontinuity across which the conservation equations of mass and momentum and the modified energy equation are valid. We label all quantities immediately behind the radiation front with the subscript 4, see Fig. 2.2, and the initial undisturbed quantities carry the subscript 1. Similarly, the subscript 2 refers to quantities behind the shock front and subscript 3 refers to quantities entering an M-critical, D-critical or weak D-type front. The thermodynamic

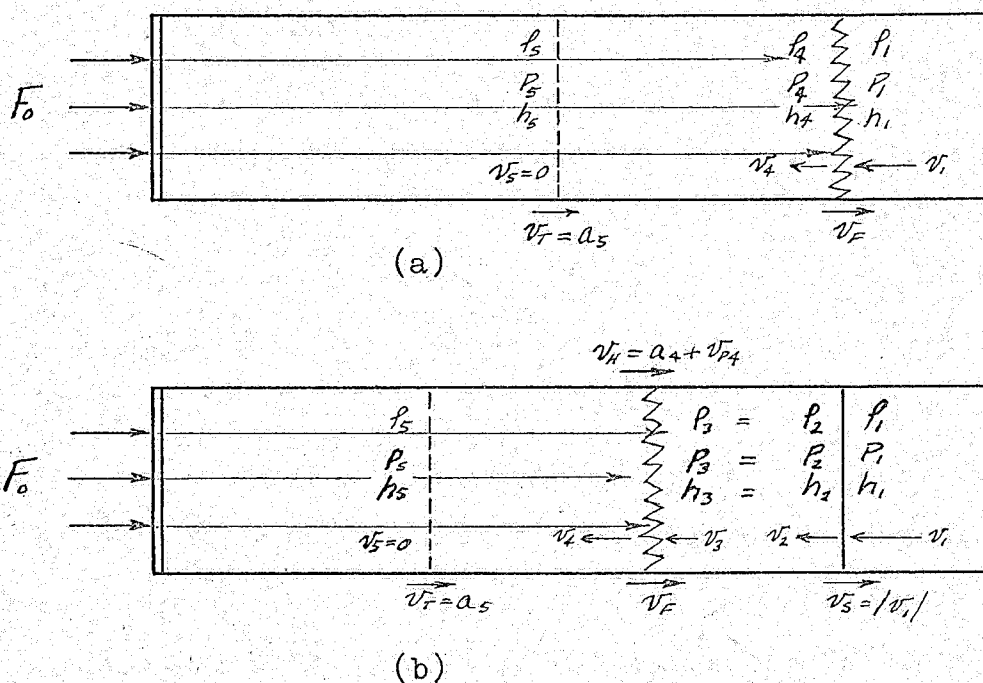


Fig. 2.2 (a) Steady discontinuities in an R-critical front
 (b) Steady discontinuities in an M-critical front

quantities with the subscripts 2 and 3 are assumed to be identical, the velocities v_2 and v_3 are, of course, different in their respective frames of reference.* If a rarefaction wave exists, the quantities behind it are labelled with the subscript 5.

In the frame of reference of the discontinuity, the conservation equations of mass, momentum and energy may be written as (e.g. for an R-critical or weak R-type front)

$$\rho_4 v_4 = \rho_1 v_1 \quad , \quad 2.1$$

$$\rho_4 v_4^2 + p_4 = \rho_1 v_1^2 + p_1 \quad , \quad 2.2$$

$$h_4 + \frac{1}{2} v_4^2 - \frac{v_1}{\rho_4 v_4} = h_1 + \frac{1}{2} v_1^2 \quad . \quad 2.3$$

* Compare footnote on page 4.

v (cm/sec) is the velocity of the gas particles relative to the discontinuity, ρ (gm/cm³) is the mass density, p (dynes/cm²) is the pressure, h (ergs/gm) is the enthalpy and W (ergs/cm²sec) is the energy flux which is absorbed by the gas. W is defined by

$$W \equiv F_0 \langle h v \rangle = \int_{V_1}^{V_2} h v F_0(v) dv \quad 2.4$$

We have neglected the radiation pressure in eq'n (2.2) since it is negligible for any cases that we consider.

With proper choice of the indices all discontinuities associated with the radiation front can be described by these conservation equations. For an M-critical, D-critical or weak D-type front, the indices on the right hand side of eq'ns (2.1) to (2.3) have to be changed to 3, (compare Figs 2.2(a) and 2.2(b)). For shocks which precede the radiation front, the quantities on the left hand side of these equations are labelled with the subscript 2 and the energy flux W is zero. These conservation equations, however, cannot be applied to rarefaction waves which are treated in the next section.

From these conservation equations and the equation of state, see section 2.4, it is possible to express the compression ratio in terms of an effective adiabatic exponent, g (Lun'kin(1959)). For an ideal gas g is analogous to the ratio of specific heats γ (see Zel'dovich and Raizer (1966), p 207). The value of g varies between 1.06 and 1.7 and often may be estimated quite accurately a priori.

Ahlborn and Salvat (1967) show the compression ratio (for an R-critical or weak R-type front) is

$$\frac{p_4}{p_1} = \frac{g_4}{g_4 - 1} \left(\frac{\frac{v_1^2}{2} + \frac{p_1}{2\rho_1}}{\frac{v_1^2}{2} + \frac{g_1}{g_1 - 1} \frac{p_1}{\rho_1} + \frac{W}{\rho_1 v_1}} \right) \left(1 \pm \sqrt{1 - \left(\frac{g_4^2 - 1}{g_4^2} \right) \frac{\left(\frac{v_1^2}{2} \right) \left(\frac{v_1^2}{2} + \frac{g_1}{g_1 - 1} \frac{p_1}{\rho_1} + \frac{W}{\rho_1 v_1} \right)}{\left(\frac{v_1^2}{2} + \frac{p_1}{2\rho_1} \right)^2}} \right)$$

2.5

where we have used the equation of state in the form $h = (g/g-1) (p/\rho)$ to eliminate the enthalpy from the energy equation (Lun'kin (1959)). Note that eq'n (2.5) has two roots signifying the mathematical possibility of two different compression ratios. The negative root corresponds to the weak R-type solution; the positive root corresponds to the strong R-type solution which does not occur in our case.

We have pointed out previously that for the critical cases (R, M and D-critical) the radiation front travels with the speed of sound, a_4 , relative to the gas behind it. We refer to the quantity a_4 as a thermodynamic speed of sound since it is defined as

$$a_4 \equiv (g_4 p_4 / \rho_4)^{\frac{1}{2}} \quad 2.6$$

Usually, the speed of sound, c_s , is defined by a differential along an isentrope

$$c_s^2 \equiv \left(\frac{\partial p}{\partial \rho} \right)_s \quad 2.7$$

For a polytropic gas ($\rho = \rho_0 \gamma^n$, where $\gamma \rightarrow g$) this equation

reduces to eq'n (2.6). In a plasma (e.g. behind a radiation front) the isentropic exponent γ is not, in general equivalent to the effective adiabatic exponent g (see Zel'dovich and Raizer (1966), p 207); however, it has been shown by Ahlborn (1966) that the approximate speed of sound given by eq'n (2.6) differs by less than 10% from more accurate calculations based on eq'n (2.7). In this thesis we will use the speed of sound as defined by eq'n (2.6).

With this definition of the speed of sound, the term inside the square root sign of eq'n (2.6) becomes identically zero for the three critical cases. This yields an extra relation and simplifies the solutions considerably.

2.3 Rarefaction waves in a one-dimensional flow

For the boundary conditions considered in this thesis fast radiation fronts are always followed by rarefaction waves. Though the properties of such waves are well known from the literature, for the convenience of the reader, we summarize the important facts in this section.

Consider a semi-infinite tube of gas closed at the left end, travelling in the $+x$ direction (i.e. to the right) with the speed v_p . At time $t = 0$, the tube comes to a complete stop. What is the motion of the gas at the left end?

This is the age old problem of Riemann and the

solution is well known (see von Mises (1958) or Courant and Friedrichs (1948)). A rarefaction wave is formed which causes the particles to decelerate through an expansion fan as illustrated in Fig. 2.3. The head of the rarefaction wave travels at the speed, $v_H = v_{p4} + a_4$ (where a_4 is the speed of sound in the gas in region 4); the tail of the wave travels at the speed, $v_T = a_5$. The expansion through the rarefaction fan occurs isentropically and it can be shown that in an isentropic expansion, the quantity $2a/(g-1) \cdot v$ is conserved at every point along the expansion (we use the effective adiabatic exponent g in place of the isentropic exponent γ). Thus we may write

$$\frac{2a_5}{g_5-1} - 0 = \frac{2a_4}{g_4-1} - v_{p4} \quad 2.8$$

For a polytropic gas the quantity $p \rho^{-g}$ is conserved; hence

$$p_5 \rho_5^{-g_5} = p_4 \rho_4^{-g_4} \quad 2.9$$

We now assume $g_5 = g_4 = g$ (an approximation which is not generally true for a plasma) and combine eq'ns (2.8) and (2.9) to obtain

$$\frac{p_5}{p_4} = \left(\frac{a_4 - \frac{g-1}{2} v_{p4}}{a_4} \right)^{\frac{2g}{g-1}} \quad 2.10$$

To obtain the temperature T_5 we use the relation

$$\frac{T_5}{T_4} = \frac{p_5}{p_4} \frac{\rho_4}{\rho_5} \frac{M_5}{M_4} \quad 2.11$$

where M_4 and M_5 are the initial and final molecular weights of the gas in regions 4 and 5.

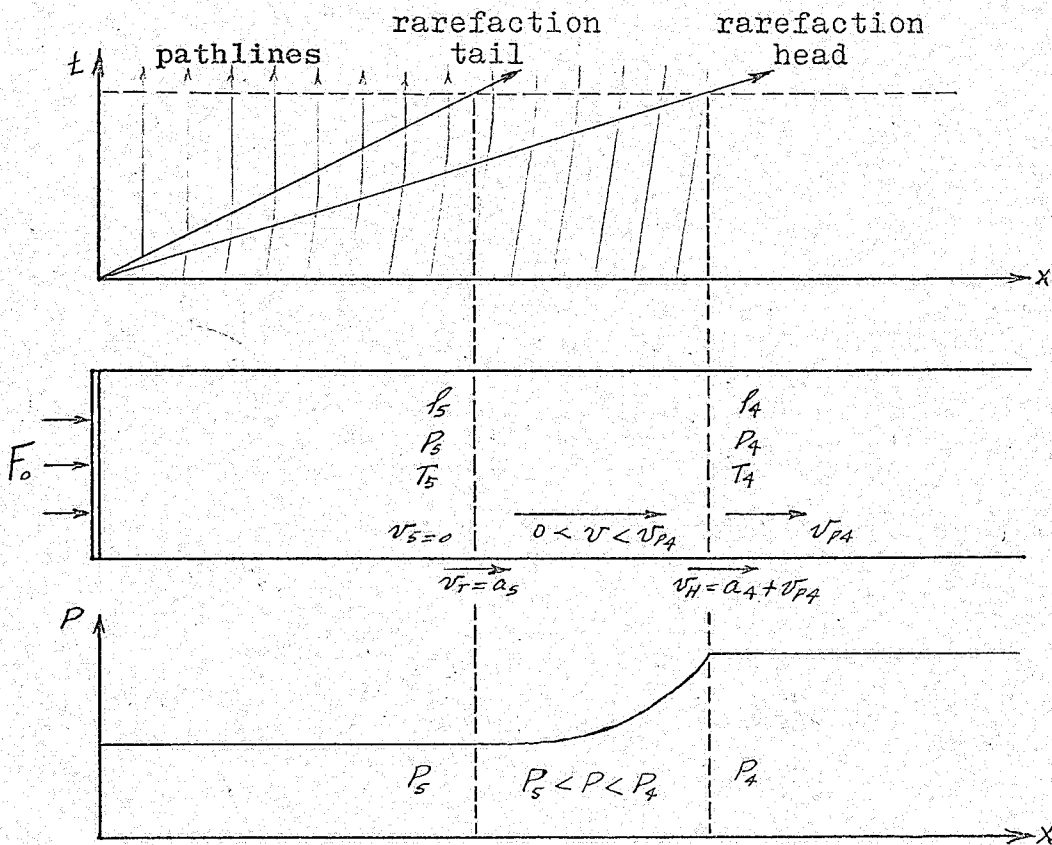


Fig. 2.3 Propagation of a rarefaction wave

We have tailored our treatment above to apply directly to the rarefaction fans which occur behind M-critical, R-critical and weak R-type radiation fronts. One may expect problems to arise when the assumption $\mathcal{E}_5 = \mathcal{E}_4$ is not valid and when g differs markedly from \mathcal{J}'' . If this occurs, one must use more accurate values and iterative techniques.

2.4 The equations of state

An equation of state relates the thermodynamic quantities such as the pressure, density, enthalpy, temperature, T , and internal energy, \mathcal{E} . Throughout this thesis, we find it convenient to use several different forms of the equation of state. We have already had occasion to use the equation which relates the enthalpy to the pressure and density by means of the effective adiabatic exponent, g ,

$$h = \frac{g}{g-1} \frac{P}{\rho} . \quad 2.12$$

Similarly, for the internal energy, \mathcal{E} , we may write

$$\mathcal{E} = \frac{1}{g-1} \frac{P}{\rho} , \quad 2.13$$

since $\mathcal{E} \equiv h - P/\rho$. We note that the temperature does not appear explicitly in these equations, however, the adiabatic exponent g is a weak function of temperature and pressure (or density). For a monatomic gas such as argon g varies from 1.67 at 300 °K to 1.13 at 20,000 °K; while for a diatomic gas such as oxygen it varies from 1.4 at 300 °K to 1.06 at 10,000 °K. Curves of $g(p, T)$ plotted versus T may be found for various gases in Ahlborn and Salvat (1966) and Kuthe and Neumann (1964). (See Zel'dovich and Raizer (1966), p 207 for a different approach.)

The pressure in a multicomponent plasma may be written as the sum of the partial pressures of the individual

components.

$$P = \sum_j P_j = \sum_j n_j k T_j \quad 2.14$$

where for a diatomic gas the index $j = m, a, e, i = 1, 2, 3, \dots$ refers to molecules, atoms, electrons and degree of ionization respectively, n_j is the particle density of the j^{th} component, T_j is the temperature associated with the translational degrees of freedom of the j^{th} component and k ($= 1.38 \times 10^{-16}$ ergs/°K molecule) is Boltzmann's constant.

The internal energy, \mathcal{E} , is defined to be the sum of the energies in the various degrees of freedom of all the components of the gas. For a diatomic gas \mathcal{E} (ergs/gm) may be written as

$$\mathcal{E} = \frac{\frac{3}{2} \sum_j n_j k T_j + \sum_{j \neq e} n_j k T_j^2 \frac{\partial}{\partial T_j} (\ln Z_j) + \frac{D}{2} (n_a + \sum_i n_i) + \sum_i E_i n_i}{\sum_j n_j m_j} \quad 2.15$$

where the quantities k , n_j and T_j are defined as in eq'n (2.14). m_j (gm) is the mass of the j^{th} component particle, D (ergs) is the dissociation energy of the diatomic molecule, E_i (ergs) is the ionization potential of the i^{th} stage of ionization and Z_j is the partition function of the j^{th} component excluding the electrons. (The term containing Z_j gives the energy in the vibrational and rotational states of the molecule and the excited electronic states of the atoms and ions.). The denominator of eq'n (2.15) is the mass density, $\rho = \sum_j n_j m_j$.

By combining eq'ns (2.14) and (2.15) it is possible to obtain an equation of the form of eq'n (2.13) and thus

obtain an explicit expression for the effective adiabatic exponent, g . To illustrate, let us consider the gas in a dissociation front in oxygen initially at room temperature. We assume that there is no ionization and we neglect the energy in the excited electronic states of the atoms and molecules. At room temperature, the rotational degrees of freedom of the molecules are in full excitation and contribute $n_m kT$ to the internal energy of the gas. The excitation of the vibrational degrees of freedom becomes appreciable at temperature larger than 1000 °K. Assuming the molecule vibrates as a harmonic oscillator the contribution to the internal energy is given by (see Zel'dovich and Raizer (1966), p 181)

$$\mathcal{E}_{vib} = n_m k \frac{(h\nu'/k)}{e^{h\nu'/kT} - 1}, \quad 2.16$$

where for oxygen $h\nu'/k = 2228$ °K. This expression assumes that the vibrational degrees of freedom are in complete equilibrium with the translational degrees of freedom.

We may thus write eq'n (2.15) as

$$\mathcal{E} = \frac{(\frac{5}{2} + \frac{1}{2}y)kT + (1-y) \frac{h\nu'}{e^{h\nu'/kT} - 1} + yD}{M}, \quad 2.15'$$

where M is the mass of the oxygen molecule ($M = n_m = 2m_a$) and where the degree of dissociation y is defined as

$$y = \frac{\frac{1}{2}n_a}{n_m + \frac{1}{2}n_a}. \quad 2.17$$

Similarly, eq'n (2.14) may be written as

$$p = (1+y) \rho \frac{kT}{M}, \quad 2.14'$$

where $f = n_a m_a + n_m m_m = (n_m + \frac{1}{2} n_a) M$.

Combining eq'ns (2.14') and (2.15') we obtain an expression for \mathcal{E} in the form

$$\mathcal{E} = \left[\frac{(\frac{5}{2} + \frac{1}{2} \gamma) + (1 - \gamma) \left(\frac{h \nu'}{kT} \right) (e^{h \nu'/kT} - 1)^{-1} + \gamma \left(\frac{D}{kT} \right)}{1 + \gamma} \right] \frac{P}{P} \quad 2.13'$$

where the term in the square brackets corresponds to $(g-1)^{-1}$ of eq'n (2.13). We note that in our simplified example g is a function of temperature and the degree of dissociation γ only. In general, one should also include the degree of ionization and invoke equilibrium relations or rate equations to relate the various particle concentrations.

2.5 Estimation of the temperature behind the radiation front

Let us consider a non-relativistic weak R-type front across which the conservation equations (2.1) to (2.3) can be applied. If we assume that the rate of energy input W is known, then these three equations plus an equation of state and an equilibrium relation* give us five equations with six unknowns $v_1, v_4, \rho_4, p_4, h_4, T_4$. (One may argue that $v_1 = v_f$ is known from eq'n (1.1); however, this is no help since then the coefficient ξ is unknown.) Similarly, if we consider any other type of front we always have one more unknown than equations. We must, therefore, obtain a further specifying equation or fix a parameter

* for the particle concentrations,

to solve the problem.

In order to obtain the specifying equation, one must be able to calculate in detail the state of the particles as they pass through the radiation front. It is also necessary to know the detailed structure of the discontinuity. In general, this is a formidable task since one must consider the reaction rates occurring in the front, collision and excitation cross sections, transition probabilities, energy transfer by means of radiation and so forth. In addition to the obvious complexity, we have a further problem in that quantitative values of many of the reaction rates, etc. are either inaccurate or unknown.

For the present, we will not attempt to obtain the structure of the radiation front but will, instead, show how to estimate or give limits for the final temperature, T_4 , behind the radiation front. A first order approximation to the temperature behind the radiation front may be obtained by considering the energy equation (2.3). If we consider a dissociation front entering a diatomic gas at room temperature, the enthalpy h_1 is given by $h_1 = 3.5 kT_1/M$, where M is the mass of the molecule. The enthalpy behind the front is given by $h_4 = (5kT_4 + D)/M$ where D is the dissociation energy and where we assume complete dissociation but no ionization. In section 3.2 we will show that the term $W/\rho_1 v_1$ may be written

$$\frac{W}{\rho_1 v_1} = \xi \frac{\langle h_1 \rangle}{M}, \quad 3.29'$$

Thus eq'n (2.3) becomes

$$3.5 kT_1/M + \frac{1}{2}v_1^2 + \xi \langle h\nu \rangle / M = (5k T_4 + D)/M + \frac{1}{2}v_4^2$$

which may be solved for the end temperature T_4 behind a dissociation front

$$kT_4 = \frac{3.5 kT_1 + \xi \langle h\nu \rangle - D + \frac{1}{2} M (v_1^2 - v_4^2)}{5} \quad 2.18$$

The corresponding temperature for an ionization front is

$$kT_4 = \frac{2.5 kT_1 + \xi \langle h\nu \rangle - E + \frac{1}{2} m_a (v_1^2 - v_4^2)}{5} \quad 2.18'$$

where E is the ionization energy and m_a is the mass of the atoms. From eq'ns (1.1) and (2.18) or (2.19') it is evident that values of ξ and v_4 are required to calculate the final temperature.

One can expect the temperature to be between relatively narrow limits. For a dissociation front the equilibrium temperature behind the discontinuity must be larger than some minimum temperature, T_{\min} , at which virtually all the particles are dissociated (for example, we arbitrarily assume that "virtually all" is 99.8%). For an ionization front the equilibrium temperature* behind the discontinuity must be at least such that all the particles are still ionized after passing through the rarefaction wave.

* In fact, even if radiation losses from the plasma behind the discontinuity are ignored, an equilibrium temperature cannot be reached since there is a finite probability of particles recombining even at extremely high temperatures. On the other hand, if radiation losses are considered, then it is not possible for the radiation front and the flow associated with it to reach a steady state unless (perhaps) the radiation flux increases in time in some special way. Nevertheless, the concept of an equilibrium temperature is necessary in the "steady state" approximation of radiation fronts.

For a dissociation front in oxygen at atmospheric pressure, we choose* $T_{\min} = 6000$ °K at which temperature only 0.2% of the gas is in molecular form and 0.005% is ionized (Landolt-Börnstein II.4, p 717).

On the other hand, we can define another temperature, T_{\max} . This temperature is that value of T_4 which one obtains from eq'n (2.18) for a weak R-type front with $v_1 = v_4$ and $\xi = 1$. As an example, let us consider a dissociation front produced by 1420 \AA (8.8 eV) photons entering a cloud of oxygen molecules which have a dissociation energy of 5.1 eV. In this case, $T_{\max} \approx 8900$ °K.

If the photon flux F_0 is extremely high (such that $F_0/N_0 \gg a_4$), the weak R-type front travels so rapidly that there is little compression ($v_4 = v_1$) and there is little time for the hot dissociated atoms to dissociate other molecules in collisions. Also, at a temperature of 8900 °K, one could expect little recombination. Thus one photon dissociates only one molecule, such that $\xi = 1$. In this case, we expect the temperature behind the radiation front to be $T_{\max} = 8900$ °K.

If the intensity of the 8.8 eV radiation is relatively low (such that $F_0/N_0 \ll a_4$) we shall obtain a weak D-type front preceded by a shock. In this case, although there is a large expansion (such that $v_4 \gg v_3$) the term $(v_3^2 - v_4^2)$ is small compared with $\xi \langle h\nu \rangle - D$ in eq'n (2.18). Also, there is plenty of time for the hot dissociated

* For convenience of calculation we assume the temperature behind the radiation front, T_4 , rather than the temperature behind the rarefaction wave, T_5 . This assumption is of little consequence since the temperature drop across the rarefaction wave is small.

particles to cool by colliding with and dissociating other molecules. Thus, one photon will dissociate more than one molecule such that $\xi < 1$. In this case we expect $T_4 \rightarrow T_{\min} = 6000 \text{ }^\circ\text{K}$.

For intermediate values of F_0 (such that $F_0/N_0 \approx a_4$) for which we obtain D, M or R-critical fronts, the situation is more uncertain. In this case, the term $(v_3^2 - v_4^2)$ or $(v_1^2 - v_4^2)$ is appreciable. Collisions in the radiation front result in both dissociation and recombination. If three body recombination is predominant over collisional dissociation, then $\xi > 1$ and we expect $T_4 > T_{\max}$. If collisional dissociation is predominant over recombination, then $\xi < 1$ and we expect $T_{\min} \leq T_4 < T_{\max}$. Unfortunately, there seems to be no criteria by which one could predict the relative importance of collisional dissociation and three body recombination within the front.

As another idealized example, consider radiation at 912 \AA entering a gas of hydrogen atoms with an ionization potential of 13.6 eV. There is no excess energy of the ionization $\langle h\nu \rangle - E \approx 0$ such that $T_{\max} = \frac{1}{2} T_1 \ll T_{\min}$ and, therefore, on the average, one would require substantially more than one photon (i.e. $\xi > 1$) to ionize one atom and heat the gas to a minimum temperature of the order of 10,000 $^\circ\text{K}$.

The results of this section may be summarized as follows:

$$\begin{array}{ll}
 T_4 = T_{\max} & \text{if } \langle h\nu \rangle - \chi > kT_{\min}, F_0/N_0 \gg a_4, \xi = 1 \\
 T_4 = T_{\min} & \text{if (i) } \langle h\nu \rangle - \chi < kT_{\min}, F_0/N_0 \text{ arbitrary, } \xi > 1 \\
 & \text{or (ii) } \langle h\nu \rangle - \chi > kT_{\min}, F_0/N_0 \ll a_4, \xi < 1
 \end{array}$$

$$\begin{aligned}
 T_{\min} \leq T_4 < T_{\max} & \quad \text{if} \quad \langle h\nu \rangle - \chi > kT_{\min}, F_0/N_0 \approx a_4, \xi < 1 \\
 T_4 > T_{\max} & \quad \text{if} \quad \langle h\nu \rangle - \chi > kT_{\min}, F_0/N_0 \approx a_4, \xi > 1
 \end{aligned}$$

where χ is the dissociation energy for a dissociation front and the ionization energy for an ionization front.

CHAPTER 3

PROPERTIES OF STEADY RADIATION FRONTS

In the discussion of radiation fronts in a gas filled tube closed on one side by a transparent window, we postulated the existence of five different types of radiation fronts assuming that the flow in each case would reach a steady state. We also developed the equations which will enable us to calculate the thermodynamic properties and the flow velocities of the gas for each of the five types. For this calculation, we must make two assumptions. First, we assumed that the flow is steady in every case (we consider a rarefaction wave with its head and tail both travelling at constant but different speeds as being a steady state situation). Secondly, we assume the temperature, T_4 , is known (either by assumption or by a calculation of the detailed structure of the front).

3.1 Idealized propagation of a radiation front

In our hypothetical situation, the dissociating radiation of F_0 photons/cm²sec passes through a transparent window into a semi-infinite tube containing N_0 absorbing particles per unit volume. Let us now make the further assumptions that all particles are stationary and that

there is no recombination of the dissociated particles, such that there is a 1:1 correspondence between photons absorbed and absorbers depleted. (We assume that the dissociated particles are transparent to the incoming radiation.) It turns out that this situation is closely approximated by a supersonic (weak R-type) radiation front.

After a sufficient length of time, we expect the radiation front which forms and propagates down the tube with velocity v_f to approach a steady state. Let us consider such a steady front for the case where the radiation F_0 consists of photons of one frequency and also for the case of black body radiation $F(\nu)$ with absorption cross sections $\propto(\nu)$.

3.1.1 Case of one frequency and one absorption cross section, \propto .-- The diagrams in Fig. 3.1 illustrate the radiation front as a discontinuity on one side of which there are only absorbers and no photons and on the other side of which there are photons but no absorbers. In the lab frame of reference $F_0/c = \mathcal{N}_0$ photons/cm³ travelling with the speed of light, c , enter a stationary gas of N_0 absorbers/cm³. The velocity of the front is v_f . We may make a Lorentz transformation into the frame of reference in which the front is stationary. Following Schwarz (1964), p 392, and considering the photons as a flux of relativistic particles, we find the flux of atoms entering from the right is $-\gamma v_f N_0$ (absorbers/cm²sec), while the flux of photons

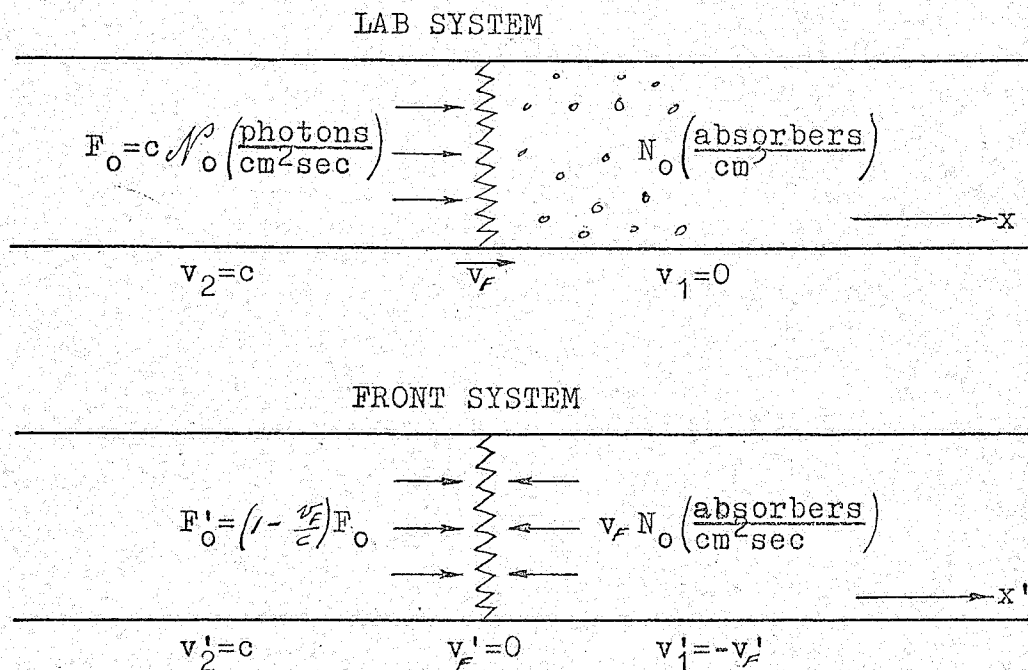


Fig. 3.1 Radiation front travelling in $+x$ direction with velocity v_F .

entering the front from the left is $F'_0 = \gamma(1 - v_F/c)F_0$ (photons/cm²sec), where $\gamma \equiv (1 - v_F^2/c^2)^{-\frac{1}{2}}$.

Equating the photon flux to the particle flux, we obtain

$$\gamma(1 - v_F/c) F_0 = \gamma v_F N_0, \quad (3.1)$$

which may be solved for v_F to give

$$v_F = \frac{F_0/N_0}{1 + F_0/cN_0} \quad [\text{cm/sec}]. \quad (3.2)$$

We note that for very high intensities such that $F_0/N_0 \gg c$, the front velocity approaches the speed of light as we expect ($v_F \rightarrow c$). For low intensities such that $F_0/N_0 \ll c$, we obtain the expected non relativistic relation, $v_F = F_0/N_0$.

Since the photoabsorption cross section is not infinite, the radiation front will have a finite thickness. The intensity $F(x)$ of the radiation at any point within the front will vary from F_0 at the extreme left to zero at the extreme right. Similarly, the absorber density $N(x)$ varies from N_0 at the extreme right to zero at the extreme left. We define the position of the front to be the point where $F(x)/F_0 = \frac{1}{2} = N(x)/N_0$. By equating the number of absorbers depleted in an interval of length Δx to the number of photons absorbed in the interval, we obtain*

$$\left(1 - \frac{v_F}{c}\right) \frac{\partial F(x)}{\partial x} = -N_F \frac{\partial N(x)}{\partial x} \quad 3.3$$

Substituting for v_F from eq'n (3.2), eq'n (3.3) becomes

$$\frac{F(x)}{F_0} + \frac{N(x)}{N_0} = \text{constant} = 1 \quad 3.4$$

The usual exponential decay equation in the lab frame of reference, $F(x,t) = F_0 \exp(-\alpha N x)$, should be generalised in our case to be

$$F(x,t) = F_0 \exp\left(\frac{-\alpha \int_0^x N(x',t) dx'}{1 - v_F/c}\right), \quad 3.5$$

since the number of absorbers N is a function of position, x , and time, t . Also, the source is moving away from the front with velocity $-v_F$ so, in general, we must include the first order correction,* $F' = (1 - v_F/c)F$. Thus instead of the usual differential equation for exponential decay

* Since we are not particularly interested in the relativistic regime we now and in the following equations assume $\gamma = 1$.

$\partial F(x)/\partial x = -\alpha N F(x)$, we must write

$$\left(1 - \frac{v_F}{c}\right) \frac{\partial F(x,t)}{\partial x} = -\alpha N(x,t) F(x,t) \quad , \quad 3.6$$

which by virtue of eq'ns (3.2) and (3.4) becomes

$$\frac{\partial F}{\partial x} = \left(1 + \frac{F_0}{cN_0}\right) (-\alpha N F) = -\left(1 + \frac{F_0}{cN_0}\right) \alpha N_0 \left(1 - \frac{F}{F_0}\right) F \quad . \quad 3.7$$

This differential equation is readily solved by separation of variables using the transformation $u = (F/F_0)$ and then

$$y = u - 1: \quad \int \frac{dy}{y} = \alpha N_0 \left(1 + \frac{F_0}{cN_0}\right) \int dx \quad ,$$

$$\ln(y/y_0) = \alpha N_0 \left(1 + \frac{F_0}{cN_0}\right) x$$

or, retransforming

$$\frac{F(x,t)}{F_0} = \frac{1}{1 + y_0(t) \exp(\alpha N_0 (1 + \frac{F_0}{cN_0}) x)} \quad , \quad 3.8$$

where the proportionality constant $y_0(t)$ can still be a function of time.

So far, we have ignored the time variable. Since this steady wave must necessarily satisfy the wave equation

$$\frac{\partial^2 F(x,t)}{\partial x^2} = \frac{1}{v_F^2} \frac{\partial^2 F(x,t)}{\partial t^2}$$

the function $y_0(t)$ may be evaluated.

A solution which satisfies the wave equation and the boundary conditions

$$\frac{F(x,t)}{F_0} = \begin{cases} 1 & , \text{ for } x \rightarrow -\infty, t \rightarrow -\infty \\ \frac{1}{2} & , \text{ for } x = 0, t = 0 \\ 0 & , \text{ for } x \rightarrow +\infty, t \rightarrow \infty \end{cases} \quad 3.9$$

is

$$\frac{F(x,t)}{F_0} = \frac{1}{1 + e^{\alpha N_0 (1 + \frac{F_0}{cN_0}) x - \alpha F_0 t}} \quad . \quad 3.10$$

From eq'ns (3.4) and (3.10) we obtain the particle density

$$\frac{N(x,t)}{N_0} = \frac{1}{1 + e^{-\alpha N_0 (1 + \frac{F_0}{cN_0}) x + \alpha F_0 t}} \quad 3.11$$

These two equations will hereafter be referred to as the "radiation front equations." Eq'ns (3.10) and (3.11) are derived for an ideal case but they correspond closely to a weak R-type front which has little particle motion and no recombination.

(i) Thickness of an ideal radiation front. -- We define the thickness of radiation front, δx as the distance between the points where F/F_0 is 0.9 and 0.1. Using these values in eq'n (3.10) we obtain

$$\delta x \equiv (x_{0.1} - x_{0.9}) = \frac{2 \ln 9}{2N_0(1+F_0/cN_0)} = \frac{4.40}{2N_0(1+F_0/cN_0)} \quad \cdot \quad 3.12$$

We note that for high intensities and low particle densities, such that $F_0/N_0 \gg c$, the width of the front is inversely proportional to the intensity F_0 . In this case, the front travels with the speed of light. Conversely for low intensities and high particle densities such that $F_0/N_0 \ll c$, the width of the front is inversely proportional to the particle density N_0 . The front speed is given by the ratio F_0/N_0 .

These dependencies are illustrated in Fig. 3.2 in which F/F_0 and N/N_0 of eq'ns (3.10) and (3.11) are plotted versus x/N_0 for $F_0/cN_0 = 0, 1$ and 10 , and for $t = 0$.

(ii) Typical values. -- Radiation fronts occur under extremely varied conditions. The high intensity, low density extreme is illustrated by ionization fronts associated with H II regions in interstellar space. In this case, a star radiates photons at wavelengths below 912 Å into a cloud of hydrogen atoms. Typical values are

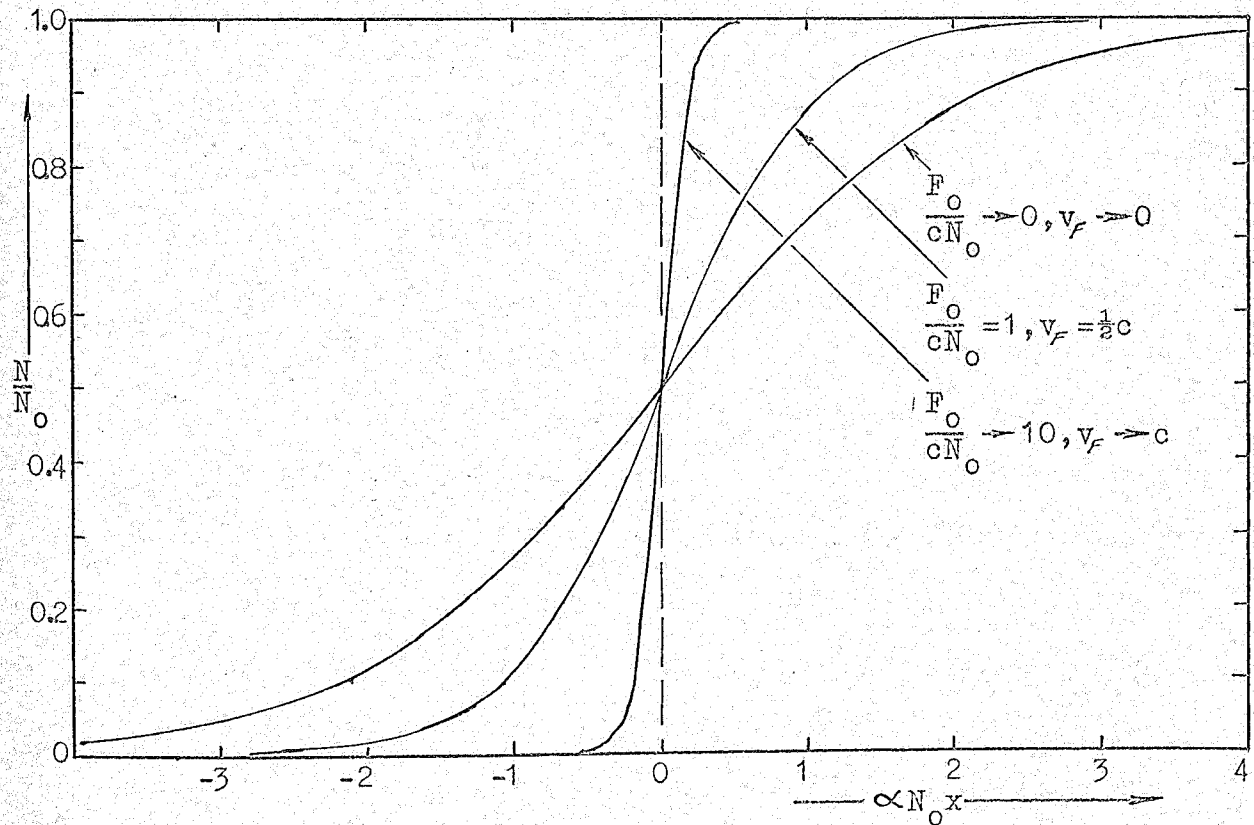
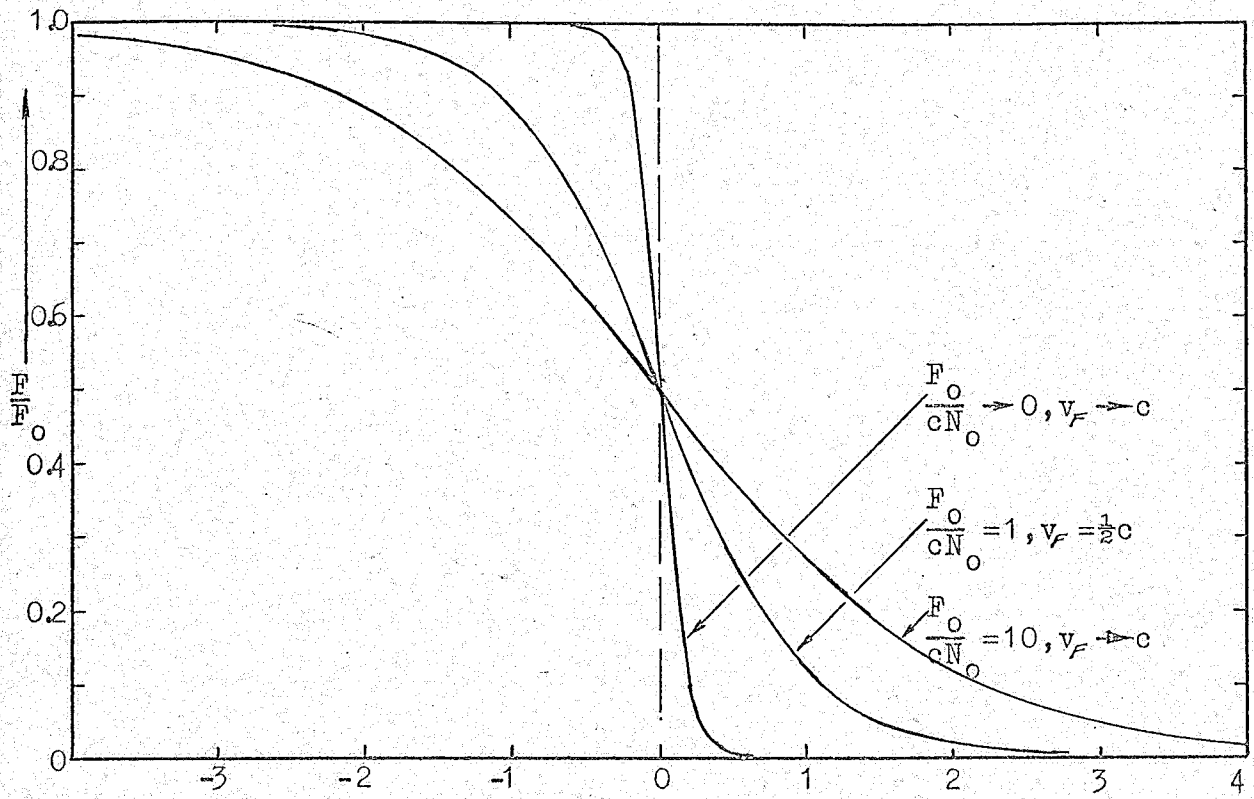


Fig.3.2 Plot of the radiation equations for various values of $\frac{F_0}{cN_0}$

$N_O = 10 \text{ cm}^{-3}$, $F_O = 10^{20} \text{ cm}^{-2} \text{ sec}^{-1}$ and photoionization cross section for hydrogen at 912 \AA , $\alpha_H = 6.3 \times 10^{-18} \text{ cm}^2$. This ionization front, if it satisfies the assumptions made in this section, would travel with the speed of light and have a width of $2 \times 10^8 \text{ cm}$.

Our own experiment described later in this thesis, in which photons in the 1400 \AA wavelength region dissociate oxygen molecules is an example of the low intensity, high density extreme. Here, typical values are $N_O = 10^{19} \text{ cm}^{-3}$, $F_O = 10^{22} \text{ cm}^{-2} \text{ sec}^{-1}$ and the photodissociation cross section $\alpha_{O_2} = 15 \times 10^{-18} \text{ cm}^2$. Thus (neglecting recombination, etc.) the dissociation front should travel at 10^3 m/sec and have a width of 0.03 cm .

3.1.2 Case of black body radiation $F(\nu)$ and continuous absorption cross section $\alpha(\nu)$. -- Most radiation sources which are available in the laboratory or which occur in nature have a continuous spectrum over a wide range of frequencies. Furthermore, the absorption cross section $\alpha(\nu)$ of the absorbing gas varies widely over the frequency spectrum. Eq'n (3.12) indicates that the width of the radiation front is inversely proportional to the absorption cross section. For example, if at the maximum absorption cross section α_m at some frequency ν_m the thickness of the radiation front is 1 cm , then at some frequency where α is $0.01 \alpha_m$ the thickness will be 100 cm . Thus, it is often necessary to ignore the absorption cross section outside a chosen frequency region. A good rule of thumb is to consider only photons

with absorption cross sections in the range $\alpha_m \leq \alpha(\nu) \leq 0.1\alpha_m$.

The differential equations may be set up in a manner similar to the preceding subsection. We pick two frequencies ν_1 and ν_2 between which the absorption cross section is finite and outside of which it is negligible. (We assume the gas is transparent to photons with frequencies outside this region. In general, this is not the case and it is necessary to consider several such frequency intervals). The total number of photons contributing to the front is

$$F_0 = \int_{\nu_1}^{\nu_2} F(\nu) d\nu \quad . \quad 3.13$$

The velocity of the front is again given by eq'n (3.2). The equation corresponding to eq'n (3.3) is

$$\left(1 - \frac{v_F}{c}\right) \frac{\partial}{\partial x} \left(\int_{\nu_1}^{\nu_2} F(\nu, x) d\nu \right) = -v_F \frac{\partial N(x)}{\partial x} \quad , \quad 3.14$$

such that again

$$\int_{\nu_1}^{\nu_2} \frac{F(\nu, x) d\nu}{F_0} + \frac{N(x)}{N_0} = 1 \quad , \quad 3.15$$

where we emphasize that this equation is valid across a steady radiation front propagating at a velocity v_F .

Corresponding to eq'n (3.5) and (3.6) we may write in the frame of reference of a semi-infinite tube with a transparent window at $x = 0$,

$$F(\nu, x, t) = F(\nu, 0, t) \exp\left(-\alpha(\nu) \left(1 + \frac{v_F}{c}\right) \int_0^x N(x', t) dx'\right) \quad 3.16$$

and

$$\left(1 - \frac{v_F}{c}\right) \frac{\partial F(\nu, x, t)}{\partial x} = -\alpha(\nu) N(x, t) F(\nu, x, t) \quad . \quad 3.17$$

Integrating over the frequency and using the identity

$(1 - v_F/c)^{-1} = (1 + F_0/cN_0)$ from eq'n (3.2) we obtain

$$\frac{\partial}{\partial X} \left(\int_{\nu_1}^{\nu_2} F(\nu, X, t) d\nu \right) = - \left(1 + \frac{F_0}{cN_0} \right) N(X, t) \int_{\nu_1}^{\nu_2} \alpha(\nu) F(\nu, X, t) d\nu. \quad 3.18$$

The following procedure proves convenient in obtaining a solution of these equations. The procedure consists of transforming the x co-ordinate in which $N(x)$ varies to a z co-ordinate in which $N(z)$ is a constant (we set $N(z) = N_0$). The problem then corresponds to black body radiation into a non-depleting cloud of absorbers in which the intensity at each frequency ν decays exponentially with a decay length which depends on ν .

In this terminology eq'n (3.16) may be rewritten as

$$F(\nu, z(X, t)) = F(\nu, 0) e^{-\frac{\alpha(\nu)}{\alpha_m} z} \quad 3.19$$

where

$$z(X, t) = \alpha_m N_0 \left(1 + \frac{F_0}{cN_0} \right) \int_0^X \frac{N(x', t)}{N_0} dx' \quad 3.20$$

and where α_m is the maximum absorption cross section in the range ν_1 to ν_2 . Also, we have written $F(\nu, 0, t) \rightarrow F(\nu, 0)$ since the incident radiation is constant in time. We now integrate eq'n (3.20) over the frequency range and normalize to obtain

$$\frac{F(z)}{F_0} = \frac{\int_{\nu_1}^{\nu_2} F(\nu, z) d\nu}{\int_{\nu_1}^{\nu_2} F(\nu, 0) d\nu} = \frac{\int_{\nu_1}^{\nu_2} F(\nu, 0) e^{-\frac{\alpha(\nu)}{\alpha_m} z} d\nu}{\int_{\nu_1}^{\nu_2} F(\nu, 0) d\nu} \quad 3.21$$

This equation must be solved (numerically, if necessary) to determine $F(z)$ as a function of z for any functions $F(\nu, 0)$ and $\alpha(\nu)$.

We now invert eq'n (3.20) to solve for X

$$X = \left(\alpha_m N_0 \left(1 + \frac{F_0}{cN_0} \right) \right)^{-1} \int_0^z \frac{dz'}{\left(\frac{N(x, z)}{N_0} \right)} \quad 3.22$$

Now from eq'n (3.15) we may write

$$\frac{N(x)}{N_0} = 1 - \frac{\int_{z_1}^x F(z, x) dz}{F_0} = 1 - \frac{F(z)}{F_0} \quad 3.23$$

where we have used the fact that the number of photons passing a point in the x co-ordinate system is the same as that passing the same point in the z co-ordinate system. Eq'n (3.22) has been derived in a frame of reference where $z = 0$ when $x = 0$. For numerical solutions, it is more convenient to shift to the frame of reference of the radiation front with boundary condition $z = 0$ when $x = -\infty$ and $x = 0$ where $F(z)/F_0 = 0.5$. Substituting eq'n (3.23) in eq'n (3.22) we obtain for positive x

$$X_+ = \left(\alpha_m N_0 \left(1 + \frac{F_0}{c N_0} \right) \right)^{-1} \int_{z_{0.5}}^{z \rightarrow \infty} \frac{dz'}{1 - \frac{F(z')}{F_0}} \quad 3.24$$

and for negative x

$$X_- = - \left(\alpha_m N_0 \left(1 + \frac{F_0}{c N_0} \right) \right)^{-1} \int_{z_{0.5}}^{z \rightarrow 0} \frac{dz'}{1 - \frac{F(z')}{F_0}} \quad 3.24'$$

where we have broken the integration up into two parts for convenience in carrying out numerical calculations. $z_{0.5}$ indicates the value of z where $F(z)/F_0 = 0.5$. Care must be taken that the limit of integration in eq'n (3.24') approaches but never reaches $z \rightarrow 0$.

We now have $F(z)/F_0$ as a function of z from eq'n (3.21) and x as a function of z from eq'ns (3.24). We may thus plot $F(x)/F_0$ as a function of x to obtain the overall structure of the radiation front. The individual frequencies $F(z, x)/F_0$ may also be plotted since we know that they decay exponentially in the z co-ordinate system.

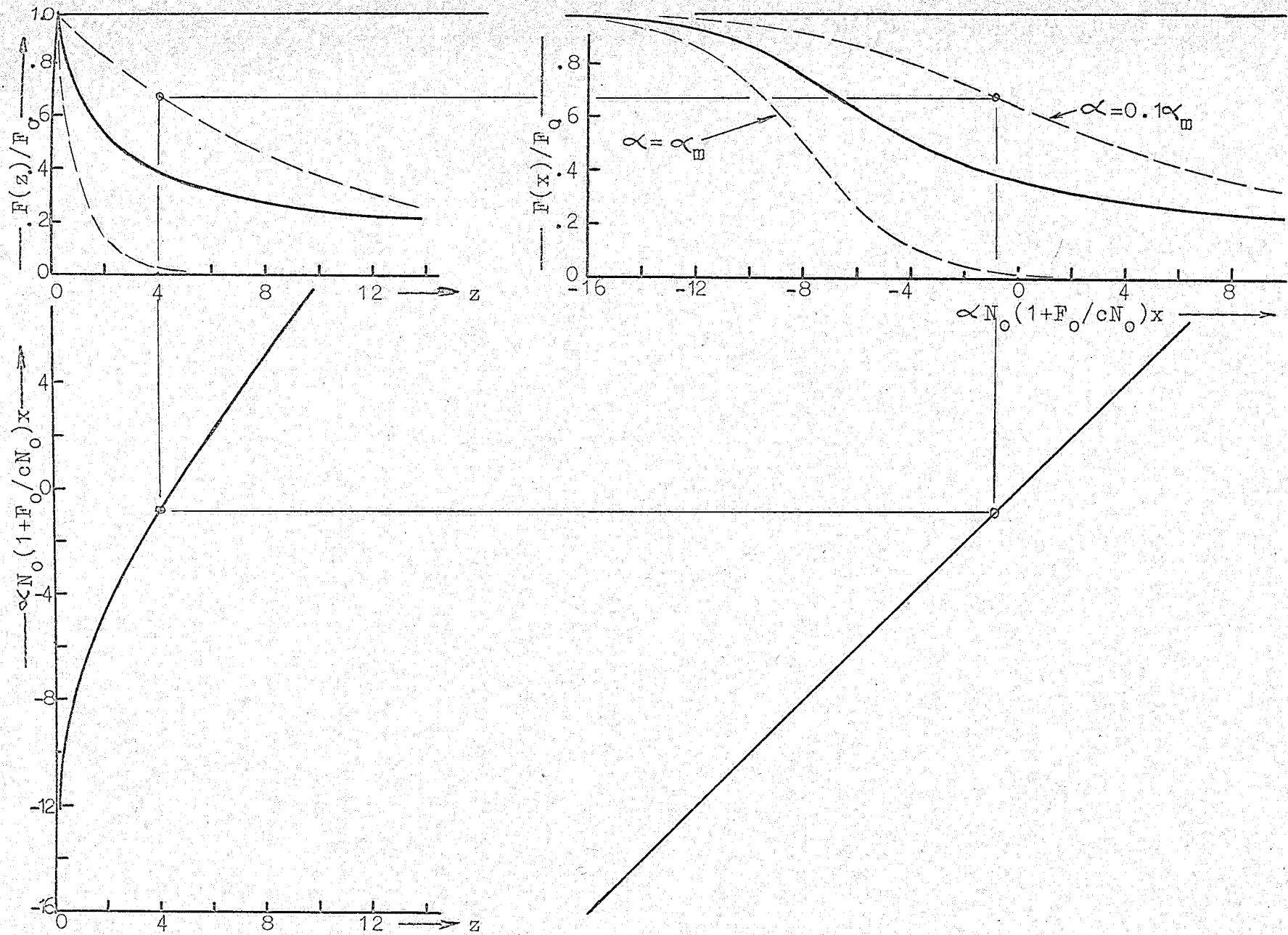


Fig.3.3 Idealized radiation front in oxygen for black body radiation, $F(z)$

An example is plotted in Fig. 3.3 to demonstrate the technique. It shows a dissociation front in oxygen produced by black body radiation from a source at a temperature of 6×10^4 °K. The photo dissociation cross sections in the Schumann - Runge region from 1280 Å to 1800 Å were taken from Metzger and Cook (1964), see Fig.B.3, Appendix B. The program to carry out the numerical calculation of $F(z)/F_0$ and the integration of $(1-F(z)/F_0)^{-1}$ to obtain $z(x)$ appears in Appendix A.

We note in Fig. 3.3 that photons with low absorption cross sections penetrate substantially further than photons with high values of absorption cross section.

In concluding this section on idealized radiation fronts, we should like to point out that although we have assumed that there is no particle motion, if Lagrangian co-ordinates are adopted, the results obtained here are valid regardless of the flow of the gas. Of course, it is still necessary to transform back to Eulerian co-ordinates. Secondly, the radiation front equations (3.10 and (3.11) which are derived for planar symmetry can easily be adapted to consider spherical symmetry such as expanding H II regions in interstellar space.

3.2 Relaxation of restrictions on particle motion and recombination

The assumptions in the last section that all particles are stationary and that recombination and collisional ionization or dissociation are negligible permitted us to obtain the radiation equations (3.10) and (3.11). We now wish to relax these assumptions and, in particular, redefine the front velocity v_F and the coefficient ξ .

3.2.1 The coefficient, ξ . -- In the last section, we used the relation $(1 - \frac{v_F}{c})F_0 = v_F N_0$ to equate the number of photons entering the front from the left to the number of absorbers entering the front from the right. There, we insisted that one photon dissociate or ionize only one absorber. However, if we allow collisions to occur such that the energetic dissociated or ionized particles either dissociate or ionize other absorbers or recombine to become absorbers again, then on the average, we could have one photon dissociate or ionize either more than one absorber or less than one absorber. We now define the coefficient, ξ , to be the number of photons required to dissociate or ionize one absorber ($0 < \xi < \infty$). Thus instead of eq'n (3.1) we write

$$(1 - v_F/c) F_0 = v_F \xi N_0 \quad 3.25$$

or

$$v_F = \frac{F_0 / \xi N_0}{1 + F_0 / c \xi N_0} \quad 3.25'$$

We emphasize that v_F is the rate at which the front is receding from the source. The photon flux density is defined by eq'n (3.13).

3.2.2 The energy input, $W/\rho_1 v_1$. -- The last term $W/\rho_1 v_1$ in eq'n (2.3) is the net energy input per unit mass inside the front. If we neglect radiation losses, we may write

$$W = (1 - v_F/c) F_0 \langle h\nu \rangle = (1 - v_F/c) \int_{\nu_1}^{\nu_2} h\nu F(\nu) d\nu \quad 3.26$$

where $F_0 \langle h\nu \rangle \equiv \int_{\nu_1}^{\nu_2} h\nu F(\nu) d\nu$ is the energy flux and $(1 - v_F/c)$ is the usual relativistic correction. If the particles ahead of the front are stationary with respect to the source then $v_1 = v_F$. The density may be written as

$$\rho_1 \equiv N_0 m_0 + \sum_j n_j m_j \quad 3.27$$

where the subscript 0 refers to the absorbers (of density N_0) and the index j refers to the dissociated or ionized particles and to any impurity particles which may be present in the absorbing gas but which are not affected by the incoming radiation.

n_j is the particle density of j^{th} particles and m refers to the mass. Thus we may write

$$\frac{W}{\rho_1 v_1} = \frac{(1 - v_F/c) F_0 \langle h\nu \rangle}{(N_0 m_0 + \sum_j n_j m_j) v_F} \quad , \quad 3.28$$

which with the help of eq'n(3.25') becomes

$$\frac{W}{\rho_1 v_1} = \frac{\xi \langle h\nu \rangle}{m_0} \left(1 + \frac{\sum_j n_j m_j}{N_0 m_0} \right)^{-1} \quad , \quad 3.29$$

where we have written $v_1 = v_F$.

We note that if there are no impurities in the absorbing gas and if there are no dissociated or ionized particles ahead of the front then the term $\sum_j n_j m_j$ in eq'n (3.29) is zero and we may write

$$\frac{W}{\rho_1 v_1} = \frac{\xi \langle h\nu \rangle}{m_0} \quad . \quad 3.29'$$

We have used this equation previously in section 2.5 where we showed how the temperature behind the radiation front can be estimated. The coefficient ξ and eq'n (3.29) are especially useful when considering R-critical, or weak R-type radiation fronts.

3.3 Weak R-type front

A weak R-type radiation front moves supersonically relative to the gas ahead and behind it. The hot gas is compressed with a compression ratio between 1 and 2 ($1 \leq \rho_4/\rho_1 < 2$). The asymptotic solution ($v_1 \rightarrow c$) of this type of front corresponds to the idealized front described earlier in section 3.1. When the front velocity is comparable with the speed of light one finds $\rho_4/\rho_1 = 1$, an approximate value for T_4 may be obtained from eq'n (2.18) or (2.18') with $v_1 = v_4$ (assuming $\xi = 1$, for $\langle h\nu \rangle - \chi > kT_{\min}$; otherwise for $\langle h\nu \rangle - \chi < kT_{\min}$, $T_4 = T_{\min}$) and the pressure P_4 may be obtained from eq'n (2.14).

In the non relativistic region (where $v_f = F_0/\xi N_0$) we may make various approximations to simplify eq'n (2.5). For all weak R-type fronts the terms $\frac{1}{2} P_1/\rho_1$ and $\frac{g_1}{g_1-1} P_1/\rho_1$

may be neglected with respect to the term $\frac{1}{2}v_1^2$. This corresponds to the standard notation of gas dynamics $M_1^2 \gg 1$, where M_1 is the Mach number. For front velocities at least 10 times larger than the speed of sound in the gas behind the front (i.e. $F_0/\xi N_0 > 10a_4$) we can make the further approximation $\frac{2W}{\xi v_1^3} \equiv W/K \ll 1$. We may now expand the square root of eq'n (2.5) (taking the negative root to correspond to the weak R-type solution) to obtain

$$\begin{aligned} \frac{\rho_4}{\rho_1} &\approx \frac{1 + \frac{1}{2}(\gamma_4+1)\frac{W}{K} + \frac{1}{8}(\gamma_4+1)(\gamma_4^2-1)\left(\frac{W}{K}\right)^2 - \dots}{1 + \frac{W}{K}} \\ &\approx 1 + \left(\frac{\gamma_4-1}{2}\right)\frac{W}{K} + \left(\frac{\gamma_4+3}{2}\right)\left(\frac{\gamma_4-1}{2}\right)\left(\frac{W}{K}\right)^2 + \dots \end{aligned} \quad 3.30$$

where $K \equiv \frac{1}{2}\rho_1 v_1^3$.

Substituting for $W/\rho_1 v_1$ from eq'n (3.29') we obtain

$$\frac{\rho_4}{\rho_1} \approx 1 + \left[\frac{(\gamma_4-1)\xi \langle hV \rangle}{M v_F^2} \right] + \left(\frac{\gamma_4+3}{2} \right) \left[\frac{(\gamma_4-1)\xi \langle hV \rangle}{M v_F^2} \right]^2 + \dots \quad 3.30'$$

where we have let $\rho_1 = N_0 M$ and $v_1 = v_F$ as defined in eq'n (3.25').

For the non relativistic case ($v_F = F_0/\xi N_0$) we obtain to first order

$$\frac{\rho_4}{\rho_1} \approx 1 + (\gamma_4-1) \frac{\langle hV \rangle}{M} \frac{\xi^3 N_0^2}{F_0^2} + \dots \quad 3.30''$$

which illustrates the relationship between the compression ratio and F_0 , N_0 and ξ .

The particle velocity behind the front ($v_p = v_1 - v_4$) is related to the density through the relation $v_p \approx v_F (\rho_4/\rho_1 - 1)$.

Thus from eq'n (3.30') we obtain

$$N_p \approx \frac{(g_4-1) \xi \langle h\nu \rangle}{M v_F} + \left(\frac{g_4+3}{2} \right) \left[\frac{(g_4-1) \xi \langle h\nu \rangle}{M v_F} \right]^2 \frac{1}{v_F} + \dots \quad 3.31$$

and for the non relativistic case to first order we obtain

$$N_p \approx (g_4-1) \frac{\langle h\nu \rangle}{M} \frac{\xi^2 N_0}{F_0} \quad 3.31'$$

Note that the particle velocity behind the front is inversely proportional to the velocity of the radiation front, v_F . The coefficient ξ and the function g_4 depend upon the assumed temperature of the gas behind the front.

Finally, the pressure ratio for the non relativistic case may be written from eq'ns (2.2) and (3.31') as

$$\frac{P_4}{P_1} = 1 + \frac{(g_4-1) \xi \langle h\nu \rangle}{k T_1} \quad 3.32$$

where we have used the eq'n of state $p_1 = N_0 k T_1$ and $\rho_1 = n_0 M$. This ratio should check with the value obtained from the equations of state.

Obtaining numerical solutions from the above equations is straight forward. With the assumed temperature T_4 (e.g. we choose $T_4 = T_{\max}$) we approximate the enthalpy by $h_4 \approx (5kT_4 + \chi)/M$ and the internal energy by $\mathcal{E}_4 \approx (3kT_4 + \chi)/M$ where χ is the ionization or dissociation energy. The effective adiabatic exponent is then $g_4 = h_4/\mathcal{E}_4$. With this value of g_4 and $\xi = 1$ (if $T_4 = T_{\max}$) approximate values of ρ_4 and P_4 are obtained from eq'ns (3.30'') and (3.32). It is then possible to obtain g_4 accurately either by calculation or from curves of $g(p, T)$ vs T . Accurate values of all quantities may then be obtained either from the asymptotic

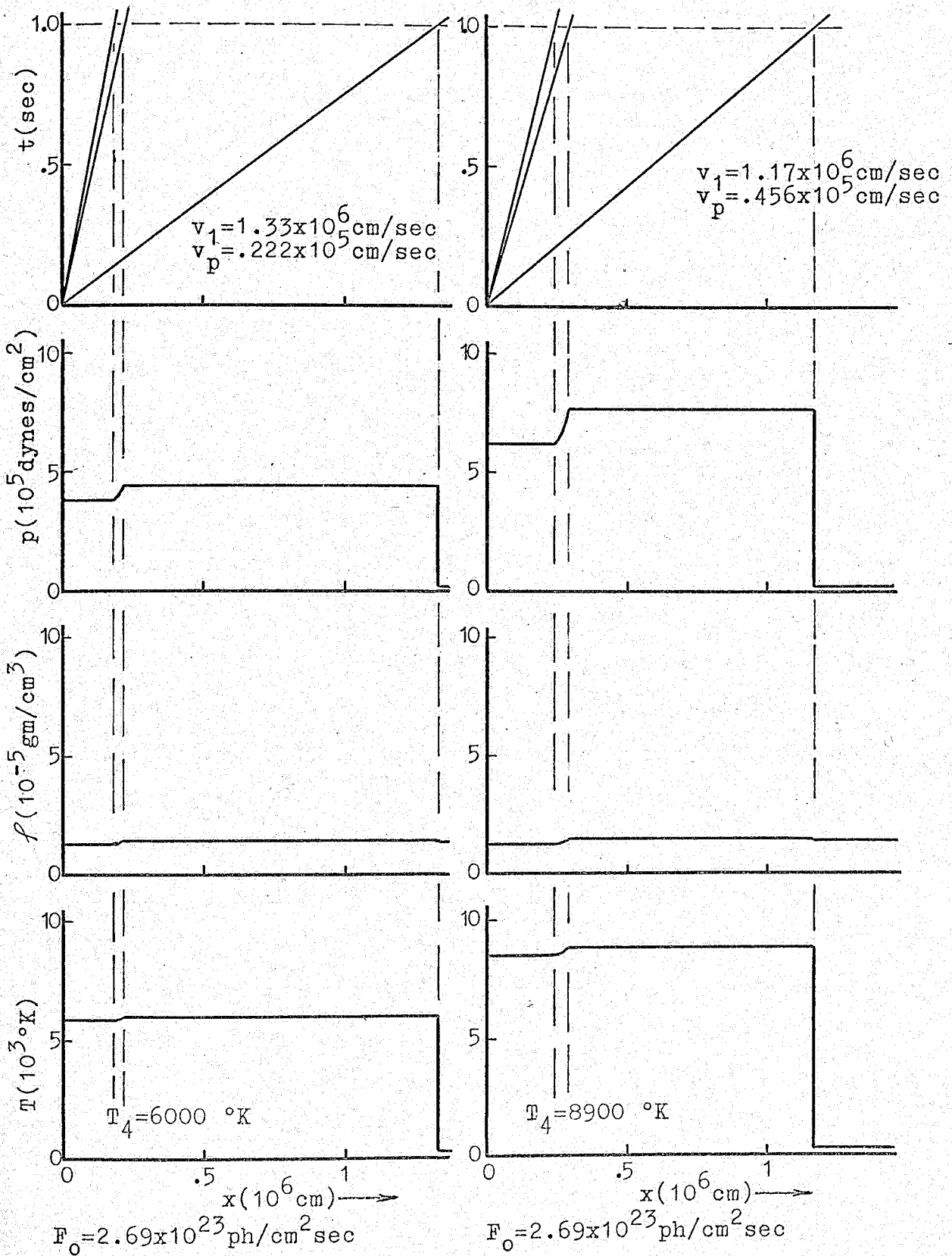


Fig.3.4 Weak R-type radiation front

formulae above or directly from eq'n (2.5) and the conservation eq'ns (2.1) to (2.3).

An example of a weak R-type radiation front is shown in Fig. 3.4. For this and other examples (Figs 3.4 to 3.8 inclusive) we use oxygen at a pressure of 0.01 atm ($N_0 = 2.69 \times 10^{17}$ particles/cm³) and a temperature of $T_1 = 300$ °K. We work out the examples for two final temperatures $T_{\min} = 6000$ °K and $T_{\max} = 8900$ °K. For T_{\min} we use $h_4 = 2.31 \times 10^{11}$ ergs/gm, $g_4 = 1.146$ and $a_4 = 1.835 \times 10^5$ cm/sec. For T_{\max} , $h_4 = 2.78 \times 10^{11}$ ergs/gm, $g_4 = 1.228$ and $a_4 = 2.517 \times 10^5$ cm/sec. The dissociating photons have an average energy of $8.8 eV$ and a value of $5.08 eV$ is used as the dissociation energy of oxygen. The upper diagram in these examples is a plot of time, t versus position x showing the velocity of propagation of the various steady discontinuities in the flow. The lower three diagrams are plots of the pressure, density and temperature as a function of x at a constant time, $t = 1$ sec.

In Fig. 3.4 we assume a value of $F_0/N_0 = 10^6$ cm/sec. At T_{\max} we find $v_1 = 1.17 \times 10^6$ cm/sec ($\xi \equiv F_0/v_1 N_0 = 0.855$) and at T_{\min} , $v_1 = 1.33 \times 10^6$ cm/sec ($\xi = 0.752$). Notice that although the pressure and temperature rise sharply behind the front, the density is almost constant.

3.4 R-critical front

If the velocity of a supersonic radiation front is reduced, either by reducing F_0 or by increasing N_0 , one will

reach the point where the velocity relative to the hot gas behind the front is exactly sonic, but the velocity relative to the undisturbed gas ahead of the front is still supersonic. This is an R-critical front. It corresponds to the Chapman - Jouguet point and can be considered the high density limit of weak R-type radiation fronts. The compression ratio is always slightly below 2. The structure of the front is quite complicated - a shock starts to develop in the radiation front and the head of the rarefaction wave which follows is merged with the front.

Approximate analytical relations are readily obtained for this case. The condition $v_4 = (g_4 \rho_4 / \rho_1)^{1/2} \equiv a_4$ (a_4 is the speed of sound in the gas behind the front) results in the quantity under the square root in eq'n (2.5) being identically zero. Thus after some algebra we obtain the compression ratio

$$\frac{v_i}{a_4} = \frac{\rho_1}{\rho_4} = \frac{g_4 + 1}{g_4} \left(\frac{1}{1 + \frac{\rho_1}{\rho_4 v_i^2}} \right), \quad 3.33$$

where we note that $\rho_1 / \rho_4 v_1^2 \ll 1$ for an R-critical front ($M_1^2 \gg 1$).

The particle velocity behind the front is given

by

$$\frac{v_P}{a_4} = \frac{v_i}{a_4} - 1 = \frac{1}{g_4} \frac{1 - g_4 \frac{\rho_1}{\rho_4 v_i^2}}{1 + \frac{\rho_1}{\rho_4 v_i^2}},$$

which to first order in $\rho_1 / \rho_4 v_1^2$ may be written as

$$\frac{v_P}{a_4} = \frac{1}{g_4} \left(1 - (g_4 + 1) \frac{\rho_1}{\rho_4 v_i^2} \right). \quad 3.34$$

The pressure behind the front as given by eq'n (2.2) is

$$P_4 = P_1 + \rho_1 v_1 v_P \approx P_1 + \rho_1 a_4^2 \left(\frac{g_4 + 1}{2g_4^2} \right) \left(1 - (g_4 + 2) \frac{\rho_1}{\rho_1 v_1^2} \right), \quad 3.35$$

where we have substituted from eq'ns (3.33) and (3.34) and retained only first order terms in $p_1 / \rho_1 v_1^2$.

The condition that the square root in eq'n (2.5) is zero gives us an extra relation between v_1 , ρ_1 and W .

Neglecting terms of p_1 / ρ_1 , we obtain

$$v_1 \approx \left(2(g_4^2 - 1) \frac{W}{\rho_1} \right)^{1/3} \quad 3.36$$

or, solving for ρ_1 and substituting for v_1 from eq'n (3.33),

$$\rho_{RC} = \rho_1 \approx \frac{2g_4^3 (g_4 - 1) W}{(g_4 + 1)^2 a_4^3} \quad 3.37$$

Finally, we obtain a relation for the coefficient ξ from eq'ns (2.3) and (3.29')

$$\frac{W}{\rho_1 v_1} = \frac{\xi \langle h v \rangle}{M} = h_4 - \frac{1}{2} (v_1^2 - v_4^2) - h_1,$$

from which with the help of eq'ns (2.12) and (3.33) we obtain

$$\xi \approx \frac{M}{\langle h v \rangle} \left\{ h_4 \left(\frac{g_4 + 1}{2g_4^2} \right) \left(1 + (g_4^2 - 1) \frac{2\rho_1}{\rho_1 v_1^2} \right) - h_1 \right\} \quad 3.38$$

The R-critical case is a point solution separating the M-critical fronts and weak R-type fronts. For a given set of conditions eq'n (3.37) is useful in predicting the type of front which one can expect to occur. For this purpose, one must approximate the value of a_4 by the relation

$$a_4 \equiv (g_4 \rho_4 / \rho_2)^{1/2} = (g_4 - 1) h_4)^{1/2} = (g_4 h T_4 / m)^{1/2}, \quad 3.39$$

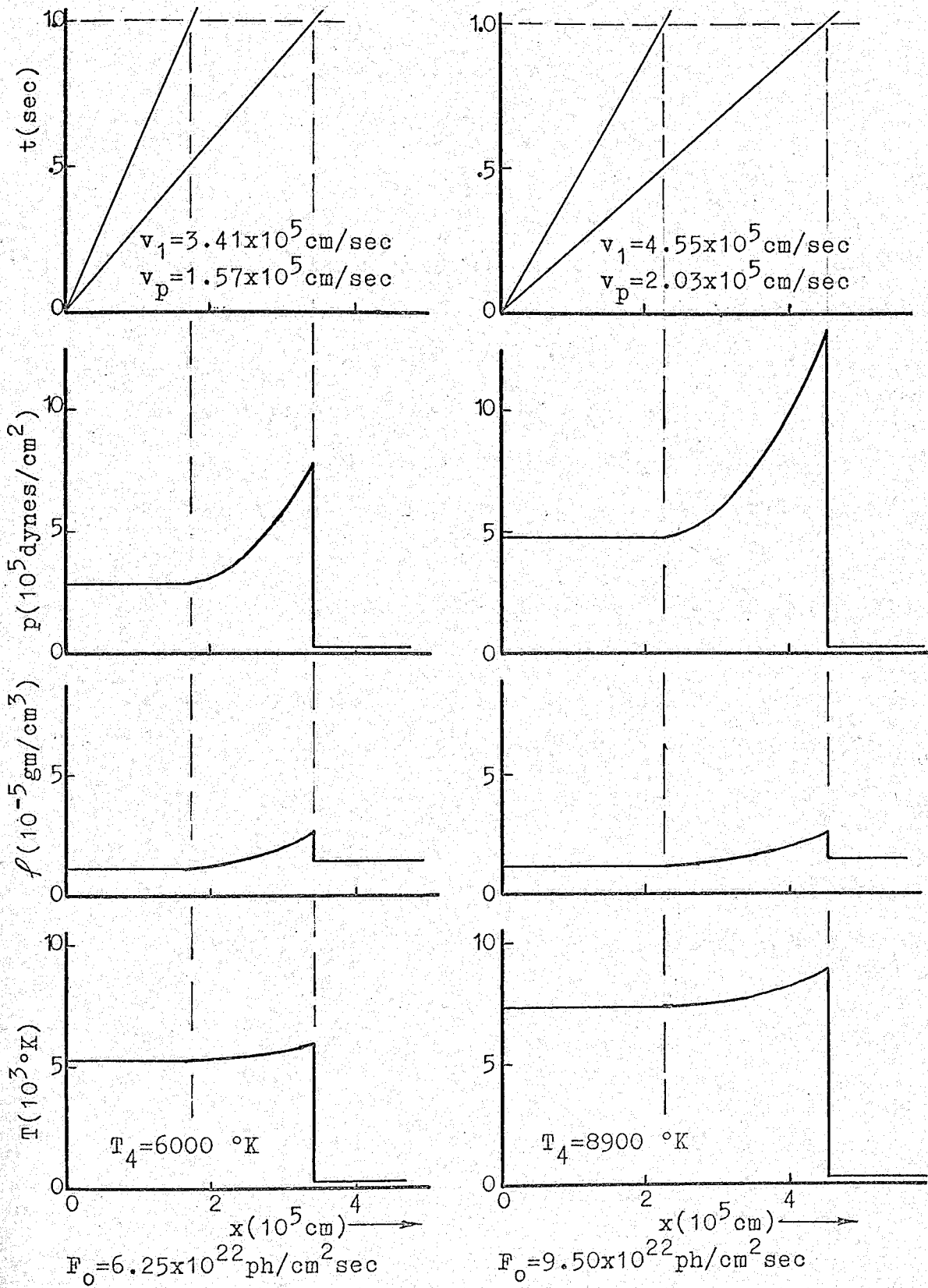


Fig. 3.5 R-critical radiation front

where we emphasize that m is the average value of the mass of the particles behind the front, $m \equiv \sum_j n_j m_j / \sum_j n_j$. A value of g_4 is obtained as outlined previously for the weak R-type case.

A complete numerical solution for the R-critical case is straightforward once an accurate value of g_4 is obtained. We treat the rarefaction wave following the front as an isentropic expansion in a manner outlined in section 2.3. For a first approximation we assume $g_5 = g_4$. (Quantities behind the tail of the rarefaction carry the subscript 5). Once the temperature T_5 , pressure p_5 , density ρ_5 and enthalpy h_5 are approximately known, a more accurate value of g_5 may be obtained and the final properties of the gas calculated more accurately.

An example of an R-critical radiation front calculated for the same conditions as used in the weak R-type case (see Fig (3.4)) is shown in Fig. (3.5). We find that for T_{\max} , we require $F_0 = 9.50 \times 10^{22}$ photons/cm² sec and the front travels at a velocity $v_1 = 4.55 \times 10^5$ cm/sec ($\xi = 0.777$). For T_{\min} , $F_0 = 6.25 \times 10^{22}$ photons/cm²sec and $v_1 = 3.41 \times 10^5$ cm/sec ($\xi = 0.680$). Notice that the pressure ratio is large whereas the compression ratio is still quite small. The rarefaction wave is dominant.

3.5 Weak D-type front preceded by a shock wave

Weak D-type fronts lie on the opposite extreme on the density scale from weak R-type fronts, they occur for

high densities and relatively low radiation intensities. This subsonic radiation front has many similarities with combustion zones. It moves subsonically with respect to the gas ahead and behind it. As explained previously, a shock discontinuity propagates ahead of the front compressing the gas, the slower moving radiation front heats and expands this compressed gas. A rarefaction wave would travel at sonic speed and overtake the radiation front and, therefore, does not exist. We now have two discontinuities to consider-- the shock wave with no energy input and the weak D-type front with energy input.

3.5.1 General equations. -- The conservation equations across the shock corresponding to eq'n (2.5) with $W = 0$ give

$$\frac{\rho_2}{\rho_1} = \frac{1}{\beta^{2-1}} \left(\frac{v_1^2 + \frac{p_1}{2\rho_1}}{\frac{v_1^2}{2} + \frac{\beta_1 p_1}{\rho_1}} \right) \left\{ \beta_2 + \sqrt{\beta_2^2 - (\beta_2^2 - 1) \frac{\left(\frac{v_1^2}{2} + \frac{\beta_1 p_1}{\rho_1} \right)^2}{\left(\frac{v_1^2}{2} + \frac{p_1}{2\rho_1} \right)^2}} \right\} \quad 3.40$$

where we have chosen the positive root. We note in passing that for strong shocks such that $v_1^2 \gg p_1/\rho_1$ (or $M_1^2 \gg 1$) we obtain the well known approximate relation

$$\frac{\rho_2}{\rho_1} \approx \frac{\beta_2 + 1}{\beta_2 - 1} \quad 3.40'$$

If we assume a velocity for the shock front v_1 we may solve for all the parameters behind the front as outlined in Gaydon and Hurle (1963), Chapter 3 or Ahlborn and Salvat (1967). (Preferably we use plots of $\frac{\rho_2}{\rho_1}$, $\frac{p_2}{p_1}$ and $\frac{T_2}{T_1}$ versus Mach number as given in Gaydon and Hurle, page 52). At any rate the solution is straightforward and we shall

not comment on this point any further.

The conservation equations across the weak D-type front corresponding to eq'n (2.5) give

$$\frac{P_4}{P_2} = \frac{g_4}{g_4-1} \left(\frac{\frac{v_3^2}{2} + \frac{P_2}{2g_2}}{\frac{v_3^2}{2} + \frac{g_2 P_2}{g_2-1} + \frac{W}{g_2 v_3}} \right) \left\{ 1 + \sqrt{1 - \frac{(g_4^2-1) \left(\frac{v_3^2}{2} \right) \left(\frac{v_3^2}{2} + \frac{g_2 P_2}{g_2-1} + \frac{W}{g_2 v_3} \right)}{g_4^2 \left(\frac{v_3^2}{2} + \frac{P_2}{2g_2} \right)^2}} \right\} \quad 3.41$$

where we have again chosen the positive square root. (The negative root corresponds to a strong D-type front -- an expansion shock with energy input, which does not occur in our case.)

Since the particles are stationary ahead of the shock front and behind the radiation front we have the following relationship for the particle velocity between the shock and radiation fronts:

$$\begin{aligned} v_F &= v_1 - v_2, & v_S &= v_1 \\ v_F &= v_4 - v_3, & v_F &= v_4 \end{aligned} \quad 3.42$$

where the velocities are defined as in Fig. 2.2, the subscripts S and F refer to shock and front respectively.

The final pressure, obtained from a momentum equation corresponding to eq'n (2.2), is

$$P_4 = P_2 - f_2 v_3 v_F \quad 3.43$$

where the particle velocity v_F is defined in eq'n (3.42).

For future reference we note that the final pressure P_4 must fall in the limits $\frac{1}{2} P_2 < P_4 < P_2$.

The equations in this weak D-type case do not lend themselves to approximate solutions as easily as in the weak R-type and R-critical cases. We, therefore, follow a numerical method of attack. As usual, we assume the

final temperature T_4 . We then assume a reasonable shock velocity v_1 , calculate the thermodynamic quantities behind the shock front, calculate the velocity of and thermodynamic properties behind the radiation front and finally, calculate the radiation intensity required to produce the velocity. An iterative procedure is required to obtain exact solutions.

For potential users of this technique, we will outline the iteration procedure in more detail in the next section. Readers who are not particularly interested in details may omit this subsection and proceed to Fig. 3.6 at the end of the section.

3.5.2 Iterative procedure for calculations.-- The procedure is as follows: We choose a shock velocity, v_1 , and calculate p_2 , f_2 , T_2 , h_2 , g_2 , and the velocities v_2 and v_p . (For oxygen we use curves of p_2/p_1 , f_2/f_1 , T_2/T_1 versus Mach number given by Gaydon and Hurle, page 52). We will see below that the final pressure p_4 must fall between $\frac{1}{2}p_2 < p_4 < p_2$ and can thus calculate a value of h_4 within 5% (using assumed T_4) and g_4 quite accurately.

The term beneath the square root sign in eq'n (3.41) must have a numerical value between 0 and 1. By assuming that it is zero we obtain a maximum value of v_3 ,

$$\frac{v_3^2}{2} = \frac{g_4^2}{g_4^2 - 1} \frac{\left(\frac{v_3^2}{2} + \frac{p_2}{2f_2}\right)^2}{\left(\frac{v_4^2}{2} + h_4\right)}, \quad 3.44$$

where we have used the energy equation

$$\frac{v_4^2}{2} + h_4 = \frac{v_3^2}{2} + h_2 + \frac{W}{P_2 v_3} \quad ,$$

and eq'n (2.12) for the enthalpy. Since $v_4 = v_p + v_3$ we may solve eq'n (3.44) by iterating to obtain an upper limit for v_3 .

With the square root equal to zero the rest of eq'n (3.41) gives a minimum value for f_4

$$\frac{f_4 \min}{f_2} = \frac{g_4}{g_4 - 1} \left(\frac{\frac{v_3^2}{2} + \frac{P_2}{2 P_2}}{\frac{v_4^2}{2} + h_4} \right) \quad , \quad 3.45$$

which we solve using the value of v_3 obtained from eq'n (3.44). We then obtain a minimum value for v_3

$$v_3 \min = \frac{v_p}{(f_2 / f_4 \min - 1)} \quad . \quad 3.46$$

The numerical values of $v_{3\max}$ and $v_{3\min}$ usually agree within a factor two. We substitute the mean of these two values into eq'n (3.41) to obtain a first approximation for f_4 and then utilize eq'n (3.46) to obtain a better value of v_3 . We repeat this iterative procedure until we obtain a self-consistent value of v_3 and f_4 . (The solutions of v_3 tend to oscillate about the final value and it is thus best to average the initial value of v_3 with the result of the iteration as a starting point for the next iteration. Two or three iterations are usually sufficient to obtain an accurate value of v_3 .) We then calculate v_4 and P_4 from eq'ns (3.42) and (3.43).

With a relatively accurate value of p_4 we can obtain accurate values of h_4 and g_4 . Similarly, one can calculate accurate values of v_3 , v_4 , f_4 and p_4 .

Finally we use eq'n (2.4) and the energy equation corresponding to eq'n (2.3) to obtain the radiation intensity required to produce the observed front:

$$F_0 = \frac{f_2 v_3}{\langle h\nu \rangle} \left(h_4 - h_2 + \frac{v_4^2}{2} - \frac{v_3^2}{2} \right), \quad 3.47$$

where we assume $v_3/c \ll 1$.

If one wants to calculate v_1 and other quantities for an experimentally given f_1 and F_0 , one must vary the assumed v_1 (eventually by interpolation) until the value of F_0 calculated from eq'n (3.47) agrees with the experimentally given flux density.

An example of a weak D-type radiation front (for our standard conditions as in Fig. 3.4) preceded by a Mach 3 shock front is shown in Fig. 3.6. For T_{\max} , the photon flux, $F_0 = 4.72 \times 10^{21}$ photons/cm²sec, enters the shocked gas with a velocity $v_3 = 0.417 \times 10^4$ cm/sec ($\xi \equiv F_0 f_1 / v_3 f_2 N_0 = 0.719$). For T_{\min} , $F_0 = 4.62 \times 10^{21}$ photons/cm²sec and $v_3 = 0.491 \times 10^4$ cm/sec ($\xi = 0.549$). We notice that in this case the pressure ratio is not as large as in the other cases. However, if we study the density distribution for this weak D-type (subsonic) front, it is seen that these radiation fronts act like "leaky" pistons, pushing the shocked gas away from the radiation

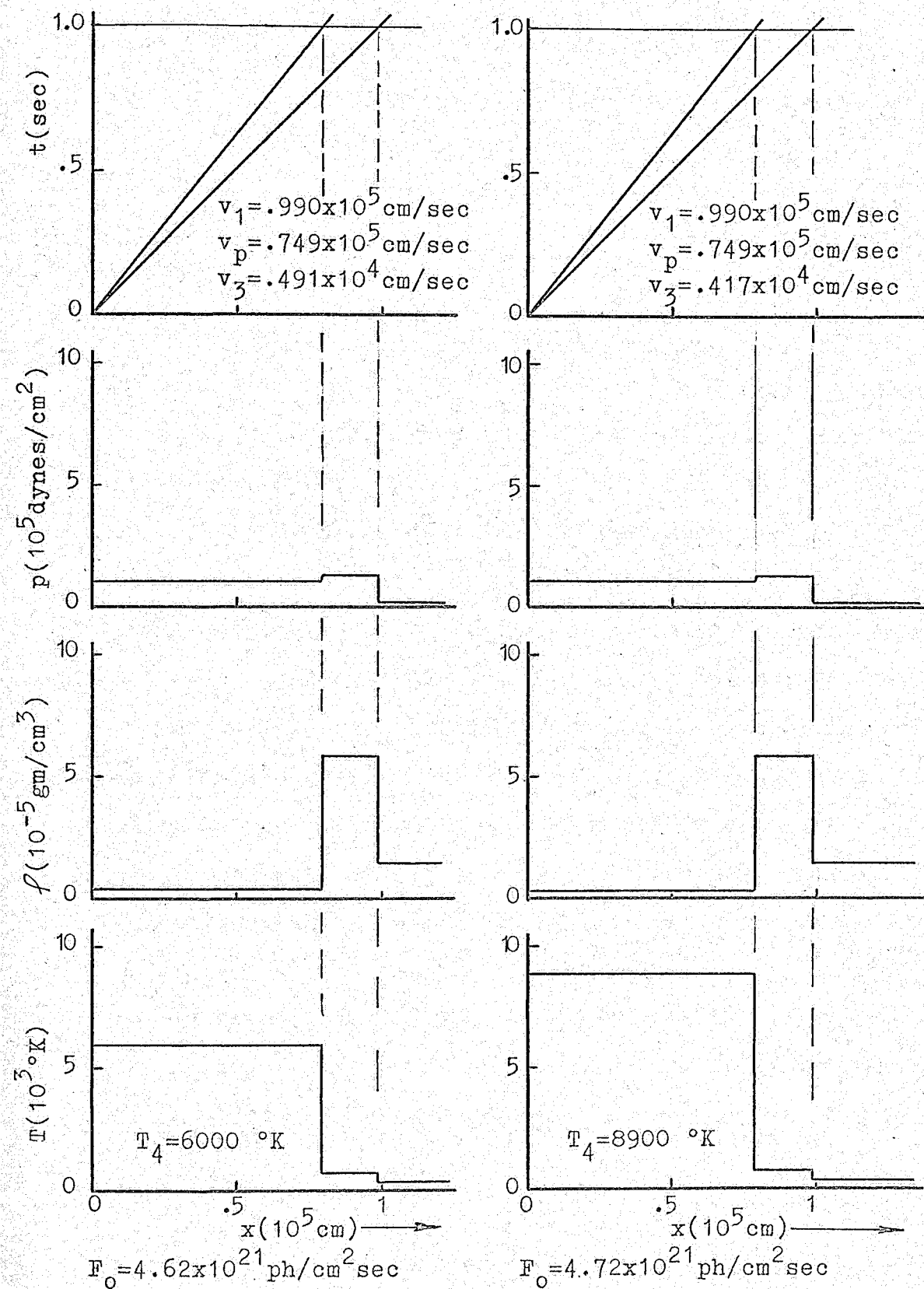


Fig.3.6 Weak D-type radiation front preceded by a shock

source into the undisturbed gas. Behind the radiation front the density of the gas (which is completely at rest) is substantially lower than the initial density N_0 . This behavior is markedly different from the weak R-type (supersonic) radiation fronts.

3.6 D-critical front preceded by a shock

We will now discuss the low density limit of subsonic (weak D-type) radiation fronts. This limiting solution is called the D-critical front. The appearance of a D-critical radiation front is exactly the same as for a weak D-type front; the only difference is that the front travels at sonic speed with respect to the gas behind it. At slightly higher velocities a rarefaction wave begins to form. The D-critical case represents a singular solution which separates weak D-type fronts from M-critical fronts.

As for the weak D-type fronts we must consider two discontinuities. Approximate analytical relations are again more difficult to obtain than in the R-critical case. As before, the condition $v_4 = a_4$ results in the quantity under the square root in eq'n (3.41) being identically zero. Corresponding to eq'n (3.33) the compression ratio is

$$\frac{v_3}{a_4} = \frac{p_4}{p_2} = \frac{2\gamma+1}{\gamma} \frac{1}{\left(1 + \frac{p_2}{p_2 v_3^2}\right)}, \quad 3.48$$

where we note that contrary to the R-critical front the term $p_2/p_2 v_3^2 \gg 1$ (or $M_3^2 \ll 1$) for a D-critical front. Eq'n (3.48) may be rearranged and solved for v_3

$$v_3 = \frac{g_4}{g_2(g_4+1)} \frac{a_2^2}{a_4} \left[1 + \frac{f_2 v_3^2}{P_2} \right] \quad , \quad 3.49$$

where we have used the definition $a_2^2 = g_2 p_2 / f_2$. The term in the square brackets is approximately equal to unity.

The condition that the square root in eq'n (3.41) is zero gives us an extra relation involving the energy flux W . We solve this equation for v_3 to obtain

$$v_3 = \left(\frac{g_1^2}{g_4^2 - 1} \right) \frac{P_2}{2g_2} \frac{a_2^2}{W} \left[1 + \frac{f_2 v_3^2}{P_2} \right] \left[1 + \frac{g_2 P_2 v_3}{(g_2 - 1) W} + \frac{f_2 v_3^3}{2W} \right]^{-1} \quad , \quad 3.50$$

where again a_2 is the speed of sound ahead of the front and the terms in the square brackets may be considered to be correction factors which are set equal to unity in a first approximation. We now equate eq'ns (3.49) and (3.50) and solve for the pressure p_2 to obtain

$$P_2(DC) = \frac{2(g_4 - 1)}{g_4 a_4} W \left[1 + \frac{g_2 P_2 v_3}{(g_2 - 1) W} + \frac{f_2 v_3^2}{2W} \right] \left[1 + \frac{f_2 v_3^2}{P_2} \right]^{-1} \quad . \quad 3.51$$

We note that except for the small correction factors the pressure ahead of the front depends only on the energy flux W .

The relationships for the particle velocity between the shock and the radiation front and for the pressure drop across the radiation front are the same as for the weak D-type case (see eq'ns (3.42) and (3.43)). From these equations and eq'n (3.48) we may obtain the pressure ratio

$$\frac{P_4}{P_2} = \frac{1}{g_4 + 1} \left[1 + \frac{f_2 v_3^2}{P_2} \right] \quad . \quad 3.52$$

If typical numerical values are inserted we find $p_4 \approx \frac{1}{2} p_2$. From this equation and equation (3.51) we obtain the pressure behind the radiation front

$$P_4(DC) = \frac{2(\gamma_4 - 1)}{\gamma_4(\gamma_4 + 1) a_4} W \left[1 + \frac{\gamma_2 P_2 v_3}{(\gamma_2 - 1) W} + \frac{\rho_2 v_3^2}{2 W} \right] \quad 3.53$$

With a lengthy calculation we can obtain the shock front velocity associated with a D-critical front. For this purpose we use the relation $v_p = a_4 - v_3$ to rewrite eq'n (3.49) as

$$v_p = a_4 - \frac{\gamma_4}{\gamma_4(\gamma_4 + 1)} \frac{a_2^2}{a_4} \left[1 + \frac{\rho_2 v_3^2}{P_2} \right] \quad 3.54$$

We must now write v_p and a_2 in terms of the velocity v_1 . For this purpose we assume that the effective adiabatic exponents ahead and behind the shock are identical, $\gamma_2 = \gamma_1$, and use the ordinary shock equations for an ideal gas. The particle velocity behind the shock is

$$v_p = (2/\gamma_2 + 1) \left[(M_1^2 - 1) / M_1^2 \right] v_1,$$

where $M_1 \equiv v_1/a_1$ is the Mach number of the shock. For strong shocks the term in brackets approaches unity. We may write

$$a_2^2 = a_1^2 (T_2/T_1),$$

where

$$\frac{T_2}{T_1} = \frac{(\gamma_2 M_1^2 - \frac{\gamma_2 - 1}{\gamma_2}) (\frac{\gamma_2 - 1}{2} M_1^2 + 1)}{(\frac{\gamma_2 + 1}{2})^2 M_1^2} \approx \gamma_2 \left(\frac{2}{\gamma_2 + 1} \right)^2 \left(\frac{\gamma_2 - 1}{2} M_1^2 + 1 \right)$$

Substituting these equations into eq'n (3.54) we obtain a quadratic equation, the solution of which is

$$v_p(DC) \approx \frac{-a_4 (\frac{\gamma_2 + 1}{\gamma_2 - 1}) (\frac{\gamma_2 + 1}{\gamma_2}) \frac{[K_2]}{[K_1]} \left(1 - \sqrt{1 + \left\{ 1 - \frac{2\gamma_1}{a_1^2} \left(\frac{\gamma_4}{\gamma_4 + 1} \right) \left(\frac{2}{\gamma_2 + 1} \right)^2 [K_1] \right\} \left\{ \frac{2\gamma_1}{\gamma_4 + 1} (\gamma_2 - 1) \frac{[K_1]}{[K_2]^2} \right\}} \right)}{3.55}$$

with the correction terms

$$[K_1] = \left[1 + \rho_2 v_2^2 / P_2 \right] \quad 3.56$$

$$[K_2] = \left[\frac{M_1^2 - 1}{M_1^2} \right] \quad 3.57$$

In calculating numerical values of $v_1(DC)$, one first obtains an approximate value by neglecting the correction terms and then an accurate value by repeating the calculation with the correction terms included.

The critical density may be calculated by using the pressure ratio

$$\frac{P_2}{P_1} = \frac{2g_2 M_1^2 - (g_2 - 1)}{g_2 + 1} \approx \frac{2g_2}{g_2 + 1} \frac{v_1^2}{a_1^2}$$

where again we assume, $g_2 = g_1$. From the definition $a_1^2 = g_1 P_1 / \rho_1$ we obtain

$$\rho_1(DC) = \left(\frac{g_2 + 1}{2} \right) \frac{P_2(DC)}{v_1^2(DC)} \quad 3.58$$

where the initial pressure $P_2(DC)$ and velocity $v_1(DC)$ are defined in eq'ns (3.51) and (3.55) respectively. We note that in the first approximation $\rho_1(DC)$ depends linearly upon the photon flux F_0 . Since the D-critical case is a singular solution separating the weak D-type and M-critical cases eq'n (3.58) is useful in predicting which front shall occur for a given set of conditions.

A numerical solution for a specific set of conditions may be obtained from the above equations. However, for exact solutions it is preferable to apply the basic

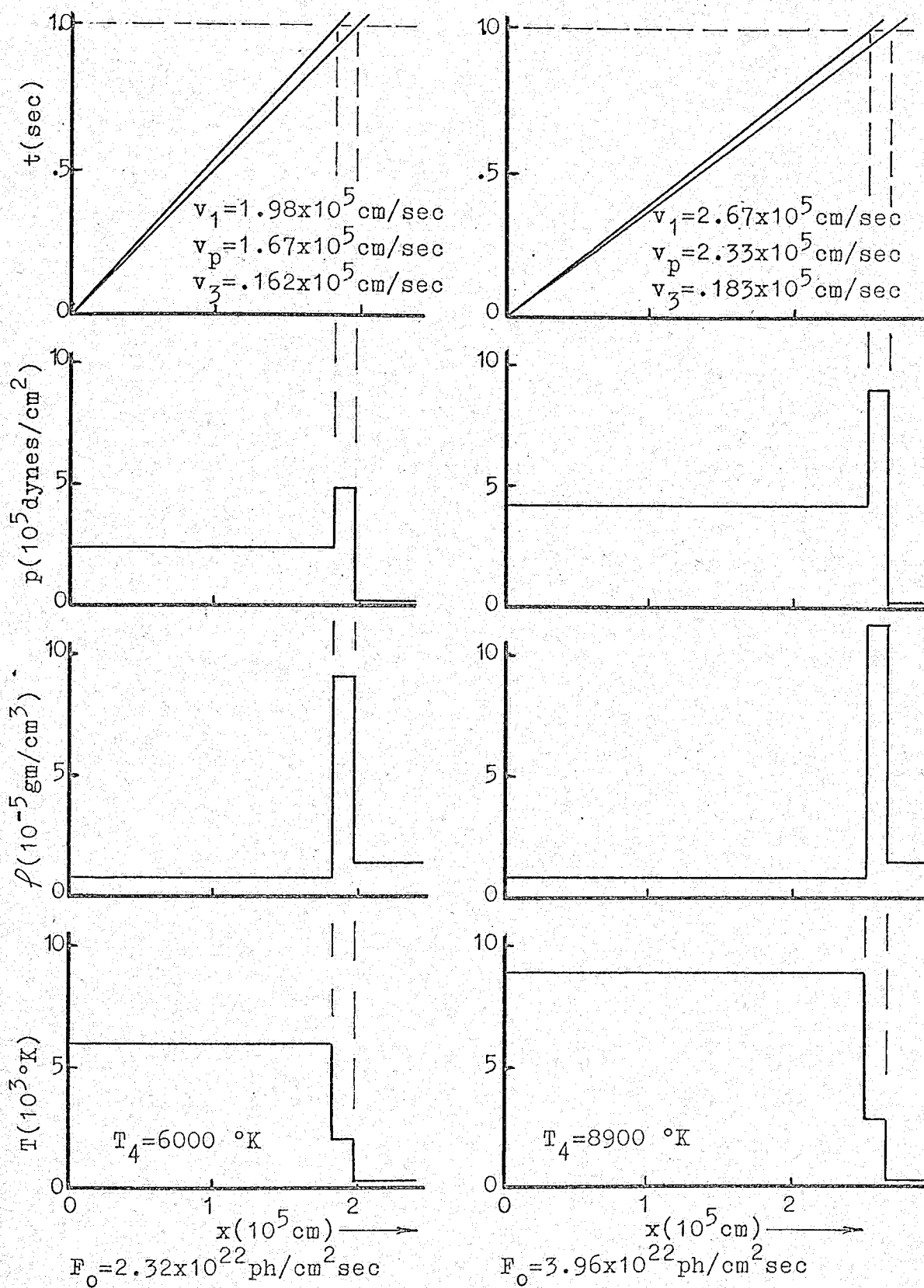


Fig.3.7 D-critical radiation front preceded by a shock

equations across the shock and radiation front such as eq'ns (3.40) and (3.41). The procedure is similar to that used for calculating weak D-type fronts.

Fig. 3.7 shows an example of a D-critical radiation front (for our standard conditions as in Fig. 3.4). In this case for T_{\max} , a Mach 8.10 shock ($v_1 = 2.67 \times 10^5$ cm/sec) precedes the radiation front. The radiation flux, $F_0 = 3.96 \times 10^{22}$ photons/cm²sec enters the shocked gas with a velocity, $v_3 = 0.183 \times 10^5$ cm/sec ($\xi \equiv F_0 \rho_1 / v_3 \rho_2 N_0 = 1.02$). For T_{\min} , a Mach 6.02 shock ($v_1 = 1.98 \times 10^5$ cm/sec) precedes the front. $F_0 = 2.32 \times 10^{22}$ photons/cm²sec and $v_3 = 0.162 \times 10^5$ cm/sec ($\xi = 0.893$). We notice that the appearance of the flow is very similar to the weak D-type case; however, the shocked region is narrower and the pressure and compression ratio are higher. A D-critical front "sweeps up" less gas than a weak D-type radiation front.

3.7 M-critical front preceded by a shock

We have studied radiation fronts at low and high densities and have given limiting densities for these super and subsonic radiation fronts. If one calculates numerical examples with given F_0 , N_0 and T_4 it is found that the high density limit $\rho_1 (RC)$ of the supersonic radiation fronts is still considerably below the low density limit $\rho_1 (AC)$ of the subsonic radiation fronts (see Fig 1.1). The region

between $\rho_1 (RC)$ and $\rho_1 (DC)$ corresponds to the M-type conditions of Kahn. Thus radiation fronts which occur in this region are called M-critical reminding us that these fronts exist over an extended range of densities which lie in the Middle between the Rarified and Dense conditions.

A radiation front which travels slightly faster than a D-critical front, $v_F > a_4$, must have a rarefaction wave following it. On the other extreme when the front velocity is slightly less than the R-critical velocity, a shock must propagate ahead of the radiation front and a rarefaction wave follow it. We thus see that an R-critical front can also be described as a D-critical front slightly preceded by (or merged with) a shock but with both traveling at the same velocity. This can be confirmed by numerical calculations. We assume that in the M-critical region a radiation front propagates at sonic velocity relative to the gas behind it such that $v_4 - a_4 \equiv (g_4 p_4 / \rho_4)^{1/2}$ and such that the term under the square root in eq'n (3.41) is identically zero.

The velocity relationships are now slightly more complicated. Corresponding to eq'n (3.42) we now have

$$v_s = v_i \quad ; \quad v_p = v_i - v_2 \quad , \quad 3.59$$

$$\left. \begin{array}{l} v_F = v_3 + v_p \\ v_F = v_4 + v_{p4} \end{array} \right\} ; \quad v_p - v_{p4} = v_4 - v_3 \quad ,$$

where v_{p4} is the velocity of the particles leaving the radiation front measured in the lab system. From the equation of conservation of mass, $\rho_2 v_3 = \rho_4 v_4$ and from eq'n (3.59) we obtain

$$v_{p4} = v_p - v_3 \left(\frac{\rho_2}{\rho_4} - 1 \right) \quad 3.60$$

Corresponding to eq'n (3.43) the pressure behind the front is

$$p_4 = p_2 - \rho_2 v_3 (v_p - v_{p4}) \quad 3.61$$

We note that for all M-critical fronts $p_4 \approx (1/2)p_2$ to about 5% accuracy.

To obtain a numerical solution we follow roughly the same procedure as outlined in section 3.5.2 for weak D-type fronts. Assuming a reasonable shock velocity v_1 we calculate all the thermodynamic quantities behind the shock. Since $p_4 \approx (1/2)p_2$ we can calculate h_4 and g_4 quite accurately (using an assumed value of T_4). A value of v_3 is obtained by iteration from eq'n (3.44) using a value of a_4 obtained from eq'n (3.39). The compression ratio, ρ_4/ρ_2 , is obtained from eq'n (3.48), and the particle velocity behind the front, v_{p4} , is obtained from eq'n (3.60). Finally an accurate value of p_4 is obtained from eq'n (3.61) and an accurate value of a_4 from the definition, $a_4^2 = g_4 p_4 / \rho_4$. If there is insufficient accuracy the whole procedure is repeated.

The radiation intensity associated with the initially assumed shock velocity is found from eq'n (3.47). The rarefaction wave is treated in exactly the same manner as described in section 3.4 for the R-critical case.

Fig. 3.8 illustrates an M-critical shock preceded by a Mach 9 shock front. (Again the calculations are for our standard conditions as for the weak R-type case in Fig. 3.4.) For T_{\max} , the photon flux, $F_0 \approx 4.63 \times 10^{22}$ ph/cm²sec, enters the shocked gas with a velocity, $v_3 = 0.200 \times 10^5$ cm/sec ($\xi = 0.968$). For T_{\min} , $F_0 \approx 4.87 \times 10^{22}$ ph/cm²sec and $v_3 = 0.277 \times 10^5$ cm/sec ($\xi = 0.735$). The pressure and compression ratios are still higher than for the D-critical case; the appearance, however, is similar except for the rather weak rarefaction wave which follows the radiation front.

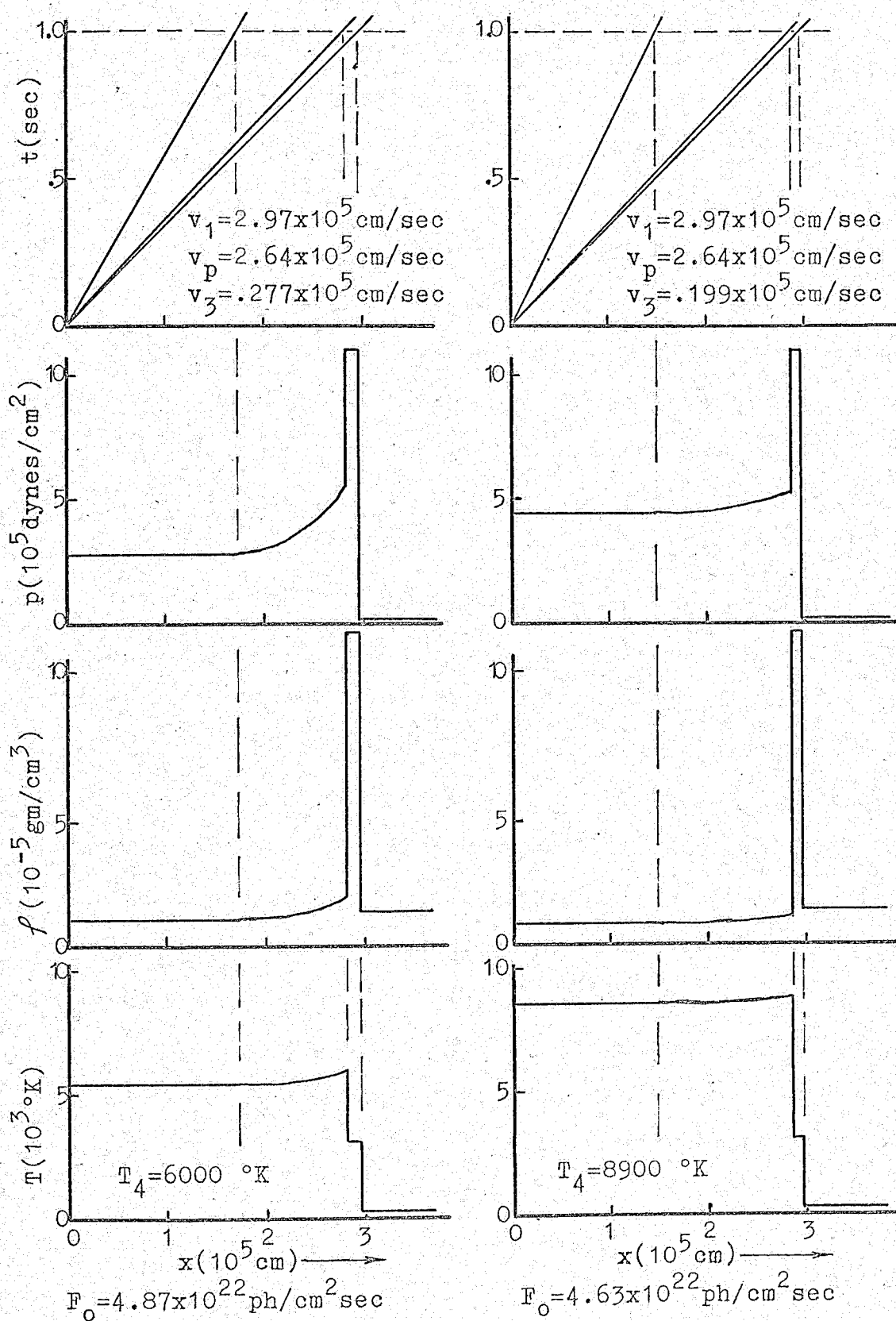


Fig. 3.8 M-critical radiation front preceded by a shock

CHAPTER 4

THE STRUCTURE OF STEADY RADIATION FRONTS

In the last chapter we treated radiation fronts as ideal discontinuities behind which the gas was all dissociated. It was necessary to assume a final temperature in order to calculate the flow associated with the front. The previous results would be unique, if the final temperature could be calculated. We feel that it is one major contribution of this thesis to realize that this temperature can (at least, in principle) be obtained, if all details of the rates of ionization, dissociation and recombination processes within the front are considered, and a stepwise integration across the front is carried out. It is the aim of this chapter to outline such a detailed calculation. As an example we will discuss a dissociation front in oxygen. Again, we consider the radiation front as a one-dimensional steady state discontinuity with energy input.

Unfortunately, it turns out that most of the required rate coefficients are not yet known, and also that the numerical integration is quite difficult (and was actually finally not successful). Therefore, the merits

of this chapter lie more in the outline of a procedure to obtain T_4 than in the production of numerical results. The cohesion of the thesis is not lost, if the reader turns over to section 4.4. He may later return to some parts of this chapter in order to study two definitions which are used in Chapter 7, namely, the local power input and the local degree of dissociation.

4.1 Conservation equations of mass, momentum and energy.

Similar to the treatment of shock front structures (Zel'dovich and Raizer (1966), Chapter VII), we will include viscous forces and heat transfer in our discussion of the radiation front structure. The conservation equations may be written

$$\rho(x) v(x) = \rho_0 v_0 \quad 4.1$$

$$P(x) + \rho(x) v(x)^2 - \frac{4}{3} \mu \frac{dv(x)}{dx} = P_0 + \rho_0 v_0^2 \quad 4.2$$

$$\begin{aligned} h(x) + \frac{v(x)^2}{2} + \frac{1}{\rho_0 v_0} \left(-k \frac{dT(x)}{dx} - \frac{4}{3} \mu v(x) \frac{dv(x)}{dx} \right) - \frac{1}{\rho_0 v_0} \int \rho(x) g(x) dx \\ = h_0 + \frac{v_0^2}{2} \end{aligned} \quad 4.3$$

The terms on the right hand side of these equations are constants of integration, expressed in terms of the initial values of the flow variables, distinguished by the subscript "0". v_0 is the front velocity relative to the particles ahead of the front. μ and κ are coefficients of viscosity and thermal conductivity respectively (one usually assumes that these coefficients are constant.) The term $g(x)$ is the rate of energy input per unit mass such that far behind the front

$$\frac{1}{\rho_0 v_0} \int_{-\infty}^{\infty} \rho(x) g(x) dx = \frac{W}{\rho_0 v_0}, \quad 4.4$$

where $W/\rho_0 v_0$ is the total energy input per unit mass as defined in eq'ns (2.3) and (3.29'). All the other variables are defined as in eq'ns (2.1) to (2.3).

We note that these equations are valid at any point inside the radiation front; in fact, far behind the radiation front these equations are identical with eq'ns (2.1) to (2.3) since the terms containing viscosity and heat conduction vanish.

4.2 Reactions within a radiation front

In general, many kinetic reactions occur within a radiation front. The photodissociated particles tend to recombine either directly by two body or three body recom-

ination or indirectly through a chain process in which "intermediate" stable or metastable compounds are formed. Negative as well as positive ions may occur, atoms and molecules are found in various stages of electronic, vibrational and rotational excitation. Collisions between hot particles within the front tend to cause further dissociations. Finally, at sufficiently high temperatures and radiation intensities the gas in the radiation front absorbs and radiates as a grey body (see Zel'dovich and Raizer, Chapter IX), presumably through an inverse bremsstrahlung mechanism with the free electrons.

If the incident radiation has a black body frequency distribution one could expect each type of particle to absorb in some region of the frequency spectrum. Furthermore, the front may produce its own radiation through free-free or free-bound two body collisions or radiational de-excitations. "Trapping" of resonant radiation may occur.

The various types of particles in the radiation front are generally not in equilibrium with each other such that equilibrium relations (e.g. Saha relations) must be used with caution, if at all. Thus the concentration of each type of particle must, in general, be described by a separate conservation equation.

Let us consider the various mechanisms which occur in a diatomic gas. As pointed out by Zel'dovich and Raizer,

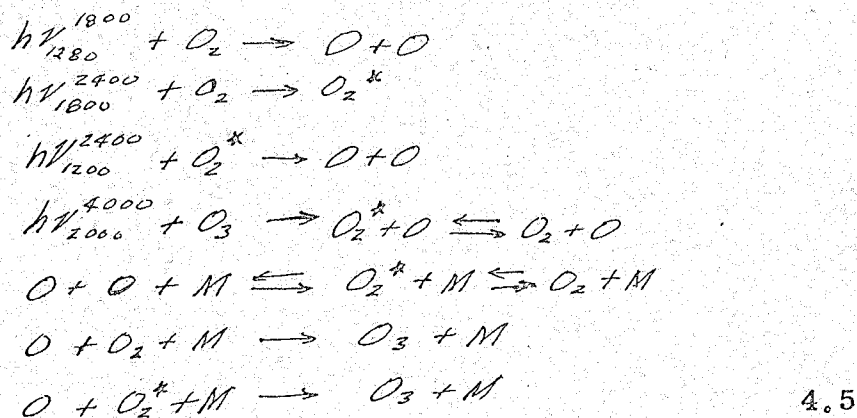
Chapter VI, studies of relaxation times of the various processes behind a shock front indicate the following: Complete equilibrium between the translational, rotational and electronic degrees of freedom is reached after less than 20 collisions per particle (3×10^{-9} sec at atmospheric pressure). It takes a much longer time to reach equilibrium between the vibrational and translational degrees of freedom. Blackman (1956) estimates that 2.5×10^7 collisions at 300°K ($9.6 \mu\text{sec}$ at a standard density of $2.69 \times 10^{19} \text{cm}^{-3}$) and 1.6×10^3 collisions per particle at 3000°K ($0.083 \mu\text{sec}$ at a density of $2.69 \times 10^{19} \text{cm}^{-3}$) are required to reach equilibrium in oxygen. On the other hand, equilibration between the individual vibrational states is extremely rapid (of the order of 20 collisions). Mathews (1959) has determined that behind shock fronts the dissociation time is an order of magnitude larger than the vibrational relaxation time. The collisional dissociation mechanism seems to be due to collisions between a particle in a highly excited vibrational state and a particle with high translational energy. Collisions between molecules in the ground state rarely produce dissociation. Conversely the three body recombination mechanism presumably leaves the molecule in a highly excited vibrational state.

Various types of reactions may occur to produce complex molecules in the radiation front. For example, in oxygen at low temperatures and low degrees of dissociation

atoms tend to combine with molecules to form ozone. (If ionization were present we would also have to consider O_2^+ and O_2^- particles.)

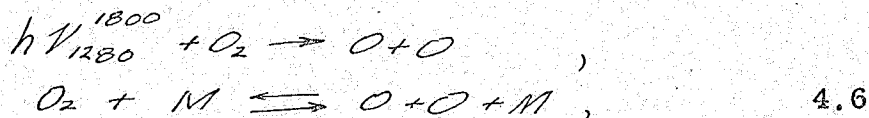
4.3 Special case of a dissociation front in oxygen

To illustrate the concepts let us consider a dissociation front propagating in pure oxygen caused by black body radiation above 1280 \AA (we assume that there is no ionization). We choose a sufficiently high particle density such that excited oxygen atoms are collisionally de-excited and the dominant recombination mechanism is by means of three body collisions. According to the mechanisms outlined in the previous section, the following reactions are dominant:



where M, the third body in the collision stands for any of O, O_2, O_3, O_2^* , the superscript "*" denotes a molecule in a vibrationally excited state, the notation $h\nu_{1280}^{1800}$ indicates that the O_2 molecule has a high photodissociation cross section in the wavelength regions 1280 \AA to 1800 \AA .

The set of reactions above is perhaps not complete; but these reactions clearly illustrate the principle and concepts which we wish to emphasize later. Unfortunately, the reaction rate constants for most of the reactions in eq'n (4.5) are not known. For calculation purposes we further simplify the reaction scheme of eq'ns (4.5) as follows



that is, we neglect ozone formation and vibrationally excited molecules. (A general treatment for the reaction scheme of eq'ns (4.5) is given in Appendix C.)

4.3.1 Conservation equations for absorbing particles. --- Since we only have two types of particles in the reactions eq'ns (4.6), the conservation equations for the atoms and molecules differ only by a factor 2.

$$\frac{\partial N_1}{\partial t} + \frac{\partial u N_1}{\partial x} = -2 \left(\frac{\partial N_2}{\partial t} + \frac{\partial u N_2}{\partial x} \right), \quad 4.7$$

where u is the flow velocity, N is the particle density and the subscripts 1 and 2 denote O and O_2 particles respectively. The conservation equation for the molecules may be written as

$$\begin{aligned} \frac{\partial N_2}{\partial t} + \frac{\partial u N_2}{\partial x} = & - \left/ \frac{\partial F}{\partial x} \right/_{2 \rightarrow 1} - k_{d1} N_2 N_1 - k_{d2} (N_2)^2 \\ & + k_{r1} (N_1)^3 + k_{r2} (N_1)^2 N_2, \end{aligned} \quad 4.8$$

where k is the reaction rate constant and the subscripts d and r denote dissociation and recombination respectively.

The term $\left/ \frac{\partial F}{\partial x} \right/$ in eq'n (4.8) is equal to the number

of molecules which have been destroyed by absorbing photons

and is defined by eq'ns (3.18 and (3.16). We assume that the photon flux is sufficiently small so that the term $(1 + F_0/cN_0)$ may be neglected.* The solution of eq'n (3.18) may be written as

$$\int_{\nu_1}^{\nu_2} F(\nu, x, t) d\nu = \int_{\nu_1}^{\nu_2} F(\nu, 0, t) e^{-\int_0^x \alpha(\nu) N_2(x, t) dx} d\nu \quad 4.9$$

where for a black body radiating at a constant temperature the photon flux entering the absorbing gas is

$$F(\nu, 0, t) d\nu \equiv G(t) F(\nu) d\nu = \text{const } G(t) \frac{\nu^2 d\nu}{e^{h\nu/kT} - 1}, \quad 4.10$$

where (for future reference) we have separated the time variation, $G(t)$, from the frequency dependence $F(\nu) d\nu$.

The mass density of the gas for the case under consideration is

$$\rho(x, t) / M = \frac{1}{2} N_1(x, t) + N_2(x, t) \quad , \quad 4.11$$

where M is the mass of the O_2 molecule. The degree of dissociation y is defined as

$$y = \frac{1}{2} N_1 / \left(\frac{1}{2} N_1 + N_2 \right) \quad , \quad 4.12$$

such that we may write

$$N_2 = (1 - y) \rho / M \quad . \quad 4.13$$

Using eq'n (4.13) in the left hand side of eq'n(4.8) we

have

$$\begin{aligned} \frac{\partial N_2}{\partial t} + \frac{\partial N_2}{\partial x} &= \frac{\rho}{M} \frac{\partial (1-y)}{\partial t} + \frac{(1-y)}{M} \frac{\partial \rho}{\partial t} + \frac{\rho u}{M} \frac{\partial (1-y)}{\partial x} + \frac{(1-y)}{M} \frac{\partial \rho u}{\partial x} \\ &= \frac{\rho}{M} \left(\frac{\partial (1-y)}{\partial t} + u \frac{\partial (1-y)}{\partial x} \right) \quad , \end{aligned}$$

* Actually the term $(1 - v_F/c) = (1 + F_0/cN_0)$ is appropriate only if we have a steady radiation front. In general, one should omit this term and write the photon flux as $F(\nu, x, t')$, where t' is the retarded time, $t' = (t - x/c)$.

since $\partial p / \partial t + \partial(pu) / \partial x = 0$. Thus eq'n (4.8) can be written in terms of the more usual thermodynamic variables as

$$\begin{aligned} \frac{p}{M} \left(\frac{\partial(1-y)}{\partial t} + u \frac{\partial(1-y)}{\partial x} \right) &= -(1-y) \frac{p}{M} \int_{y_1}^{y_2} \frac{1}{\alpha(u)} F(y, \rho, t) e^{-\int_0^x \alpha(z) (1-y) \frac{p}{M} dz} dy \\ &- k_{d1} \frac{p^2}{M^2} (1-y)(2y) - k_{d2} \frac{p^2}{M^2} (1-y)^2 \\ &+ k_{r1} \frac{p^3}{M^3} (8y^3) + k_{r2} \frac{p^3}{M^3} (4y^2)(1-y) \end{aligned} \quad 4.14$$

where we have differentiated eq'n (4.9) to obtain the first term on the right hand side.

Collisional dissociation and three body recombination coefficients in oxygen have been measured by various workers (Rink et al (1961), Comac and Vaughan (1961), Mathews (1959)). The reaction rate constants depend only on the temperature and are related to each other by the principle of detailed balancing

$$\frac{k_{d1}}{k_{r1}} = \frac{k_{d2}}{k_{r2}} = K(T) = A T^{-1/2} e^{-D/kT} \quad (\text{moles/cm}^3), \quad 4.15$$

where $K(T)$ is the equilibrium constant, which determines the equilibrium degree of dissociation y at a given temperature and density; A is a constant. Although eq'n (4.15) is strictly valid for an equilibrium situation, presumably it is also, at least approximately, valid for non equilibrium situations (Hurle (1967)).

The dissociation coefficient is assumed to be of the form

$$k_d = B \left(\frac{p}{kT} \right)^n \exp(-D/kT) \quad , \quad 1.0 < n < 3.0 \quad , \quad 4.16$$

where B is some constant, D is the dissociation energy and the exponent n is believed to have a value between one and

three. The value of n is difficult to determine since the temperature dependence is swamped by the exponential term.

The oxygen atom is roughly three times as effective as a molecule in recombination reactions, thus using the values of Rink et al (1961) and a value of $A = 115 \times 10^3$ we obtain

$$\begin{aligned}
 3.06 \times 10^{-3} T^{-3/2} e^{-D/kT} & \left(\frac{\text{cm}^3}{\text{particle sec}} \right) & = & k_{d2} \\
 9.18 \times 10^{-3} T^{-3/2} e^{-D/kT} & \left(\frac{\text{cm}^3}{\text{particle sec}} \right) & = & k_{d1} \\
 4.4 \times 10^{-30} T^{-1} & \left(\frac{\text{cm}^6}{\text{particle}^2 \text{ sec}} \right) & = & k_{r2} \\
 13.2 \times 10^{-30} T^{-1} & \left(\frac{\text{cm}^6}{\text{particle}^2 \text{ sec}} \right) & = & k_{r1}
 \end{aligned}$$

4.17

We must emphasize that these values were obtained from shock wave studies in oxygen near 4000 °K and the exponent (-1) in the equations for k_{r1} was used by Rink et al to obtain an approximate temperature dependence. It may, in fact, be as large as (-3) and small as (-1/2). Consequently, at room temperature the values of k_{r1} obtained from eq'ns (4.17) may be significantly in error. Nevertheless we shall use these values for calculations in the thesis.

4.3.2 The rate of energy input per unit volume,

$\rho(X, t) q(X, t)$. --- The energy input for radiation fronts or radiation produced shocks is through absorption of photons. For high radiation intensities and low number densities (corresponding to weak R-type conditions) there is little particle motion so a knowledge of the energy input at any

point in space and time is not necessary. Nevertheless, if recombination of the particles behind the radiation front is negligible this energy input may be easily calculated in a manner analogous to the methods outlined in section 3.1. If recombination is not negligible then the calculation is much more complicated and furthermore depends upon whether the recombination is due to two body collisions with resulting photon emission or due to three body collisions with no emission.

Recombination of the particles would tend to broaden the radiation front and distort the energy input across the front since the photons of high absorption cross section would tend to be absorbed by the recombined particles which presumably are formed relatively far behind the leading edge of the front. Also, if the particle density is relatively low (10^{16} cm^{-3}) the dominant recombination mechanism is by two body collisions with photon emission. This results in substantial "diffusion" of radiant energy in the vicinity of the front and it is necessary to employ the theory of radiative transfer (Chandrasekhar (1960)) to obtain the net energy input at any point in space and time.

In weak D-type fronts preceded by shocks there is substantial motion of the gas and therefore a knowledge of the energy input at every point in space and time is of dominant importance if one wishes to analyze the development of a radiation or shock front or the structure of a

steady state radiation front.

The rate of energy input for the reaction scheme in eq'n (4.6) is obtained directly from the $\left| \frac{\partial E}{\partial x} \right|$ term as defined in eq'ns (4.8) and (4.9) simply by replacing the photon flux F with the energy flux E . (See Appendix C for the general case.) The relation between the energy flux and photon flux

$$E(x,t) \equiv \int_{\nu_1}^{\nu_2} E(\nu, x, t) d\nu = \int_{\nu_1}^{\nu_2} h\nu F(\nu, x, t) d\nu \\ = \int_{\nu_1}^{\nu_2} h\nu F(\nu, 0, t) e^{-\int_0^x \alpha(\nu) N_2(x,t) dx} d\nu, \quad 4.18$$

where we have used eq'n (4.9) and where $F(\nu, 0, t) d\nu$ is defined by eq'n (4.10). Thus differentiating eq'n (4.18) we obtain

$$Iq \equiv \left| \frac{\partial E}{\partial x} \right| = N_2 \int_{\nu_1}^{\nu_2} \alpha(\nu) h\nu F(\nu, 0, t) e^{-\int_0^x \alpha(\nu) N_2(x,t) dx} d\nu, \quad 4.19$$

which in the notation used in eq'n (4.14) is

$$Iq = (1-g) \frac{I}{M} \int_{\nu_1}^{\nu_2} \alpha(\nu) h\nu F(\nu, 0, t) e^{-\int_0^x \alpha(\nu) (1-g) \frac{I}{M} dx} d\nu. \quad 4.19'$$

In general, if there is more than one type of absorbing particles in the radiation front, an equation similar to eq'n (4.19) must be written for each type. This is illustrated in Appendix C for the reaction scheme shown in eq'ns (4.5).

4.3.3 Calculation of the front structure. --- For given boundary conditions one can, in principle, calculate the structure of a steady radiation front from eq'ns (4.1), (4.2) and (4.3) where to evaluate the term $\int \mathcal{L}(x) q(x) dx$ in eq'n (4.3) it is necessary to use eq'ns (4.19') and (4.14).

For a steady radiation front one replaces the time derivative with the spatial derivative $\partial/\partial t \rightarrow -v_F \partial/\partial x$, where v_F is the velocity of the front, such that the left hand side of eq'n (4.14) becomes

$$\frac{\rho}{M} \left(\frac{\partial(1-\beta)}{\partial t} + u \frac{\partial(1-\beta)}{\partial x} \right) \rightarrow \frac{\rho}{M} (u - v_F) \frac{\partial}{\partial x} (1-\beta) \equiv \frac{\rho v}{M} \frac{\partial}{\partial x} (1-\beta), \quad 4.20$$

where $v = u - v_F$ is the particle velocity relative to the front.

An attempt was made to calculate the structure of a weak D-type front in oxygen preceded by a Mach 3 shock front. For this we used eq'ns (4.1), (4.2), (4.3), (4.14) and (4.19') as well as the equation of state. In this manner we hoped to obtain a value of the temperature behind the radiation front which we had assumed for the calculations in Chapter 3. The procedure was to divide up the radiation front into equal sections (in Lagrangian co-ordinates) with the first section at the point where the photon flux was 1% of the initial value. Calculations were then carried out for each succeeding section. First, the degree of dissociation was calculated from eq'n (4.14), ρq was calculated from eq'n (4.19') and $v^2/2$ from eq'n (4.3). Unfortunately, the iterative procedure did not converge -- negative values of the density and imaginary values of the velocity always occurred. Perhaps this is hardly surprising since the $v^2/2$ term is about 10^4 times smaller than the ρq and the h terms in eq'n (4.3) -- our iterative procedure could hardly be expected to produce such accuracy. Perhaps some other cal-

calculation procedure would prove to be more satisfactory. However, further work in this direction was abandoned.

We shall return briefly to this problem in Chapter 7, where we will use the equations developed in this section.

4.4 Concluding remarks on Chapters 2, 3 and 4

In the previous chapters we have treated steady radiation fronts propagating in a semi-infinite tube and showed that five different types of fronts were possible. In Chapter 3 we carried out detailed calculations (for an assumed temperature, T_4) for each of the five types of radiation fronts which occur. We would like to stress one of the most interesting phenomena: Radiation fronts may act like driving pistons to accelerate the gas ahead of them. The results are best presented by plotting the velocities v_p , v_f and v_s as a function of N_0/F_0 . The diagrams in Fig. 4.1 show such a plot. The values of these curves were obtained from Figs. 3.4 to 3.8 which were calculated for standard conditions as outlined in section 3.3.

In Chapter 4 we introduced concepts and equations to calculate the structure of any steady radiation front with given boundary conditions. In this way it is possible, in principle, to calculate the final temperature behind the front so as to make the solutions of Chapter 3 and the relations presented in Fig 4.1 unique in terms of the final temperature.

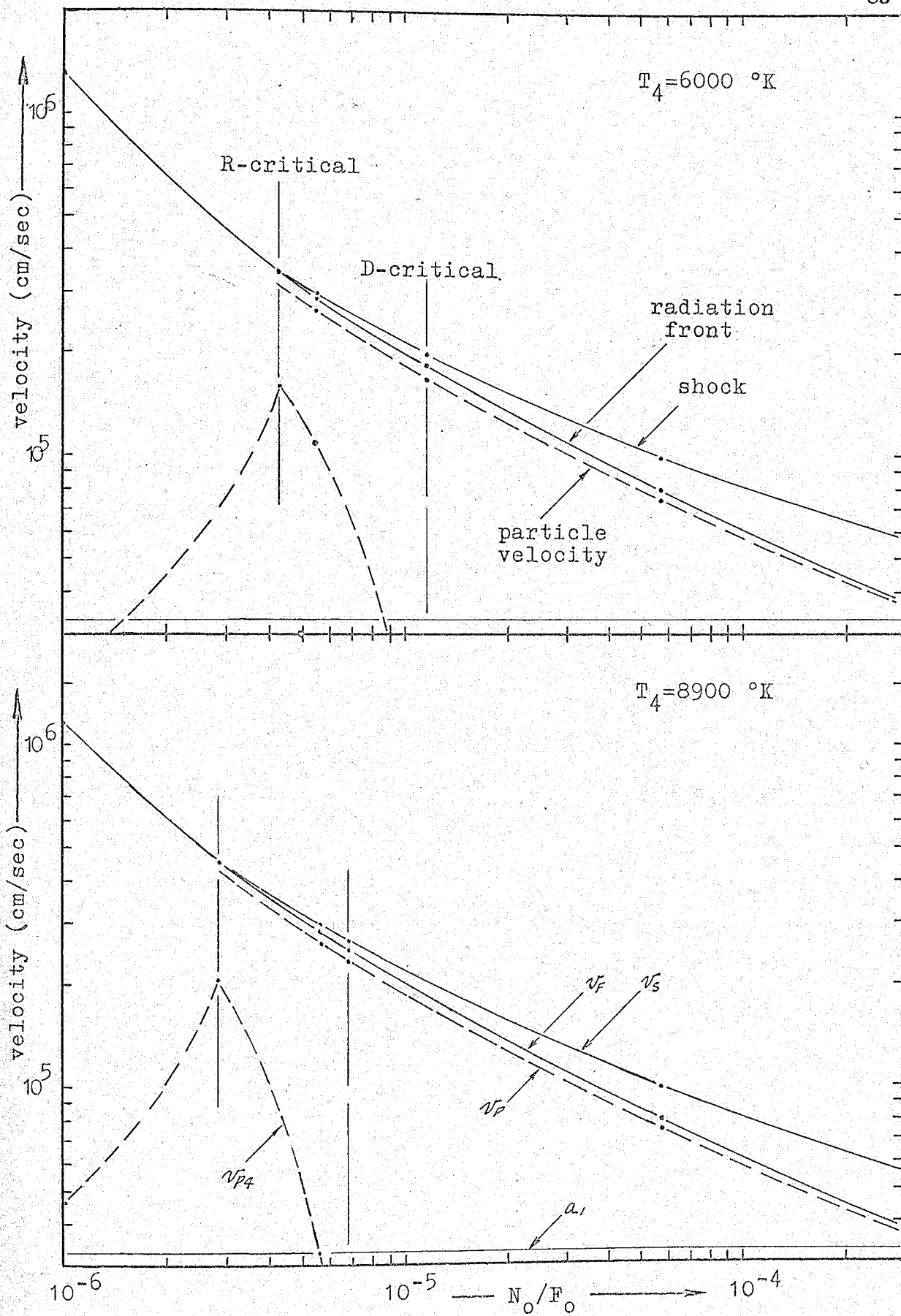


Fig.4.1 Plot of velocities versus N_0/F_0 for T_{\min} and T_{\max}

This, in effect, yields an additional equation so that now there are as many equations as unknowns (see section 2.5) and, therefore, no assumptions are necessary. Although we failed to obtain a numerical solution for a simplified case we believe that the ideas developed in this chapter and Appendix C will point the way to successful calculation in the future.

We have intimated several times that in the strictest sense of the word steady radiation fronts do not occur in real gases. All radiation fronts will possess non steady state characteristics to some degree. The application of steady state equations to radiation fronts will yield approximate results - in some cases quite accurate and in others, less reliable. However, even in obviously non steady state situations, the results of these chapters are useful in estimating the properties of and thermodynamic quantities associated with the radiation front.

In the next two chapters we describe an experiment which matches the geometry, which we have considered throughout this thesis. In trying to understand the details of our experimental results we found it necessary to consider aspects of non steady radiation fronts. Consequently, in Chapter 7 we develop a method to consider such fronts.

CHAPTER 5

THE BOGEN LIGHT SOURCE

Having treated steady radiation fronts in the first part of this thesis we will now focus our attention on an experiment to produce radiation fronts in the geometry of Fig. 2.1.

An extremely intense light source radiating in a wavelength region where the photoabsorption cross section of the test gas is large is a necessary requirement for experimental work on radiation fronts. An ideal source would be a powerful pulsed laser radiating at the desired frequency and for a period of several tens of microseconds. Comparison of the experimental results with the theory for such a monochromatic source would be much simpler than for a black body source.

Unfortunately such ideal lasers are not available at present. For our experiments we choose a light source similar to that described by Bogen et al (1965). This source consists of an arc constricted through a narrow channel in a polyethylene rod and radiates as a black body with an effective temperature of the order of 10^5 °K for a period of about 10μ sec.

5.1 Description of light source

The light source is illustrated schematically in Fig. 5.1. A 25 μ F capacitor bank capable of being charged to 20 kV is discharged through a 2 - 4 mm diameter hole drilled through a 4.2 cm long polyethylene rod. The discharge, squeezed through the hole, vaporizes the polyethylene at the walls and produces an extremely hot, high density plasma which radiates along the axis of the hole as a black body. The radiation passes into the test chamber either directly or through a glass, quartz or LiF window.

Unfortunately much of the polyethylene plasma consists of vaporized carbon which tends to settle on the walls of the chamber and on the window. Consequently it is necessary first to remove the test chamber as far from the source as practical, secondly, to insert baffles between the source and the test chamber and thirdly to use large dump chambers to disperse the spent plasma. Otherwise, the window must be cleaned after every one or two shots.

The sequence of events in firing the light source is as follows: The system is pumped down to below 0.05 Torr which is sufficiently low to ensure that breakdown does not occur. The condenser bank is charged to the desired value (usually 3 kV). The light source is fired by directing a jet of helium onto the hole in the polyethylene. This raises the pressure until for the applied voltage a point

on the Paschen curve is reached where breakdown occurs. The spent plasma and excess helium are pumped out and the whole process may be repeated every 30 to 60 seconds. After about 1000 shots the discharge channel becomes enlarged and the polyethylene must be replaced.

An alternate method of triggering the discharge would be supplying a pulse of approximately - 12 kV at the negative electrode by means of a brush cathode. This method was not used since the electrical noise associated with the triggering pulse tended to trigger the oscilloscope prematurely.

Various designs of the light source were tried before the design illustrated in Fig. B1, Appendix B was successful. It consists of two electrodes embedded in and

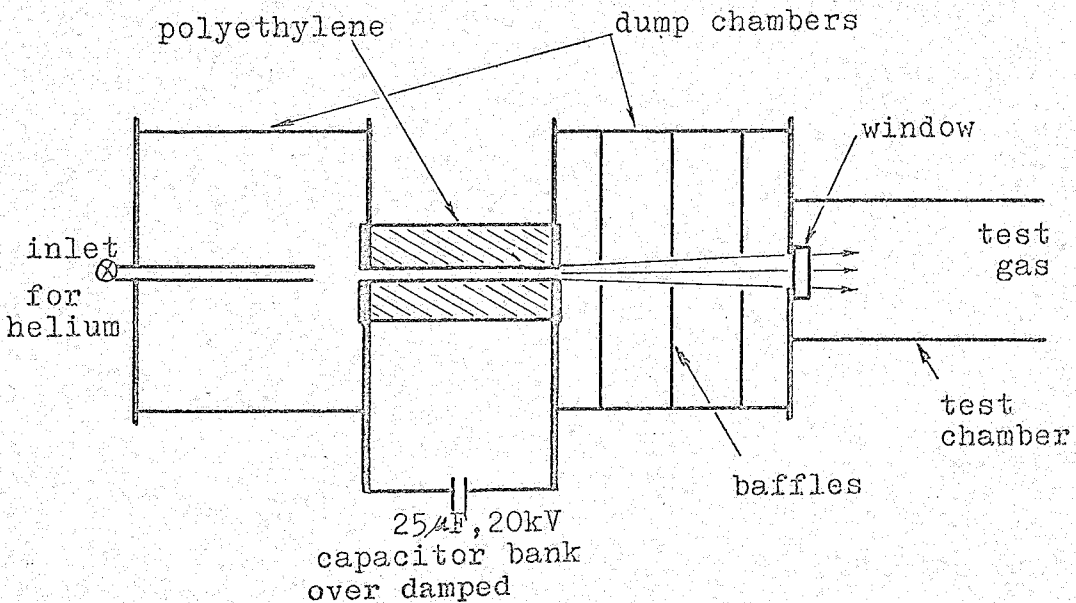


Fig. 5.1 Schematic representation of light source

separated by epoxy strengthened with fibreglass. A 3/4" diameter threaded polyethylene rod is screwed into the epoxy such that the 2 - 4 mm diameter hole serves as the axis of the cylindrically symmetric apparatus.

Although this design was quite satisfactory the polyethylene tends to crack after many shots especially at relatively high discharge voltages, ($\approx 7kV$). Also, the ringing frequency of the bank decreases as the discharge channel in the polyethylene increases in diameter. Consequently, the light intensity was not strictly reproducible from shot to shot and the peak intensity tended to become delayed after many shots were fired.

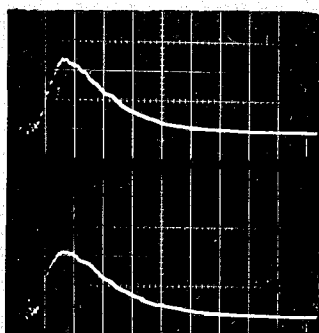
The dump chambers consisted of 6 inch diameter aluminum tubing of various lengths (2 inches to 12 inches) sealed with O - rings.

The LiF and quartz windows were 1/4" thick by 1" diameter; the actual aperture for the radiation entering the test chamber was 1.7 cm diameter. A mechanical shutter consisting of sheet metal, was installed to stop the light from entering the test chamber. It was operated from outside the chamber by means of a magnet.

5.2 Measurement of intensity

A typical oscilloscope trace of the light pulse is shown in Fig. 5.2. The peak intensity of the light pulse

was measured as a function of wavelength and as a function of discharge voltage.



2 v/div; $\frac{2}{5}$ μ sec/div
 $\lambda = 5000 \text{ \AA}$; discharge voltage = 2.5kV

Fig. 5.2 Light pulse from Bogen source

5.2.1 Absolute intensity at 5000 \AA with discharge voltage at 3.0 kV. -- The absolute intensity was measured by comparison with a standard carbon arc (made by Leybold, with Ringsdorf RW 202 anode and RW 401 cathode). The arc was operated as prescribed by Null and Lozier (1962) The experimental setup is indicated in Fig. 5.3. Care was taken to ensure that the optical systems were identical for the two light sources. This was accomplished by means of a mirror-- first measuring the intensity of one system, rotating the mirror by 90° and measuring the intensity of the other system.

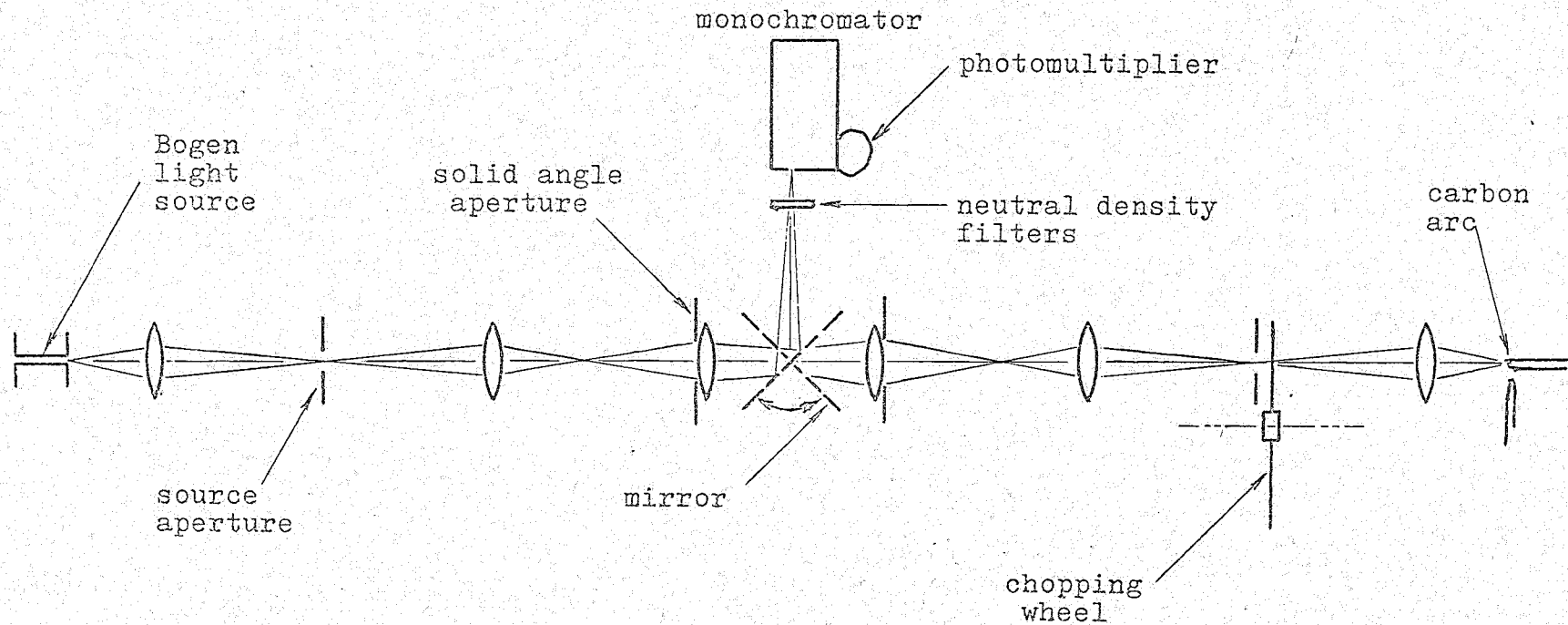


Fig.5.3 Experimental setup for absolute intensity measurements

By adjusting the size of the source aperture (see Fig. 5.3) it was possible to adjust the effective size of the light sources. By adjusting the solid angle aperture it was possible to measure the intensity of the Bogen light source as a function of solid angle. Measurements show that the intensity per unit cross-section tends to decrease slightly with the size of the hole in the polyethylene insert. The optimum size (at a discharge voltage of 3.0kV and at a wavelength of 5000 \AA) was found to be approximately 4 mm. Measurements also show that the light from the Bogen source is concentrated in quite a narrow beam in the axial direction since the intensity per unit solid angle decreases markedly for large solid angles (perhaps by a factor 3 for $\Omega \approx 0.1$ sterad).

Measurements indicated that at 3.0 kV and 5000 \AA the average intensity of the Bogen light source for a solid angle of 0.1 sterad was $(1.9 \pm 0.2) \times 10^3$ times as bright as the carbon arc. Along the axis this value is roughly three times larger. Since the carbon arc intensity at 5000 \AA is 200 watts/($\text{cm}^2 \text{ster } \mu$) we calculate that at the source aperture we have a photon flux of about 3.6×10^{21} photons/($300 \text{ \AA} \text{ cm}^2 \text{sec}$) (for $\Omega = 0.064$ and area magnification of 5.3). From Stefan's law the effective black body temperature of the Bogen source is in the region 60,000 °K to 150,000 °K depending on the solid angle.

5.2.2 Intensity as a function of wavelength at 3.0 kV. -- To measure the intensity in the wavelength region from 2500 Å a procedure similar to that described above was used. However, no lenses were used and the neutral density filters were replaced by a set of frosted quartz windows (the transmission of the various combinations was measured as a function of wavelength prior to intensity measurements). The measurements show that the intensity of the Bogen source gradually increases with wavelength to a value of 4.2×10^6 watts/(cm²ster μ) at 2500 Å (i.e. about 10 times larger than at 5000 Å). Unfortunately the intensity of the carbon arc is very small at 2500 Å and accurate measurements are difficult. Nevertheless by comparison with Planck black body radiation the values of the intensities at 2500 Å indicate an effective black body temperature of the order of 40,000 °K.

5.2.3 Intensity as function of discharge voltage. -- At low voltages the intensity of the Bogen light source increases quite linearly. However, at higher voltages it tends to increase more slowly indicating a saturation level is being reached, at around 6 kV. Also this saturation level seems to be larger for larger diameters of the channel in the polyethylene insert. A typical curve of intensity versus discharge voltage is shown in Fig. 5.4. From this curve it

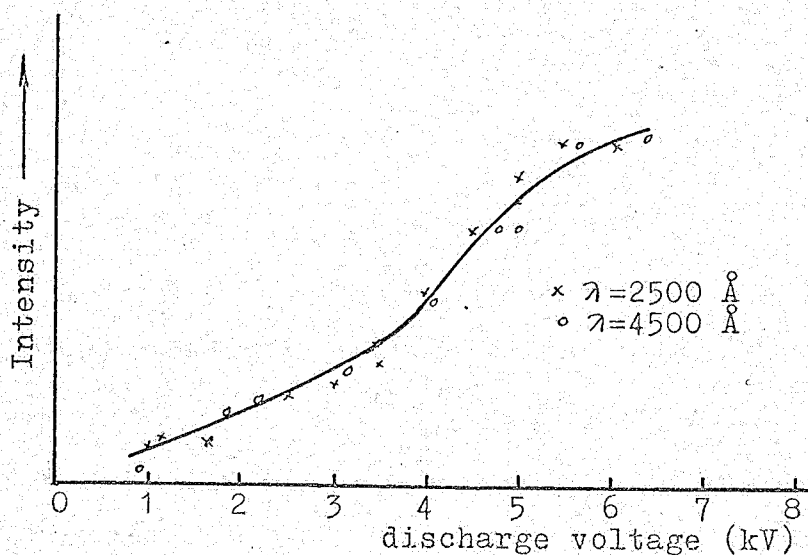


Fig. 5.4 Intensity of Bogen light source as a function of discharge voltage.

appears that the optimum discharge voltage is around 5 to 6 kV. Unfortunately, unless the window is very far from the light source, it gets badly chipped at these voltages; consequently, it was preferable to use lower discharge voltages and place the window closer to the light source.

CHAPTER 6

EXPERIMENTS AND RESULTS

Throughout our theoretical investigations we have considered steady radiation fronts which are generated in a semi infinite tube sealed by a transparent window. For experiments with ionization fronts one must use a window which transmits photons of energy below the ionization potential of the test gas (e.g. the ionization limit of hydrogen atoms is 912 \AA). We know of no material which transmits radiation at such low wavelengths. Lithium flouride, which transmits radiation down to a wavelength of about 1200 \AA has the lowest cut off limit. Consequently we could only study dissociation fronts in test gases which have photodissociation cross sections in a wavelength region above 1200 \AA . Iodine and oxygen fulfill this requirement and were used as test gases.

When we examine the temporal variation of the light pulse from the Bogen source, we find that it is of much too short a duration for a steady dissociation front to develop. Therefore it was decided to study two phenomena (i) the beginning of the formation of the radiation front at low absorber densities during the time of the light pulse and (ii) the formation of shocks at high absorber densities after the light pulse was over. Such experimental

investigations are described below.

6.1 Beginning of formation of dissociation front in iodine

An experiment to observe the beginning of the formation of a radiation front requires a test chamber of finite length (see Fig.6.1). If we choose a test gas which absorbs in the visible wavelength region (where we may use conventional monochromators, filters and photomultipliers), it is possible to measure the amount of light passing through the test chamber. An increase with time in the amount of radiation passing through the test chamber relative to the radiation incident on it (i.e. an increase in transmission) indicates the development of a dissociation front. Furthermore, if the conditions correspond to a weak R-type case (see Chapter 3) or if the predicted width of a steady radiation front corresponding to such conditions is wide (such that the pressure gradient is small), then there will be little motion of the particles during the $10\mu\text{sec}$ light pulse and, therefore, the interpretation of the results is simplified.

To carry out such an experiment iodine was chosen as the test gas since it is photodissociated by radiation in the region 4600 \AA to 5000 \AA . It has a photoabsorption cross section of $2.4 \times 10^{-18}\text{ cm}^2$ at 4995 \AA (see results of

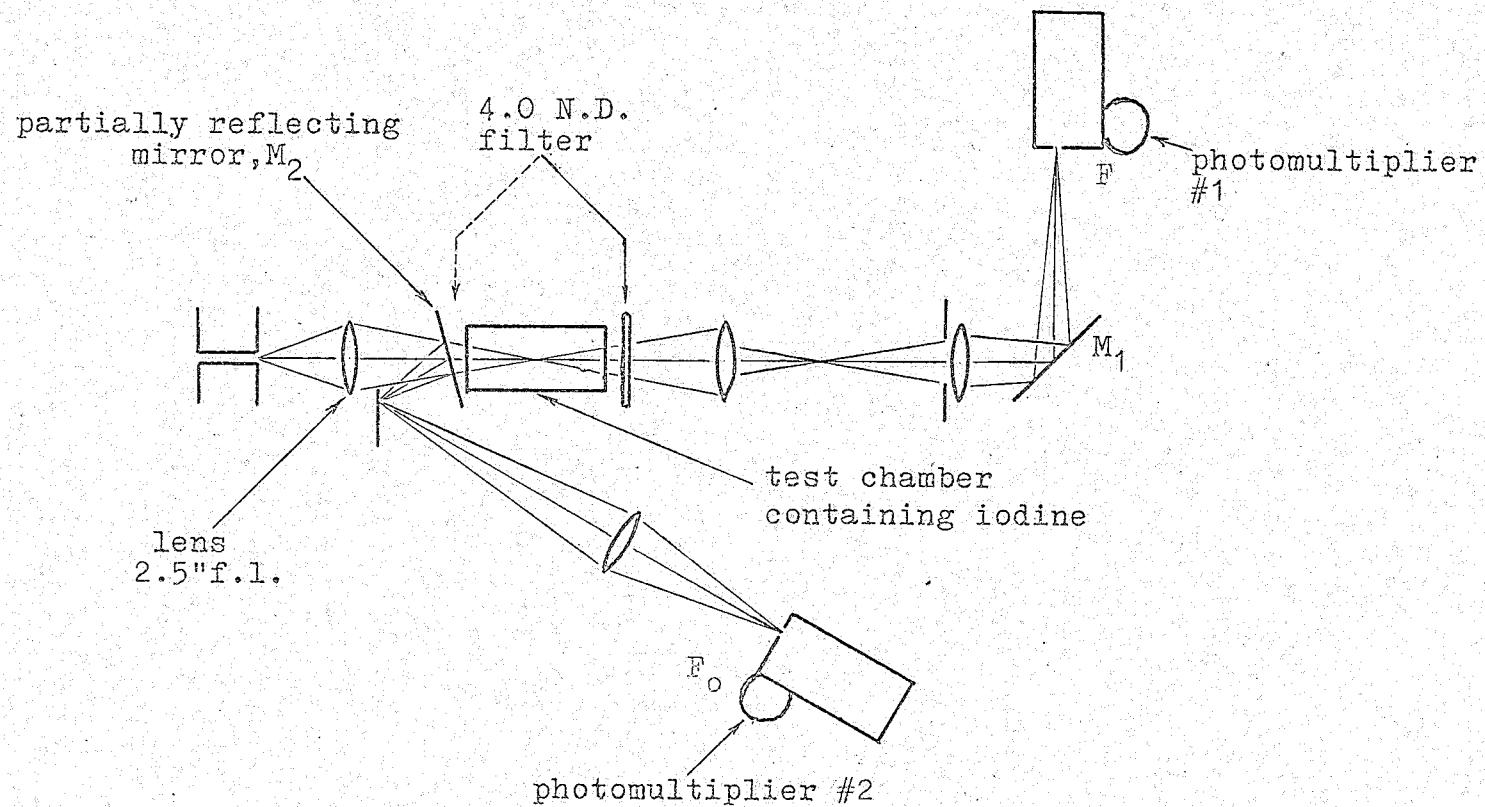


Fig.6.1 Schematic representation of experiment with iodine

Rabinowitch and Wood (1936) in Fig.B.2, Appendix B) and a recombination coefficient of $7.6 \times 10^{-30} \text{ cm}^6/\text{molecule}^2\text{sec}$ for three body recombination with I_2 particles as the third body (Porter and Smith (1961)). There were three conditions to satisfy in the choice of the length of the test chamber and the initial pressure so as to obtain a maximum in the variation of the transmission. First we wanted about 90% of the radiation at 4995 Å to be absorbed within the chamber since for this case the signal to noise ratio (Δ transmission: transmission) was large. Secondly, we wanted to use a short focal length lens to focus the light into the test chamber and thus obtain a large photon flux, F_0 . This dictated the use of a short test chamber. On the other hand, the chamber could not be too short since this would require the use of high particle densities at which three body recombination would not be negligible. To satisfy these conditions we chose a test chamber 10 cm in length and used a particle density of 1.12×10^{17} particles/ cm^3 .

The test chamber was a 3.5 cm diameter evacuated glass cell (containing iodine crystals) enclosed in a brass container which was equipped with heating elements to control the temperature. The particle density of the iodine vapor was regulated by adjusting the temperature of the cell. We used 70 ± 0.5 °C which corresponds to $[\text{I}_2] = (1.12 \pm 0.03) \times 10^{17} \text{ cm}^{-3}$.

The experimental setup, is shown in Fig.6.1. It has an optical system similar to the arrangement for measuring the absolute intensity of the Bogen source (see Fig. 5.3). A 2.5" focal length lens was used to seal the dumping chamber of the Bogen source and also to focus the radiation into the test chamber (with an area magnification of 5.3). It was necessary to clean this lens after every four shots. The transmitted light F passed into a monochromator and was measured by photomultiplier #1. A plane glass plate was inserted to divert a small fraction of the incident radiation, F_0 , into a second monochromator and photomultiplier #2 which served as a monitor. A $D=4.0$ neutral density gelatin filter could be placed either in front of or behind the cell.

Since the difference between the signals F and F_0 is small and, furthermore, not reproducible, it was necessary to use a differential technique. The experimental procedure is as follows: The neutral density filter is placed in front of the iodine cell and the amount of light, F_0 , entering phototube #2 (at 4995 Å) is adjusted to reasonable levels and equalized to F entering phototube #1 by means of additional neutral density filters (not shown in Fig. 6.1). The difference of these two signals is displayed on an oscilloscope, (ideally this difference should be zero, but in practise this never occurs) and recorded on polaroid film. The 4.0 N.D. filter is then placed behind the iodine cell and the procedure repeated. If there is substantial depletion

of the I_2 molecules in the cell during the time of the light pulse, the signal from phototube #1 should be larger than the signal of the monitor. The difference in these two signals is a measure of the development of the radiation front.

Typical oscilloscope traces are shown in Fig. 6.2. Unfortunately the signals are not reproducible and in order to obtain a meaningful measurement it was necessary to average measurements over 12 shots. The results are shown in Fig. 6.3. The solid error bars indicate the standard deviations. The dashed error bars indicate the results obtained with no iodine vapor in the cell (accomplished by keeping the cell at liquid nitrogen temperatures) for which we should obtain a straight line along the horizontal axis. The deviation from the expected result and the large error bars are testimony of the difficulty in detecting the radiation front in this experiment.

The two solid curves in Fig. 6.3 give upper and lower limits for the expected theoretical results.* Here we used a photon flux $F_0 = 1.44 \times 10^{22}$ ph/300 Å cm²sec) and a photon flux half this value (corresponding to the results of section 5.2 using solid angles of 0.256 steradians and 0.128 steradians). The calculations are carried out as outlined in Chapter 7. (Drift motion and diffusion of the particles as well as wavelength dependence of the absorption cross section were neglected. Also, the radiation was assumed to be parallel.) Despite the obvious shortcomings of the

* Rather than plotting the original and the increased flux which differ only by about 5%, we gave the expected differences of both signals in Fig. 6.3.

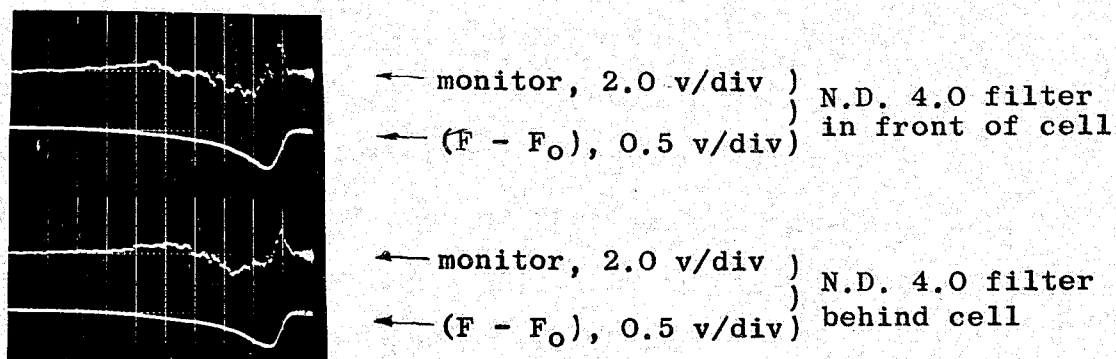


Fig. 6.2 Typical oscilloscope traces for measurements in iodine.

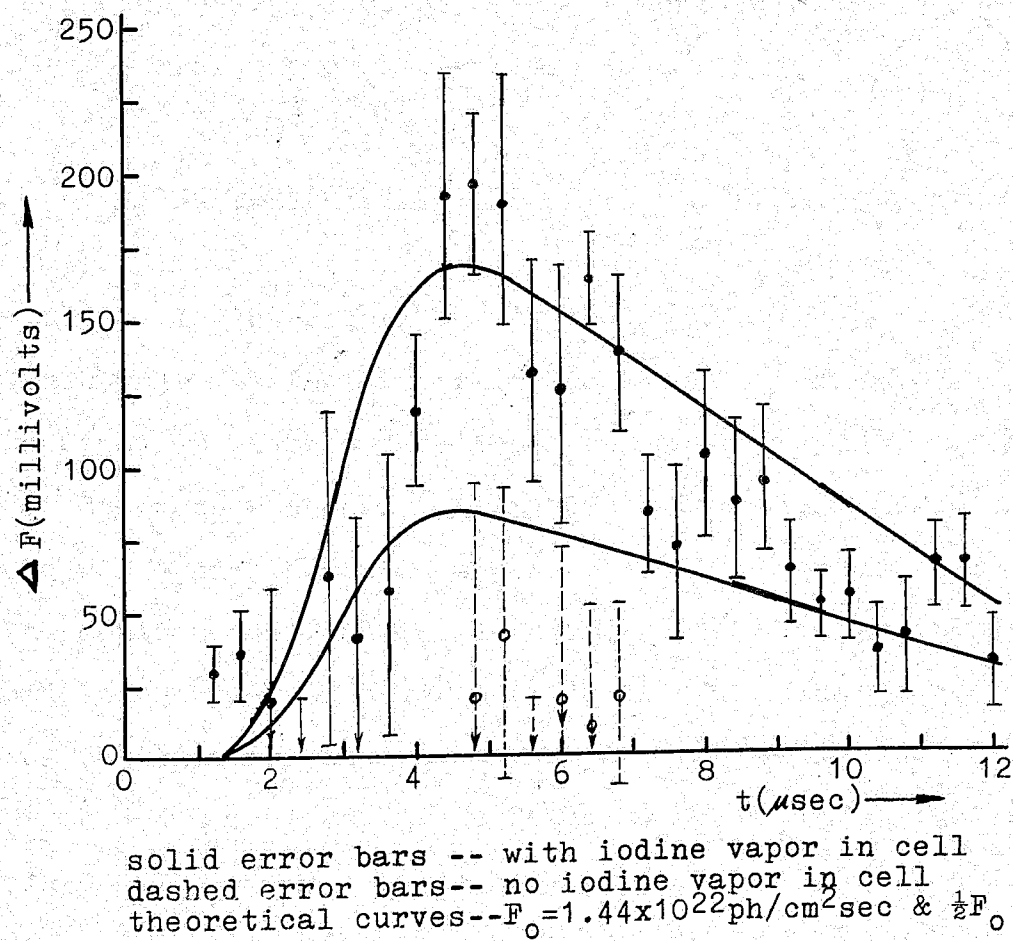


Fig. 6.3 Increase in light intensity during of light pulse

measurements and theoretical curves there is general agreement between theory and results. We would like to emphasize the difficulties encountered in these measurements -- the intensity and time duration of the light pulse from the Bogen source were simply insufficient to measure the development of the radiation front precisely.

In concluding this section the author would like to suggest that an experiment similar to the one described above but using a strong d.c. light source be attempted. (Possibly a large carbon arc such as are used as projectors in drive-in theatres would be satisfactory). Also, other gases (or mixtures of gases) such as chlorine, bromine and sulphur dioxide may be preferable as test gases.

6.2 Shock fronts in oxygen

In the experiment in iodine a low density was used such that little particle motion could be expected. In this section we wish to accentuate the dynamics of the test gas so as to produce shocks.* As shown in Chapters 3 and 4 one has to use a high absorber density and a test gas with a high absorption coefficient in order to produce significant particle motion over short periods of time. Oxygen was chosen as test gas for this purpose. It has a high photodissociation cross section in the Schumann Runge region from about 1280 Å to 1800 Å (see results of Metzger and Cook (1964), Fig. 8.3, Appendix B); its maximum value of $14.9 \times 10^{-18} \text{ cm}^2$

* Similar shocks were reported by Elton, (1964).

at 1420 Å is six times larger than the value for iodine at 4995 Å. Also the particle densities used were in the region of 10^{18} cm^{-3} to $2.69 \times 10^{19} \text{ cm}^{-3}$, substantially higher than for the case of iodine. Consequently, a radiation front tends to be much narrower than in the case of iodine and the pressure gradients much larger.

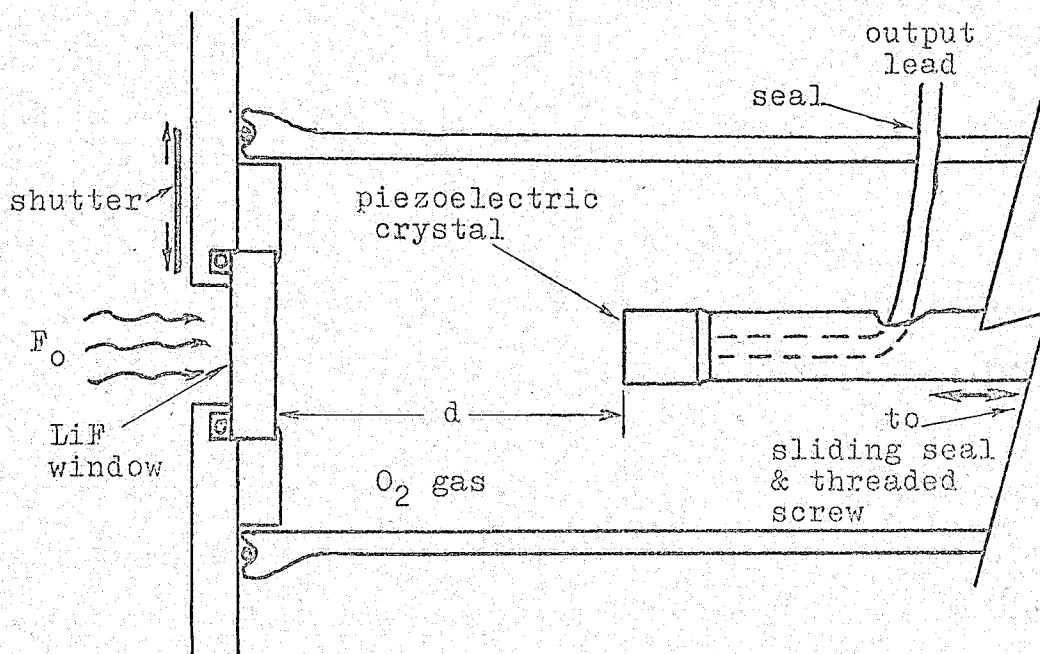


Fig. 6.4 Schematic of experiment in oxygen.

The experimental setup is illustrated in Fig. 6.4. The test chamber consisted of a 2" diameter pyrex T-junction filled with oxygen at the desired pressure. The radiation passes through the 1.7 cm diameter opening in the lithium fluoride (LiF) window, is absorbed in the oxygen gas and produces a shock which travels in the +x direction.*

* Since there are no containing walls it also tends to disperse outwards in the radial direction. However, this seems to have no effect on the axial propagation of the shock since a 1.8 cm I.D. tube inserted to prevent this diffusion resulted in no detectable difference in the strength of the shock.

A piezo electric pressure probe, (pressure transducer LD-15/89 of the Atlantic Research Corp., Alexandria, Va.) was placed directly facing the incoming radiation, the distance between it and the LiF window could be adjusted to any desired value by means of a threaded screw. The face of the piezo probe was coated with aluminum paint to prevent the radiation from falling directly onto the crystal. This probe measured the time of arrival and strength of any shocks or compression waves which were formed.

The procedure was simply to set the piezo probe at any desired distance d , fire the Bogen source and record the signal from the piezo probe as displayed on an oscilloscope. (It was necessary to clean the LiF window after every 6 shots.) Typical traces are shown in Fig. 6.5. We notice that the sharp shock signals are superposed on a long duration slowly decaying signal. This signal is presumably due to thermal heating of the crystal when radiation (above 2000 \AA) strikes and is absorbed by the face of the probe. In fact, the amplitude of this signal proved to be a convenient way of monitoring the intensity of the radiation passing through the LiF window. The secondary peak which appears after the primary signal is due to the reflected shock (from the piezo probe, back to the LiF window and back to the piezo probe).

From these signals we may calculate the speed and initial point of formation of the shock at various pressures. We find that at high pressures (600 Torr) the shock forms very near the LiF window while at low pressures, (20 Torr) the

distance d must be at least one centimeter before a signal can be detected. In general, as the distance d is increased the amplitude of the signal first increases to a maximum and then decreases gradually. Presumably this indicates that the compression wave initially builds up in strength to a maximum and then slowly decays. This is illustrated in Fig. 6.6 for an initial pressure of 400 Torr at which the maximum is at about 0.5 cm. We will examine these results in more detail in Chapter 7.

The velocity of the shocks at all pressures is 364 ± 8 m/sec. In fact, the velocities at low pressures seemed to be slightly larger than at high pressures but certainly no more than 8 m/sec. The time of arrival of the shock as a function of distance d is plotted in Fig. 6.7 for an initial pressure of 400 Torr. From the slope we obtain a velocity of 368 m/sec while from the reflected shock the velocity is 363 m/sec. Notice that there is a slight bend in the curve at 0.5 cm, indicating that near the window the velocity may be different than the measured value. Unfortunately, it is difficult to obtain reproducible results in this region. We compare these results with theory in Chapter 7.

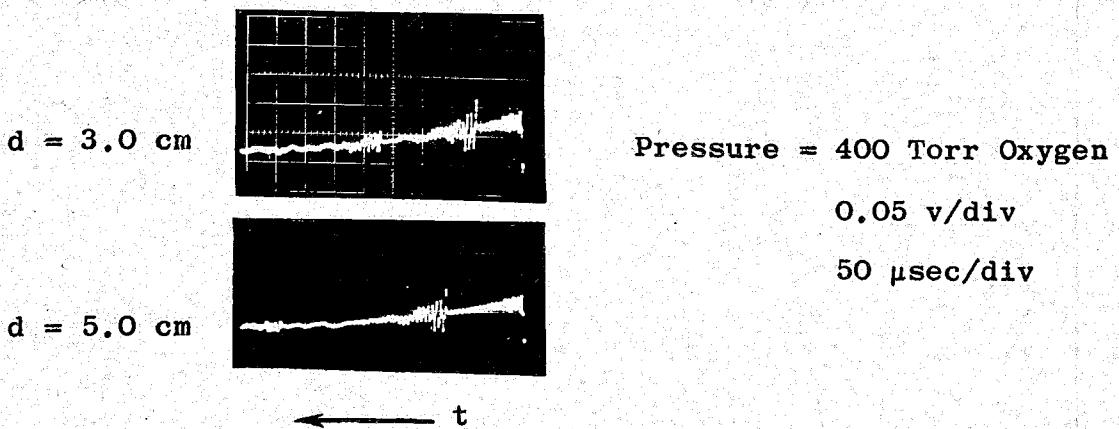


Fig. 6.5 Oscilloscope traces of piezoelectric probe.

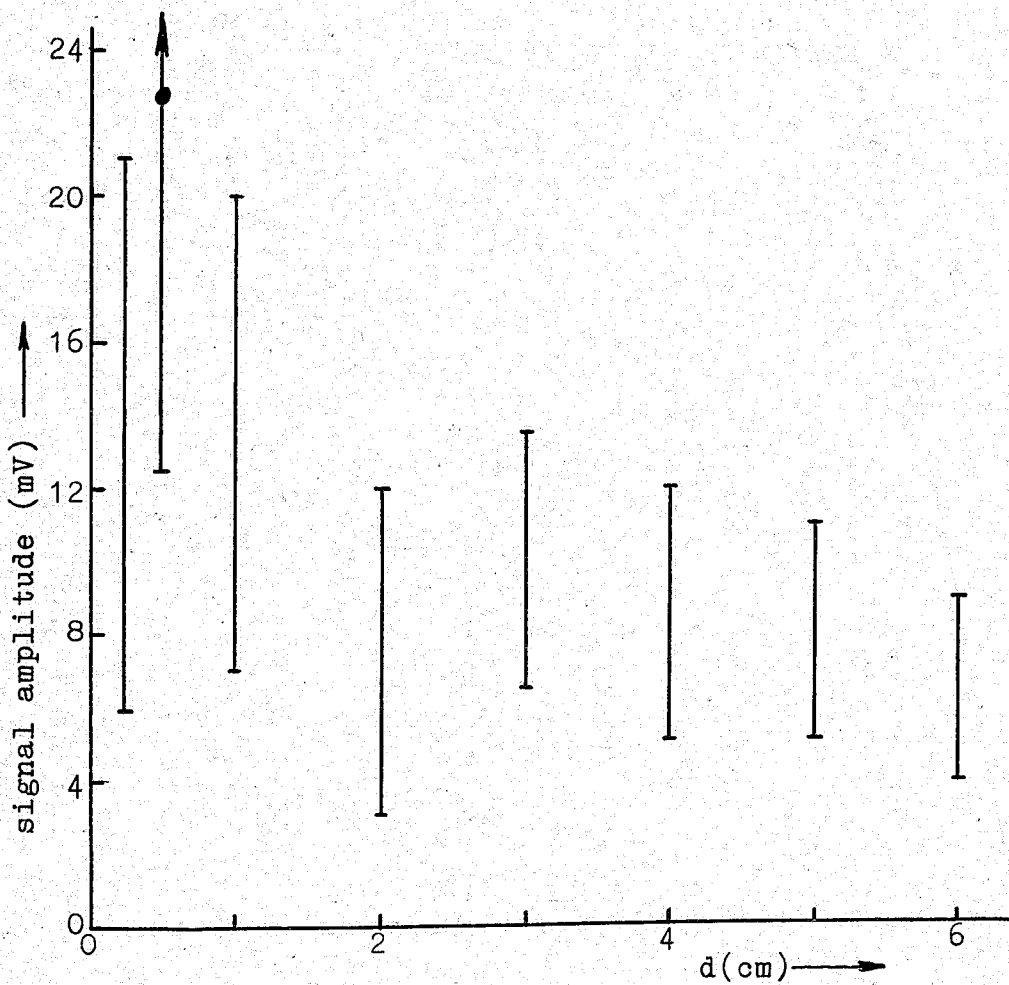


Fig. 6.6 Shock strength as function of d at 400 Torr oxygen

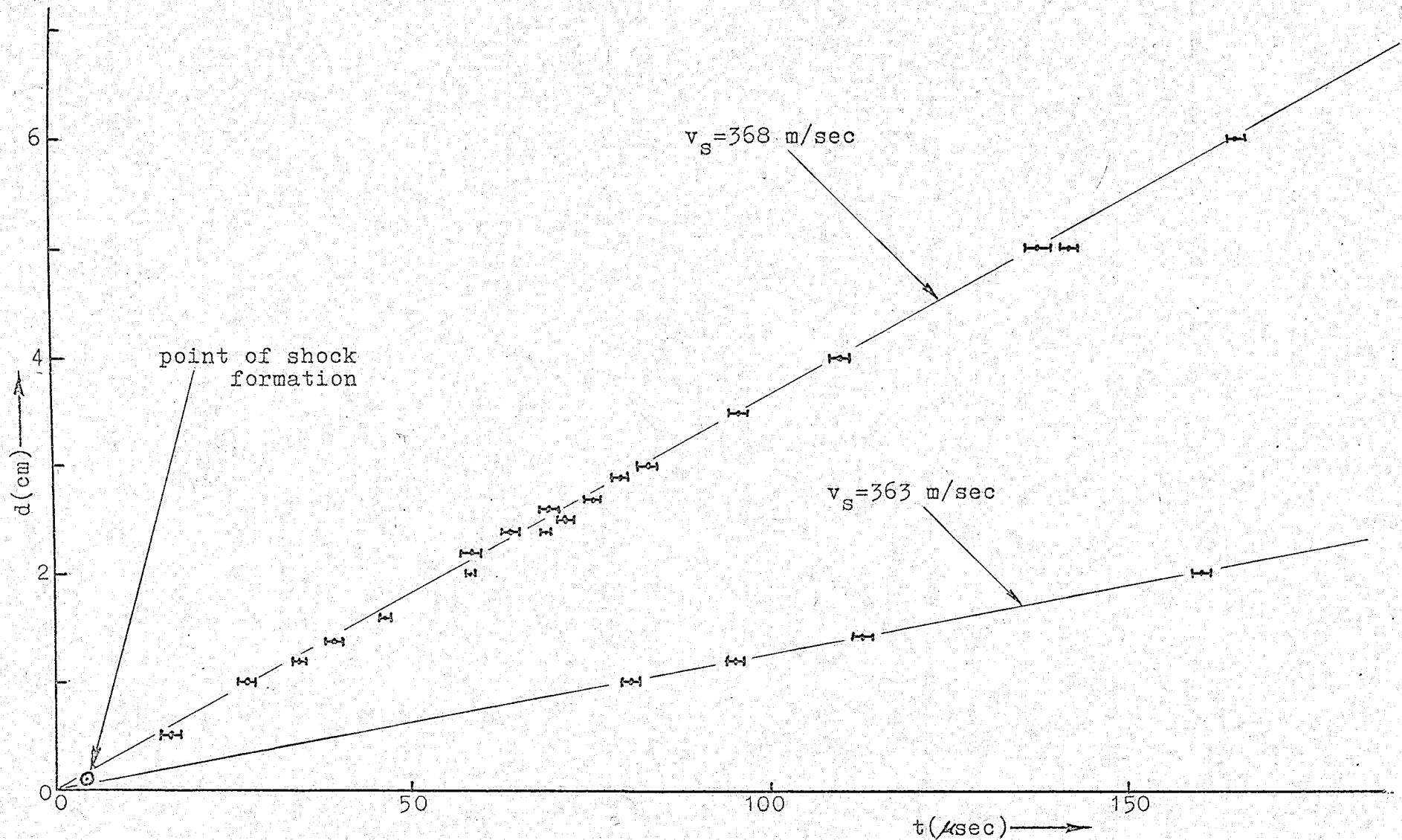


Fig.6.7 Velocity of shock at 400 Torr oxygen

6.3 Attempts to measure ionization in the test chamber

If one removes the window which was used in the two previous experiments then it is possible for ionizing radiation to enter the test chamber. Indeed large signals of the order of 100 volts were measured by means of electrodes inserted into the test chamber. However, these signals did not seem to be correlated with the light pulse in any way, seeming to start at or just after breakdown of the Bogen source whereas the light pulse is delayed 2 or 3 μ sec. Also, the signals depended upon the grounding of the dump chamber and polarity of the test chamber. Further, work along these lines was abandoned.

We also observed the photoeffect from metal surfaces due to radiation in the range of 1200 to 2000 \AA . With the intense Bogen light source it seems to be easy to produce a cold electron plasma, ideally suited for the measurements of electron-neutral collision cross sections. However, no systematic investigations were carried out.

CHAPTER 7

UNSTEADY ONE-DIMENSIONAL FLOW WITH ENERGY INPUT

In the theoretical section of this thesis we considered only the steady state cases in which the radiation front was fully developed and the incident radiation was constant as a function of time. In this chapter we will consider the development of radiation fronts with the incident radiation varying with time in an arbitrary manner. In particular, we will set up the theory to calculate the development of the shock fronts in oxygen which were observed experimentally in Chapter 6.

The boundary conditions again are a tube bounded at one end by a window. The motion of the gas may be described as unsteady one-dimensional flow with energy input. If the energy input as a function of time and position along the tube is known, the evolution of the flow along the tube may be calculated by the method of characteristics or by the method of finite differences. The rate of energy input $q(x,t)$ may be calculated quite generally according to the treatment outlined in Appendix C for the case of oxygen. However, we will base our calculations of this quantity on the simplified treatment outlined in section 4.3.2.

7.1 Method of characteristics

A detailed explanation of the method of characteristics is given by Shapiro (1954), Chapters 23-25 and Oswatitsch (1957), Chapter 3. Hoskin (1964) describes a method of calculation at fixed time intervals which is particularly applicable to our case. In order to show the limitations of this method we will first give a brief explanation.

Consider the x - t plane shown in Fig. 7.1(a). Let us assume that

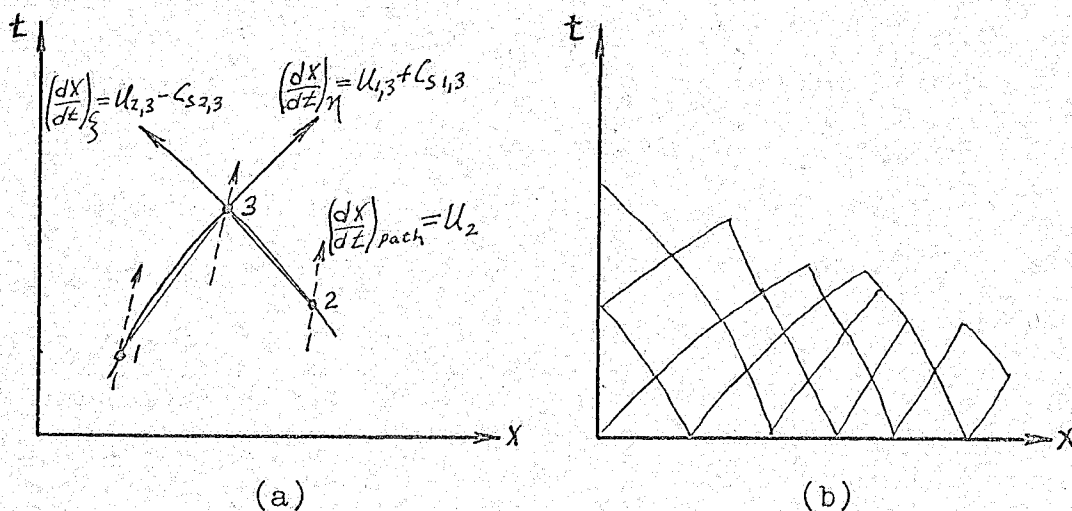


Fig. 7.1 Mach lines and path lines of characteristic net.

the complete state of the gas at points 1 and 2 is known. Any disturbance travelling to the right from point 1 will propagate with the speed $u_1 + c_{s1}$; any disturbance travelling to the left from point 2 will propagate with the speed $u_2 - c_{s2}$ (where u is the particle drift velocity and c_s is the speed of sound at the point in question). We refer to

the loci of right travelling waves as η characteristics or Mach lines and to the loci of left travelling waves as ξ characteristics or Mach lines. The loci of the individual particles are called path lines. The η and ξ characteristics intersect at some point 3.

The basis of the method of characteristics rests on the fact that along the Mach lines and path lines the thermodynamic quantities vary according to certain specified equations (see below) such that the state (and velocity) of the gas at point 3 may be calculated.*

The characteristics net is constructed as illustrated in Fig 5.1 (b). Using our case as an example we choose equally spaced points along the x-axis where the particle velocity is zero and the speed of sound is constant. We then find the intersection points of the η and ξ characteristics, and determine the thermodynamic quantities at these points. We then simply repeat the procedure to obtain the next set of points. As we feed in energy the characteristics net becomes distorted indicating the formation of compression and rarefaction waves. A shock forms at a point where two or more characteristics of the same family intersect.

The method of characteristics at fixed time intervals

* This is strictly true only if the η and ξ characteristics can be drawn as straight lines; however, we can satisfy this condition to as high an accuracy as we wish simply by decreasing the distance between points 1 and 2.

is similar in concept to the above explanation except that the points at which the state of the fluid is calculated are selected beforehand. For this purpose one usually selects a rectangular mesh in time-Lagrangian space coordinates and uses the required differential equations in Lagrangian form. The Mach lines are drawn backwards in time from the pre-selected point into the region where the state of the gas has already been calculated.

7.1.1 Physical characteristics in Eulerian and Lagrangian co-ordinates. -- In Eulerian co-ordinates the equations of the Mach lines is

$$\left(\frac{dx}{dt}\right)_{\eta, \xi} = u \pm c_s \quad 7.1$$

where the upper sign of \pm refers to the η characteristic and the lower sign refers to the ξ characteristic. The equation of the path lines is simply

$$\left(\frac{dx}{dt}\right)_{path} = u \quad 7.2$$

In Lagrangian co-ordinates z , eq'ns (7.1) and (7.2) may be written as

$$\left(\frac{dz}{dt}\right)_{\eta, \xi} = \pm \frac{\rho c_s}{\rho_0} \quad 7.3$$

and

$$\left(\frac{dz}{dt}\right)_{path} = 0 \quad 7.4$$

where ρ is the mass density, c_s is the speed of sound and ρ_0 is a constant reference density (e.g. the density at $t = 0$ when $\rho(x)$ is constant).

7.1.2 State characteristics. -- In Lagrangian co-ordinates the properties of the fluid along the path lines are described by the second law of thermodynamics

$$\left(\frac{\partial h}{\partial t}\right)_z - \frac{1}{\rho} \left(\frac{\partial p}{\partial t}\right)_z = q \quad 7.5$$

where h is the enthalpy per unit mass, ρ is the density and p is the pressure. q is the rate of energy input per unit mass as given in eq'n (4.19').

In Lagrangian co-ordinates the equations of momentum and mass may be written as (Hoskin (1964))

$$\frac{\partial u}{\partial t} + \frac{1}{\rho_0} \frac{\partial p}{\partial z} = 0 \quad , \quad 7.6$$

and

$$\frac{1}{\rho} \frac{\partial \rho}{\partial t} + \frac{\rho}{\rho_0} \frac{\partial u}{\partial z} \quad , \quad 7.7$$

where ρ_0 is a reference density defined in eq'n (7.3). (We neglect thermal conductivity and viscosity as was done in Chapter 4.) If we multiply eq'n (7.7) by the speed of sound c_s and use the equation of state in the form of eq'n (2.12)

$$h = \left(\frac{\gamma}{\gamma-1}\right) \frac{p}{\rho} \quad , \quad 2.12$$

eq'n (7.7) may be written in the form

$$\frac{1}{\rho c_s} \frac{\partial p}{\partial t} + \frac{\rho c_s}{\rho_0} \frac{\partial u}{\partial z} = \frac{1}{\rho c_s} \left(\frac{\partial p}{\partial t} - c_s^2 \frac{\partial \rho}{\partial t} \right) \quad . \quad 7.9$$

Using the energy equation and the equation of state (eq'ns (7.5) and (2.12)) we may write the right hand side of eq'n (7.9) in terms of the rate of energy input q . Thus eq'n (7.9) becomes

$$\frac{1}{\rho c_s} \frac{\partial p}{\partial t} + \frac{\rho c_s}{\rho_0} \frac{\partial u}{\partial z} = \frac{1}{\rho c_s} \left[(g-1) \rho g + \frac{\rho}{g-1} \frac{\partial g}{\partial z} + \left(\frac{\partial p}{\rho} - c_s^2 \right) \frac{\partial p}{\partial z} \right].$$

7.10

We now add and subtract eq'n (7.6) from eq'n (7.10) to obtain two equations in characteristic form

$$\begin{aligned} \frac{1}{\rho c_s} \left(\frac{\partial p}{\partial t} + \frac{\rho c_s}{\rho_0} \frac{\partial p}{\partial z} \right) \pm \left(\frac{\partial u}{\partial t} \pm \frac{\rho c_s}{\rho_0} \frac{\partial p}{\partial z} \right) \\ = \frac{1}{\rho c_s} \left[(g-1) \rho g + \frac{\rho}{g-1} \frac{\partial g}{\partial z} + \left(\frac{\partial p}{\rho} - c_s^2 \right) \frac{\partial p}{\partial z} \right]. \end{aligned}$$

Thus along the characteristics $(dz/dt)_{\eta, \xi} = \pm \rho c_s / \rho_0$ we have

$$\frac{1}{\rho c_s} \left(\frac{\partial p}{\partial t} \right)_{\eta, \xi} \pm \left(\frac{du}{dz} \right)_{\eta, \xi} = \frac{1}{\rho c_s} \left[(g-1) \rho g + \frac{\rho}{g-1} \left(\frac{\partial g}{\partial z} \right)_{\pm} + \left(\frac{\partial p}{\rho} - c_s^2 \right) \left(\frac{\partial p}{\partial z} \right)_{\pm} \right]. \quad 7.11$$

We emphasize that the differentials on the left hand side are evaluated along the Mach lines whereas the differentials on the right hand side of eq'n (7.11) are evaluated along the path lines.

There are two points in eq'n (7.11) which we would like to discuss. First, the term containing $(\partial g / \partial z)_{\pm}$ is usually small (though not necessarily negligible) compared to the term $(g-1) \rho g$. For calculations in this thesis we will neglect this term.* Secondly, the speed of sound c_s was introduced ad hoc and has not yet been defined. The problem here is that for a system of particles not in thermodynamic equilibrium the speed of sound depends on the frequency of the sound wave (see Zel'dovich and Raizer (1966), chapter VIII). (We should point out that we are really interested in the velocity of propagation of a disturbance

* see addendum Appendix D, page 138

at some point in the radiation front which we assume to be equal to the speed of sound at that point rather than in the speed of sound itself.) Classically the speed of sound is defined as the rate of change of pressure with respect to density at constant entropy (see eq'n (2.7))

$$c_s^2 = \left(\frac{\partial P}{\partial \rho} \right)_s = \frac{\gamma'' P}{\rho} ,$$

where γ'' is the isentropic exponent. We pointed out in Chapter 2 that replacing γ'' with the effective adiabatic exponent g may not be a very good approximation.

For non-equilibrium situations the validity of such an approximation is still more questionable. Nevertheless, for calculations in this thesis we will assume $c_s^2 = \frac{2}{g\rho} P$ such that the term containing $(\partial \rho / \partial t)_z$ in eq'n (7.11) is zero. With these two approximations we obtain a simplified form of eq'n (7.11)

$$\frac{1}{\rho c_s} \left(\frac{dP}{dt} \right)_{\eta, s} + \left(\frac{du}{dt} \right)_{\eta, s} = \frac{1}{\rho c_s} [(\gamma - 1) P g] \quad 7.11'$$

7.2 Method of finite differences in Lagrangian co-ordinate

If we use a constant energy input then the method of characteristics will determine the evolution of a radiation front and eventually the steady state structure as given in Chapter 3. However, once a strong shock has formed, a special procedure is required to calculate the thermodynamic quantities across it. If the structure of the shock

is of no importance it is more convenient to use the method of finite differences to calculate the flow.

A treatment of the method of finite differences in one space variable and no energy input is given by Richtmyer and Morton (1967), Chapter 12. Once their equations are modified to include the energy input, their treatment is directly applicable to our case for numerical solution on a computer.

One drawback of the method of finite differences is that it is incapable of handling shock discontinuities and sharp gradients in the thermodynamic quantities. The presence of such a discontinuity results in an oscillatory solution. To overcome this difficulty Richtmyer and Morton introduce an artificial viscosity which "smears out" the discontinuity over a finite distance and thus eliminates or reduces the oscillations in the solution.

This artificial viscosity Q_s is of the form

$$Q_s = \begin{cases} \frac{1}{2} a^2 (\delta u)^2 & \text{if } \delta u < 0 \\ 0 & \text{if } \delta u \geq 0 \end{cases} \quad 7.12$$

where "a" is a numerical constant ($a \geq 1$), the value of which one chooses at one's convenience and δu is the velocity change over the space interval δz between lattice points. This viscosity appears in the momentum and energy equations (see eq'ns (7.6) and (7.5)). One simply makes the substitution $p \rightarrow p + Q_s$.

Since we do not develop any new concepts in using this method we relegate the differential equations for this treatment to Appendix E.

7.3 Application of the two methods to dissociation fronts in oxygen

The equations given in the two sections above (and in Appendices D and E), together with eq'n (4.19') for the energy input and eq'n (4.19') for the energy input and eq'n (4.14) for the degree of dissociation, permit us to calculate the development and flow of any radiation front. One drawback is that in many cases the amount of computer time necessary for such calculations is prohibitively long (and expensive). Perhaps the procedures outlined in Appendices D and E could be modified to make more efficient use of computer time. (One possibility is to obtain a better first approximation in the iterative procedures by extrapolating the values of the variables from the previously calculated values.)

Nevertheless, these methods were used to help explain the results obtained previously. For the calculations we assumed that the incident radiation had a black body spectrum corresponding to a temperature of 6×10^4 °K.

7.3.1 Shock formation for time dependent radiation from Bogen source.-- The results of section 6.2 indicate that the shock front in oxygen at a high pressure forms more rapidly and nearer the LiF window than at low pressure. Also, near the LiF window the speed of the shocks may be lower at high pressures than at low pressures. It was not known if the signal measured by the piezo probe was due to a shock or a compression wave. In order to compare these results with the theory, the development of the shock was treated by the method of characteristics at fixed time intervals. (The method of finite differences cannot be used in this case since the artificial viscosity "smears out" any shocks which may form.)

The calculations were carried out for pressures of 1.0 atm and 0.1 atm. The various constants, the difference intervals and the computer programme which were used are given in Appendix D. (A computing time of 10 minutes was used.) Figs. 7.2 and 7.3 show computer plots of the various thermodynamic quantities as a function of dimensionless distance X at various times.

The pressure profiles are of special interest since this is the quantity which produces the signal measured in section 6.2. At 1.0 atm the pressure rises to a maximum of $p = 1.9 p_0$ within 3.0 μsec , then decreases as the pressure wave propagates away from the window. At 8 μsec the compression wave is at 0.295 cm and is travelling at a velocity of 460 m/sec. At 0.1 atm the maximum pressure is $p = 3.8 p_0$ within

3.2 μsec , is 3.3 p_0 at 8 μsec and 3.2 p_0 at 16 μsec . At 16 μsec the compression wave is at 0.85 cm and is travelling at a velocity of about 562 m/sec. In section 6.2 we obtained velocities of 364 m/sec at distances far from the LiF window. The fact that the calculated values are consistently higher than the measured value indicates that the photon flux ($F_0 = 1.16 \times 10^{22}$ ph/cm²sec) which we used in our calculations was too high. On the other hand the velocity measurements were taken relatively far from the LiF window whereas the calculations were carried out to distances relatively near the LiF window. Finally, it is possible that our programme gives a systematically high value for the velocity.

These pressure profiles indicate that the compression waves do not become shocks within the computing time. However, we should consider this statement with caution since it was not practicable to show that if sufficient time were allowed the compression waves do become shocks.

Fig.7.2 Computer profiles, 1.0 atm.

Method of characteristics at fixed time intervals.

Energy input from Bogen light source.

Peak photon flux, $F_0 = 1.16 \times 10^{22}$ ph/520 \AA cm^2sec .

Time, $t = (N-1)\Delta t$, with $\Delta t = 0.10$ μsec .

Distance from window, $x = 0.00249 X$ [cm] .

Curves plotted for $(N/10) = 1, 2, 3, \dots, 8$.

Fig.7.2 --continued

PRESSURE, $P=p/p_0$, with $p_0=1.0$ atm.

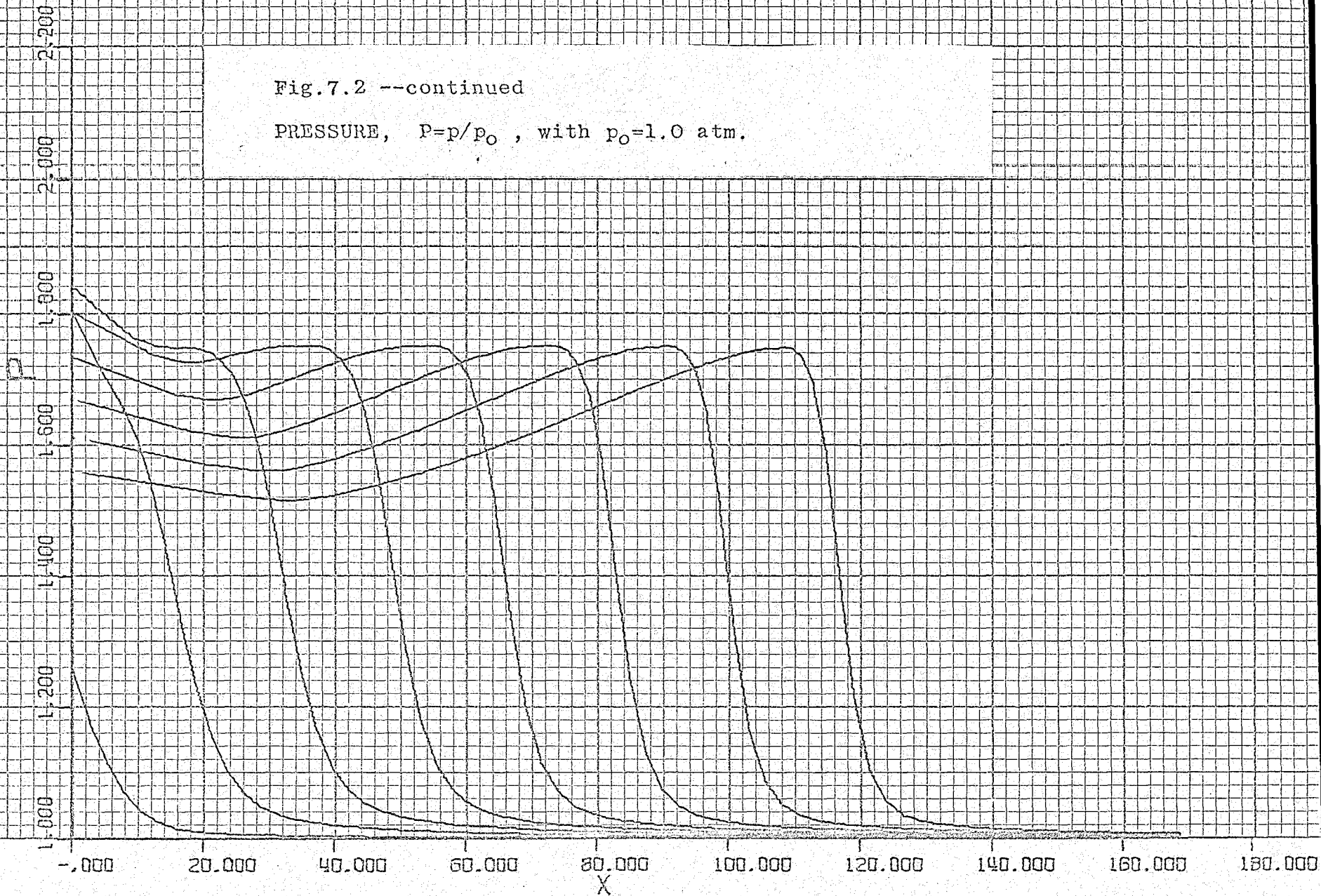


Fig.7.2 --continued

PARTICLE VELOCITY, $U=u/c_0$, with $c_0=330$ m/sec

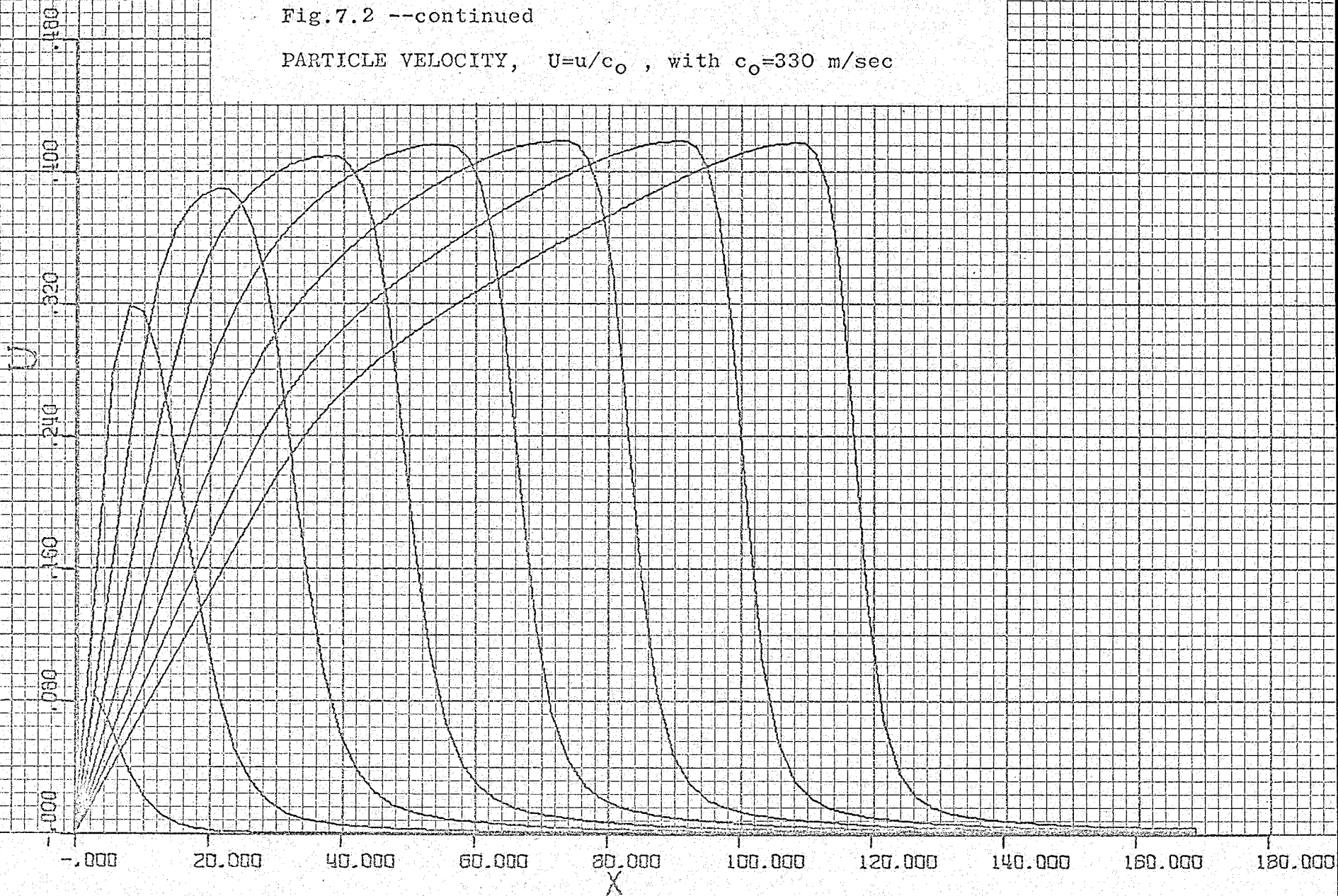


Fig.7.2 --continued

DENSITY, $R = \rho/\rho_0$, with $\rho_0 = 1.43 \times 10^{-3} \text{ gm/cm}^3$

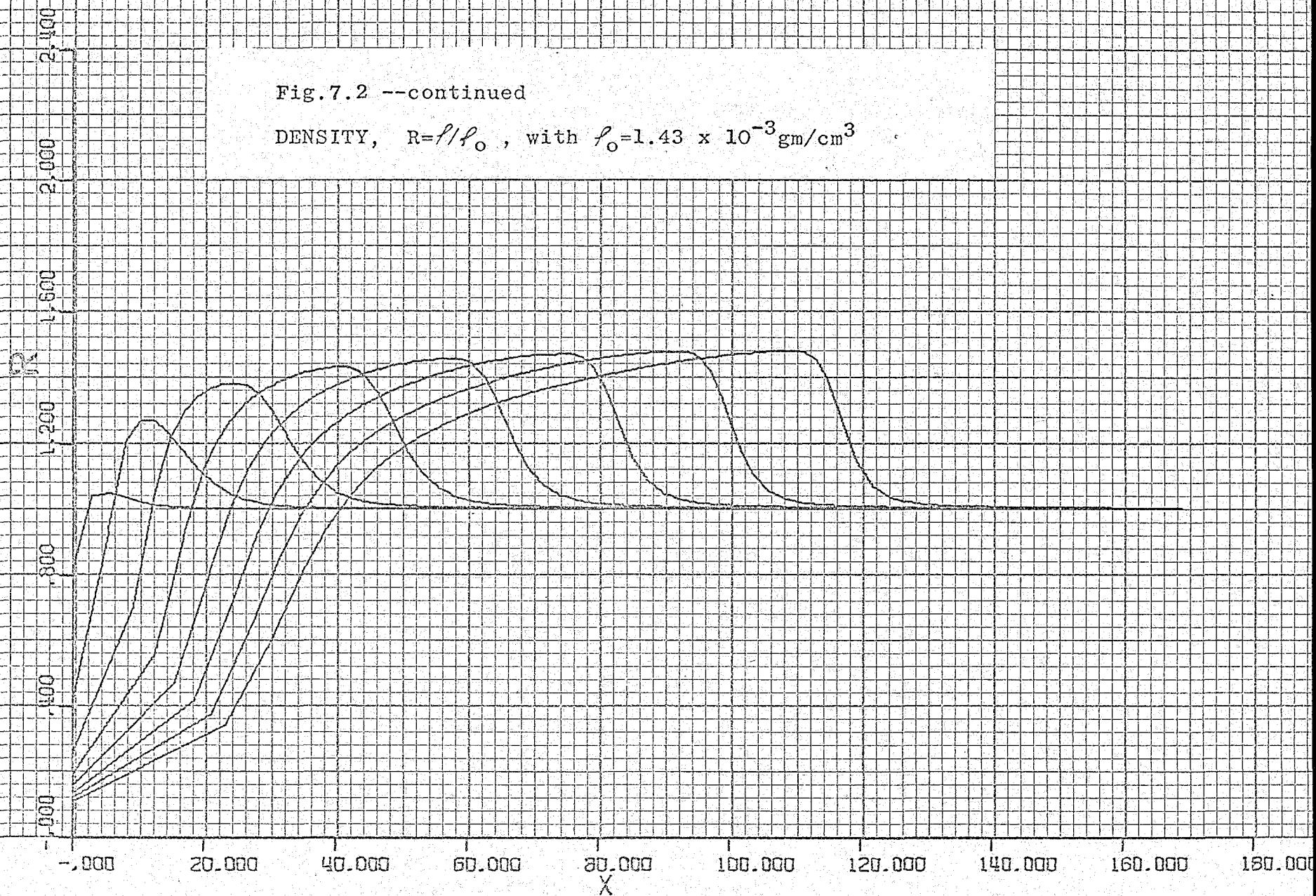


Fig.7.2 --continued

DEGREE OF DISSOCIATION, $Y=y$, with $0 \leq y \leq 1.0$

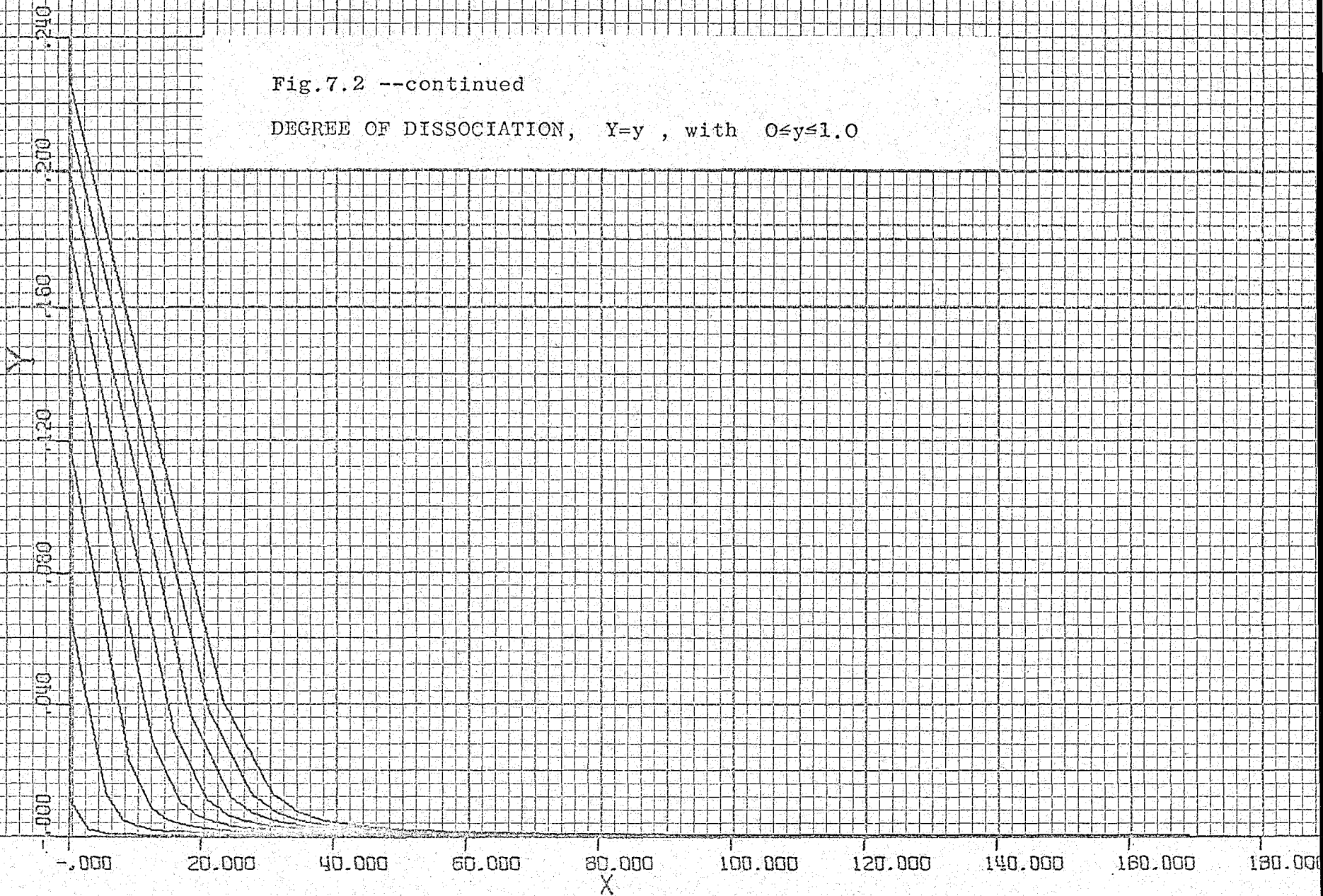


Fig.7.2 --continued

ENERGY INPUT, $Q=(M/\alpha\epsilon_0 f_0 c_0)q$, with $\alpha=14.94 \times 10^{-18} \text{cm}^2$,
 $\epsilon_0=1.94 \times 10^9 \text{ergs/gm}$, $M=53.3 \times 10^{-24} \text{gm}$

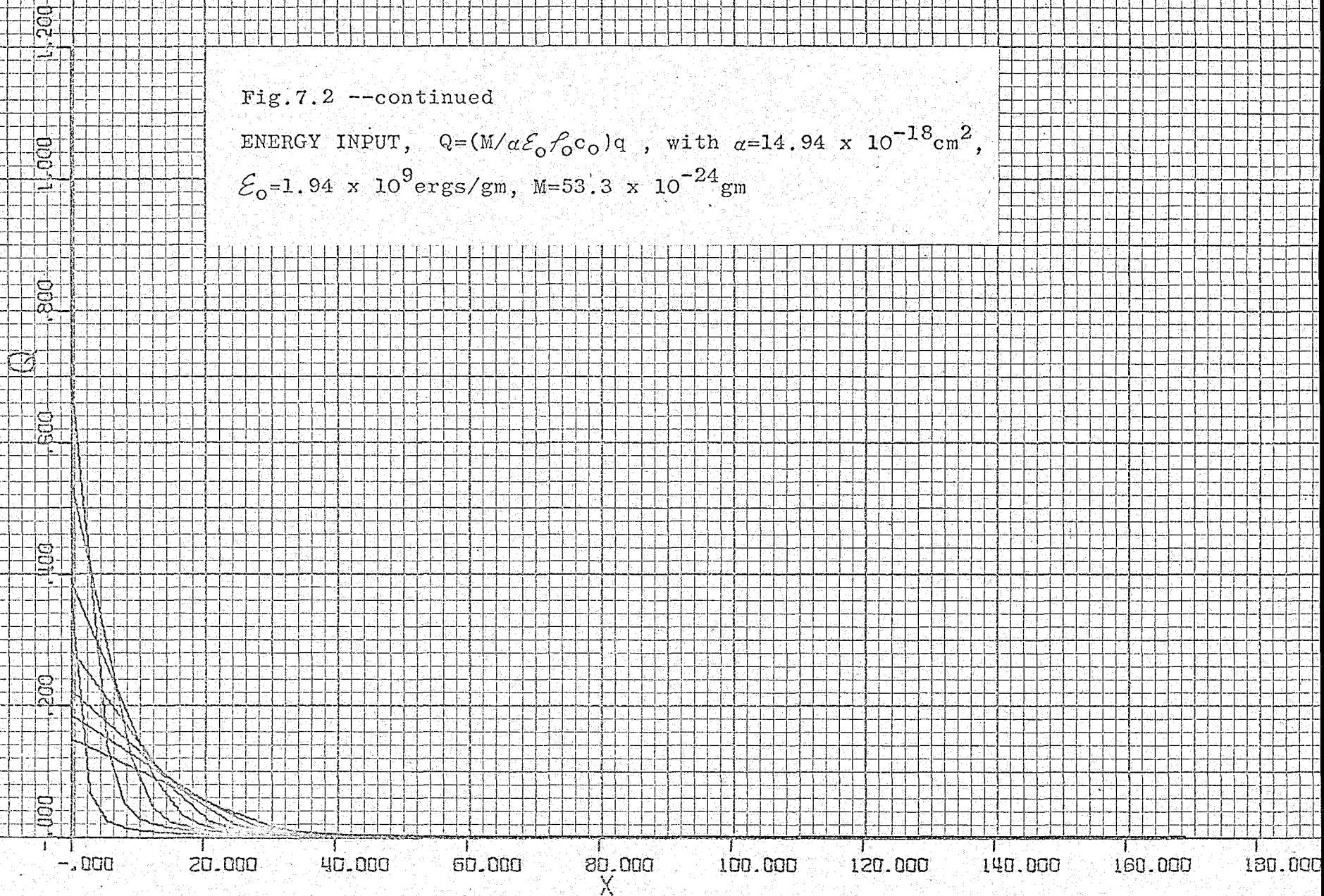
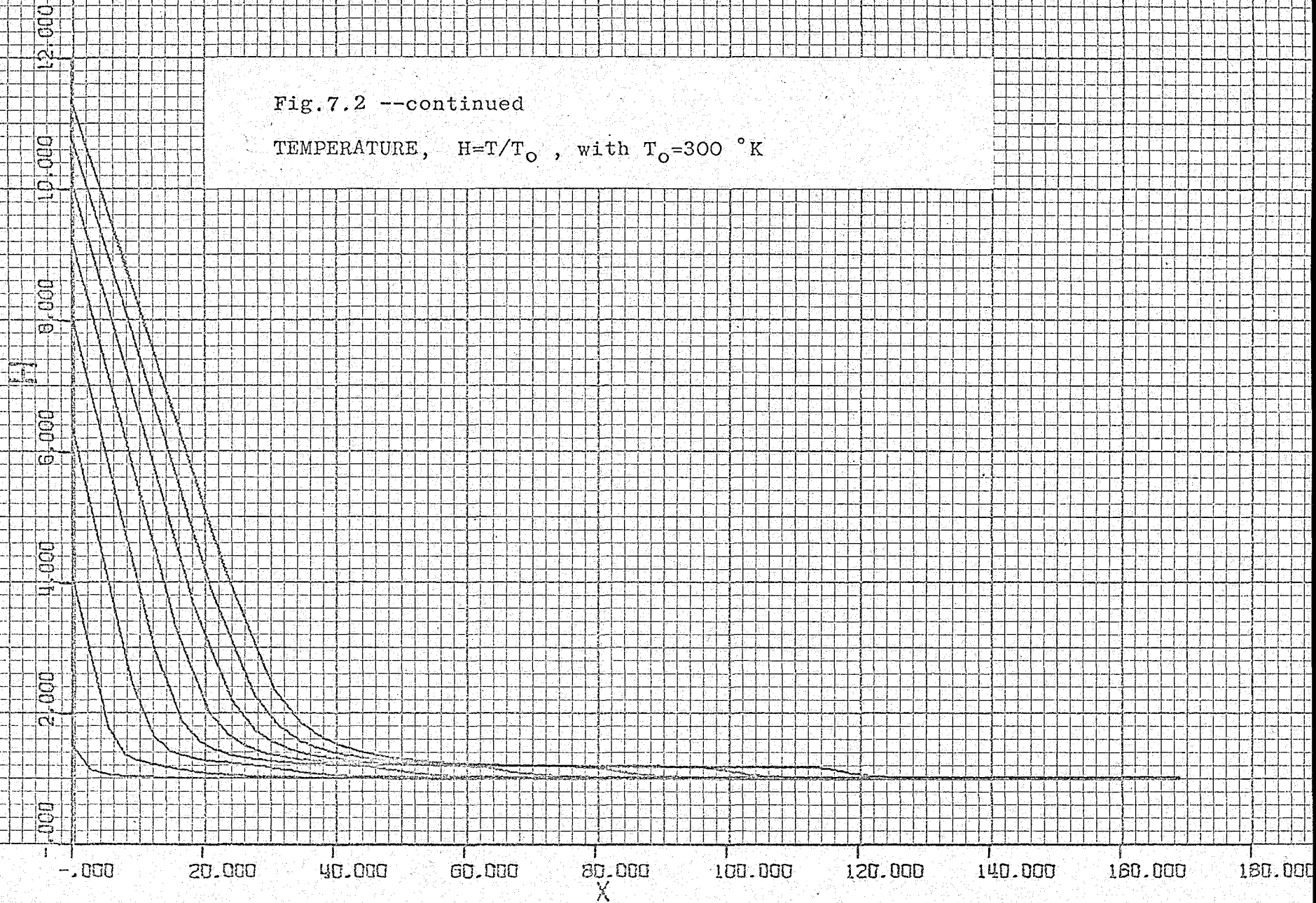


Fig.7.2 --continued

TEMPERATURE, $H=T/T_0$, with $T_0=300$ °K



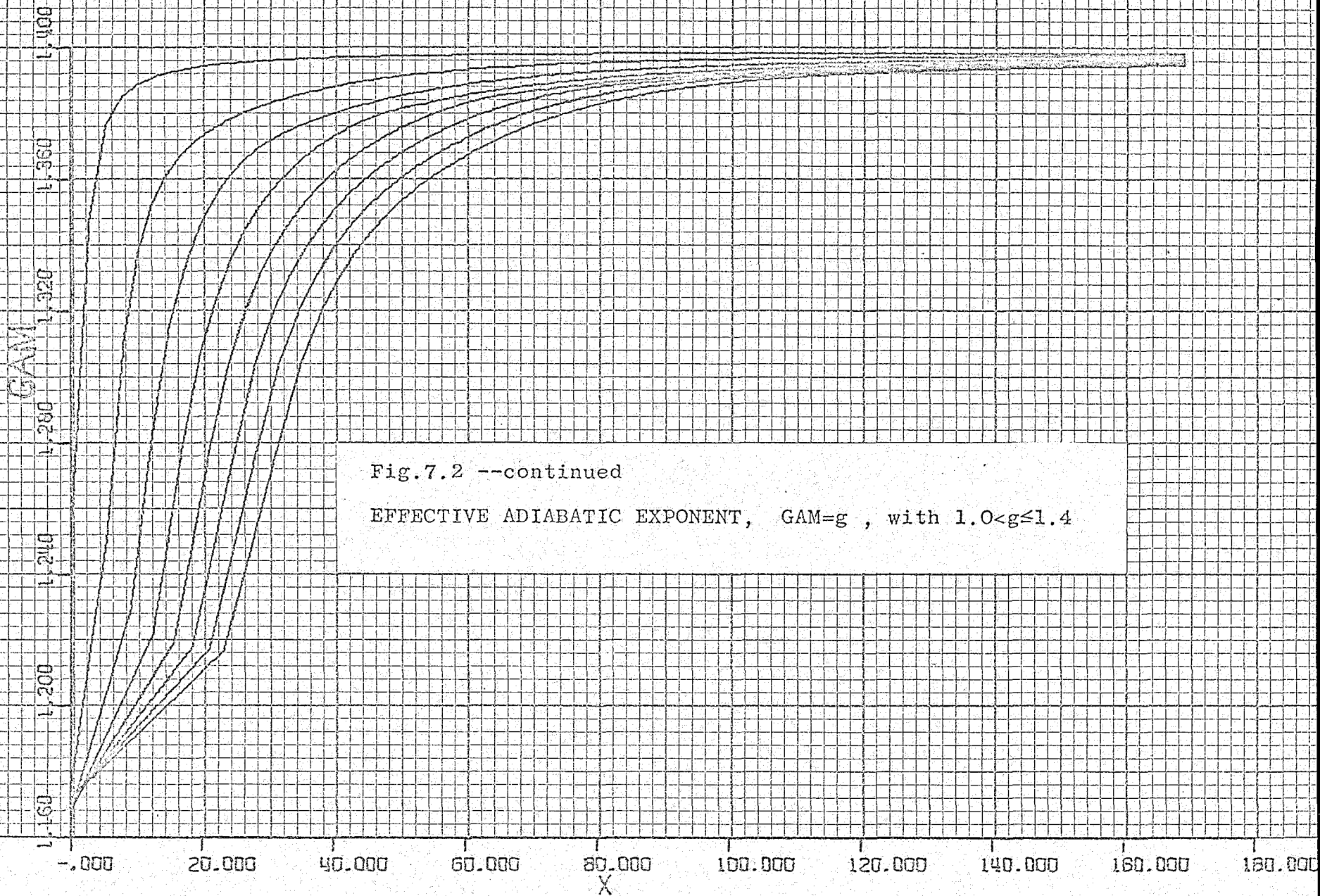


Fig.7.2 --continued
 EFFECTIVE ADIABATIC EXPONENT, $GAM=g$, with $1.0 < g \leq 1.4$

Fig.7.3 Computer profiles, 0.1 atm.

Method of characteristics at fixed time intervals.

Energy input from Bogen light source.

Peak photon flux, $F_0 = 1.16 \times 10^{22}$ ph/520Å cm²sec.

Time, $t = (N-1)\Delta t$, with $\Delta t = 0.20$ μsec.

Distance from window, $x = 0.0249 X$ [cm].

Curves plotted for $(N/10) = 1, 2, 3, \dots 8$.

Fig.7.3 --continued

PRESSURE, $P=p/p_0$, with $p_0=0.1$ atm.

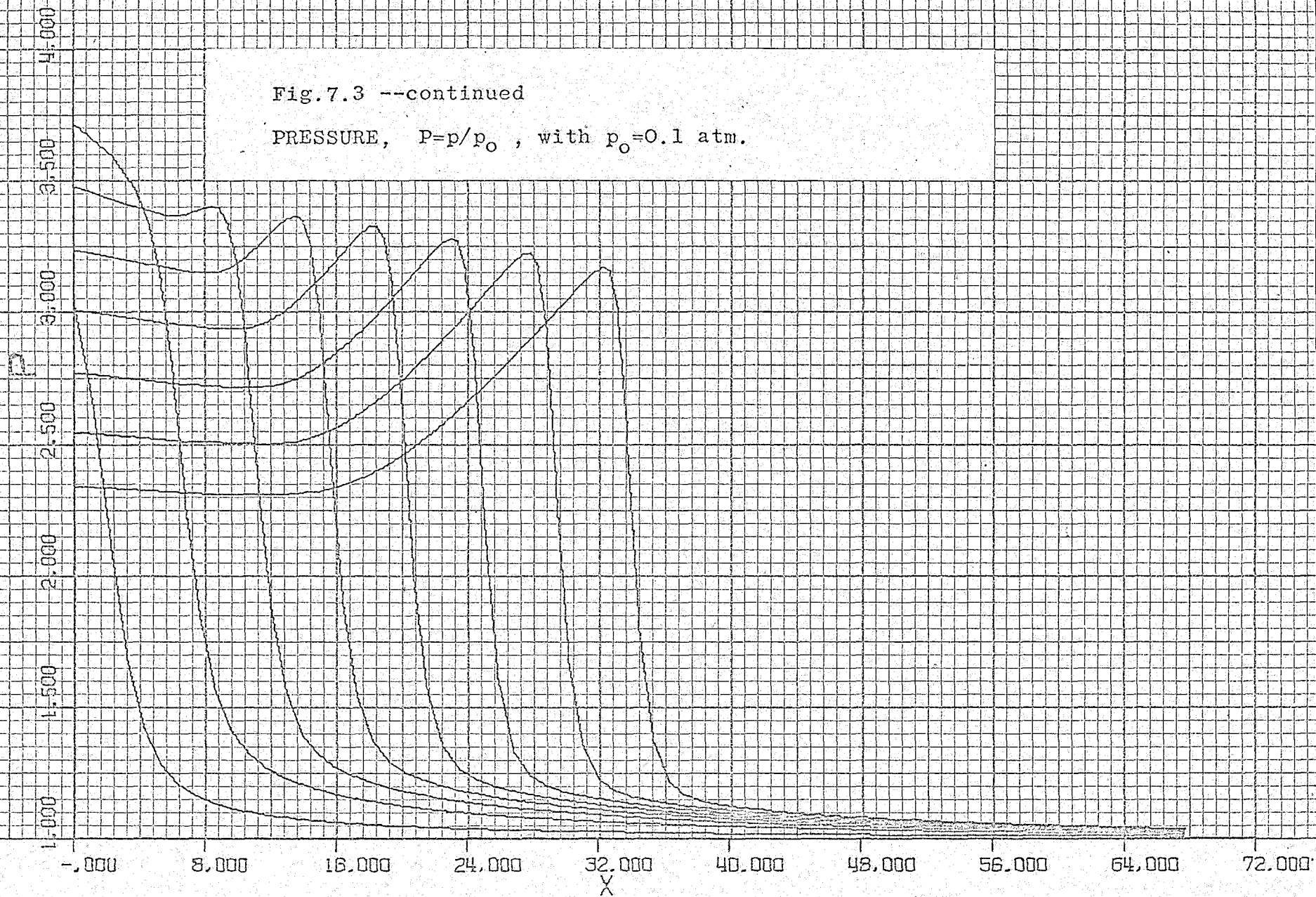


Fig.7.3 --continued

PARTICLE VELOCITY, $U=u/c_0$, with $c_0=330$ m/sec

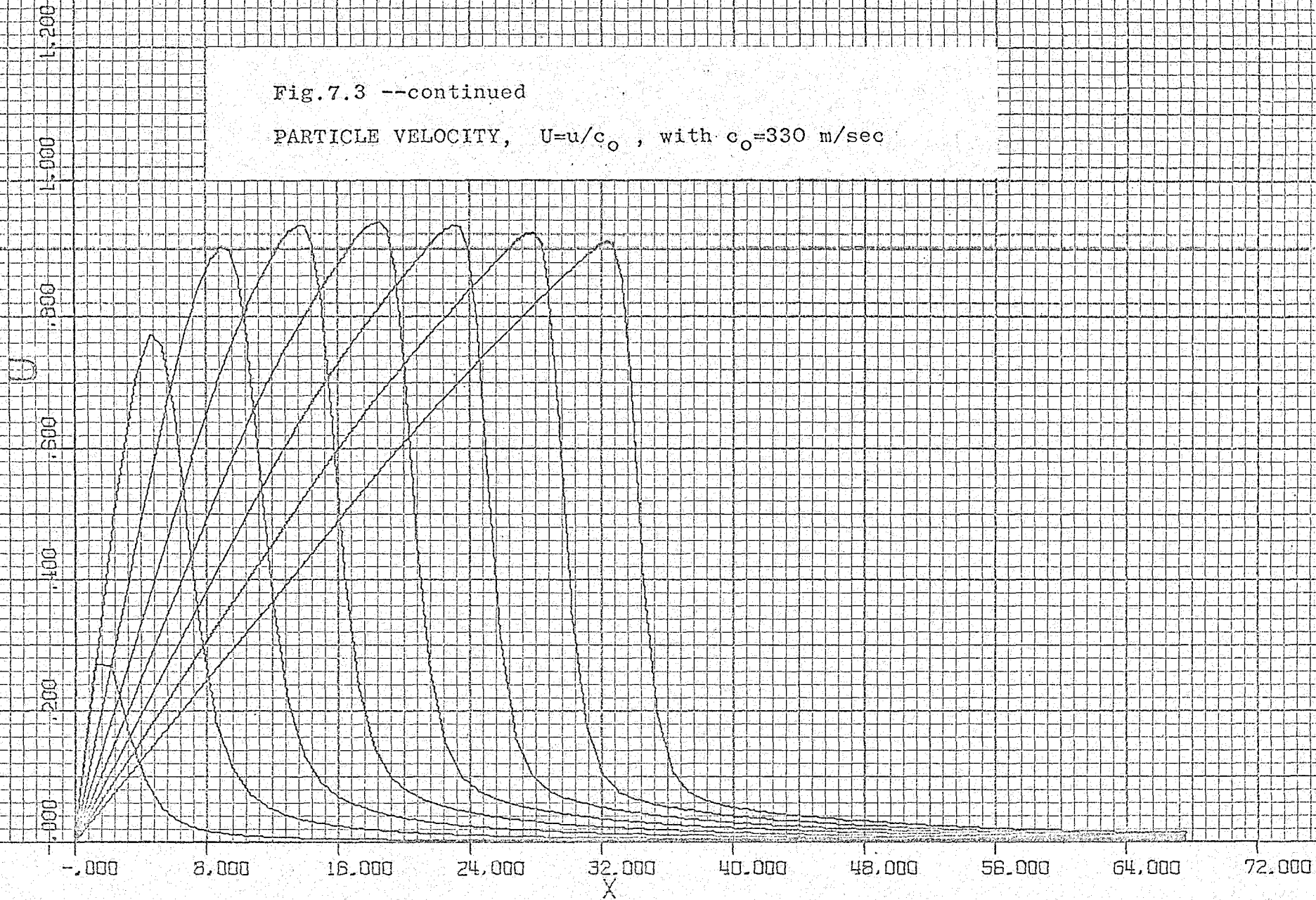


Fig.7.3 --continued

DENSITY, $R=f/f_0$, with $f_0=1.43 \times 10^{-4} \text{ gm/cm}^3$

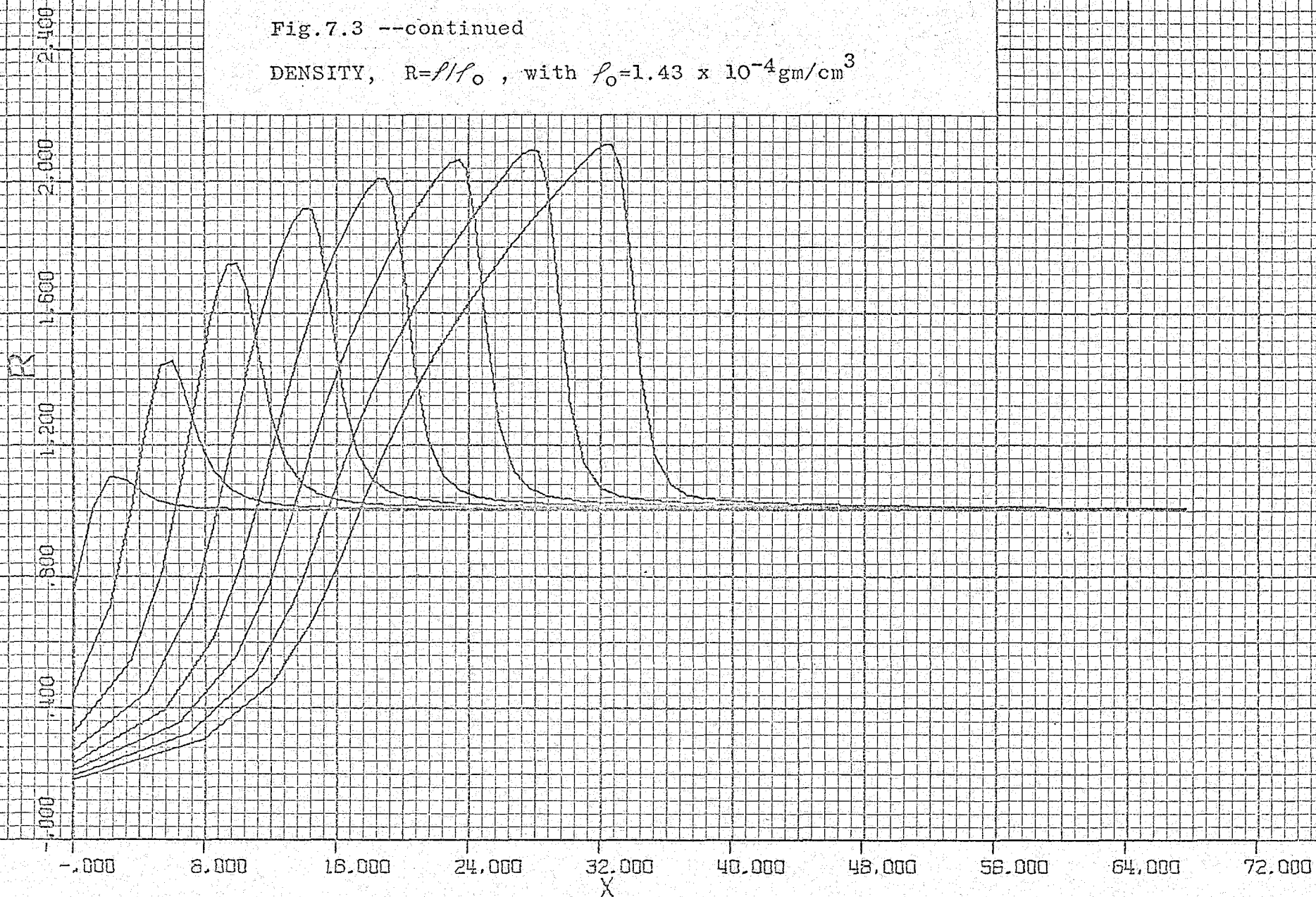


Fig.7.3 --continued

DEGREE OF DISSOCIATION, $Y=y$, with $0 \leq y \leq 1.0$

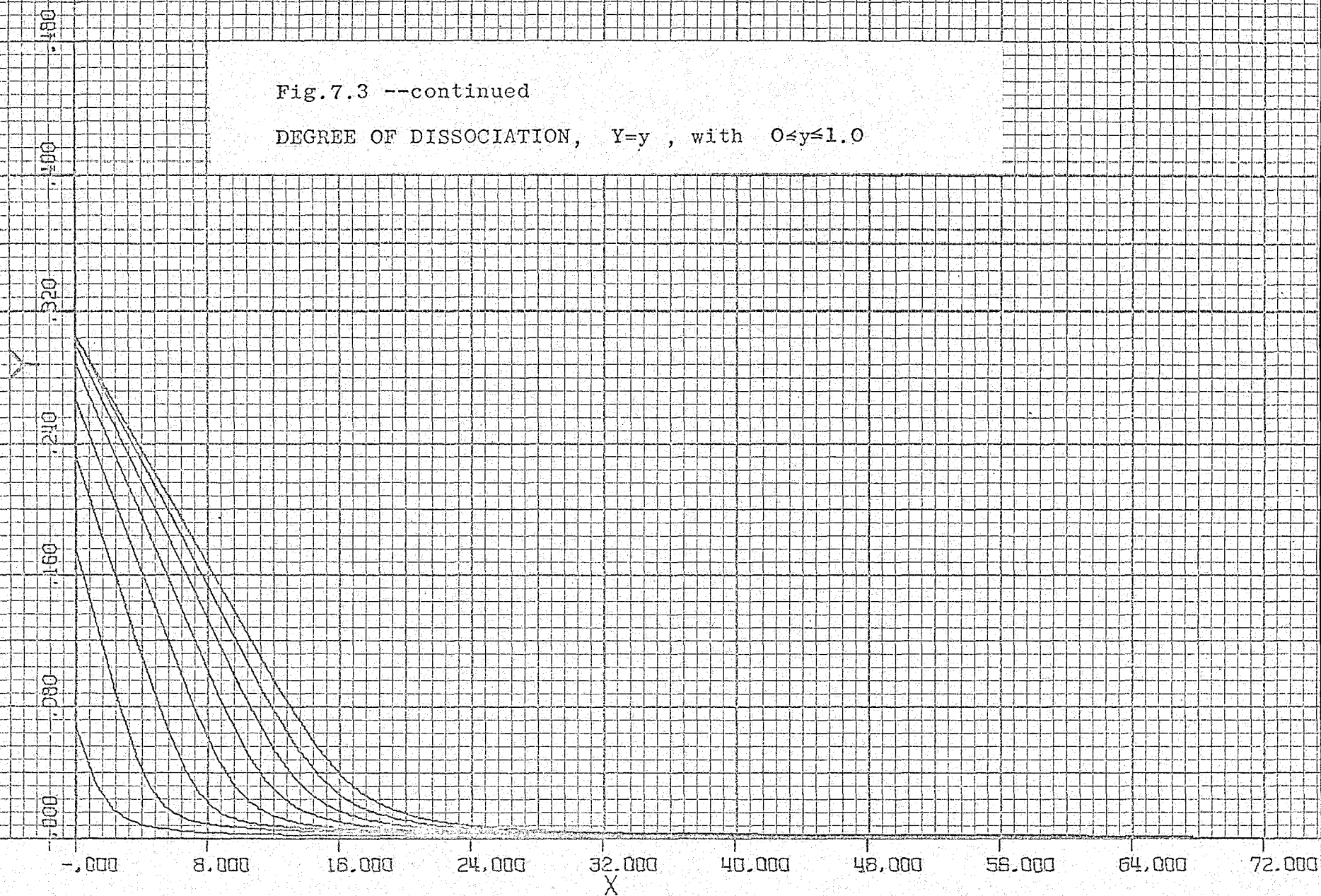


Fig.7.3 --continued

ENERGY INPUT, $Q=(M/\alpha \epsilon_0 f_0 c_0)q$, with $\alpha=14.94 \times 10^{-18} \text{cm}^2$,
 $\epsilon_0=1.94 \times 10^9 \text{ergs/gm}$, $M=53.3 \times 10^{-24} \text{gm}$

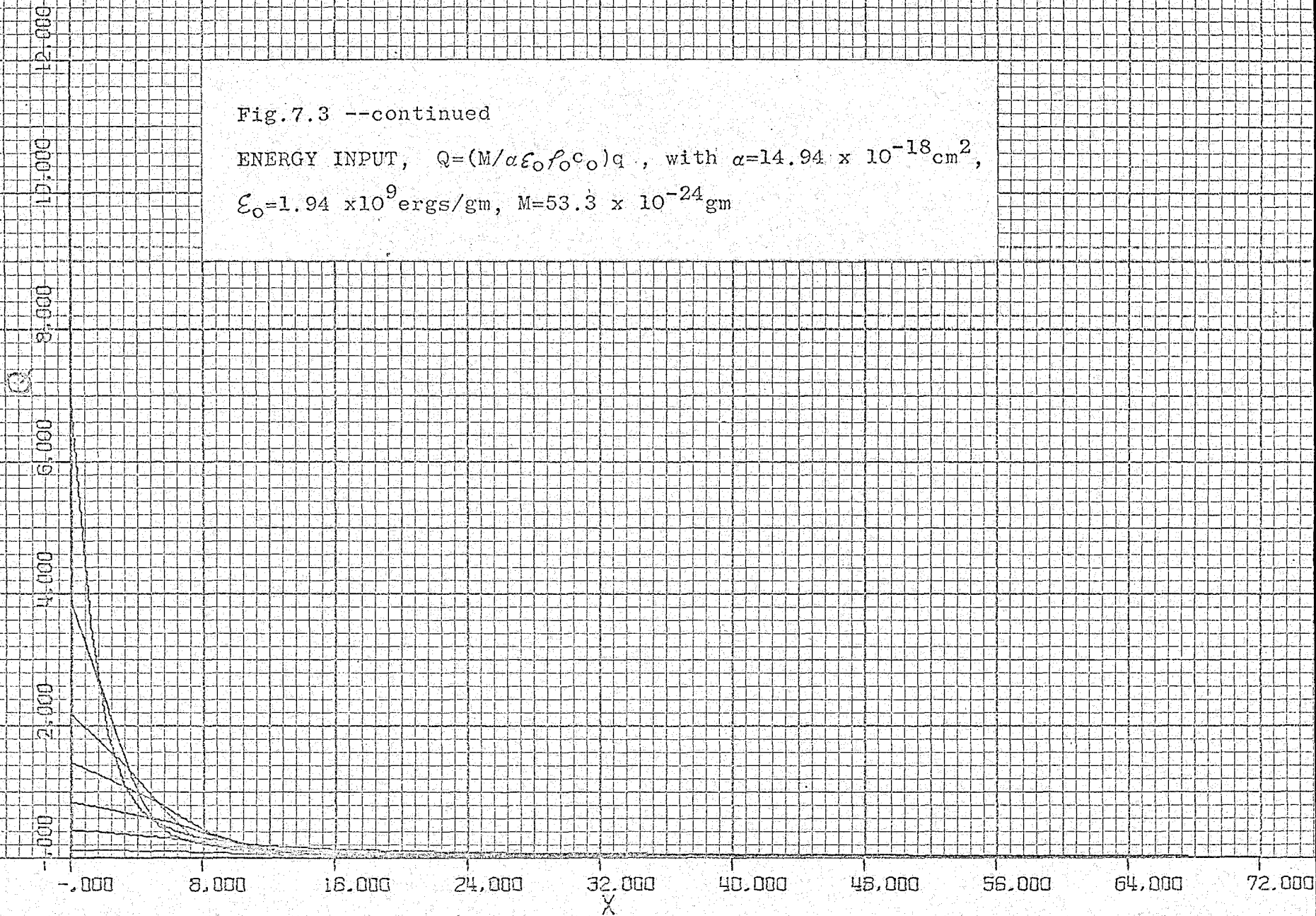
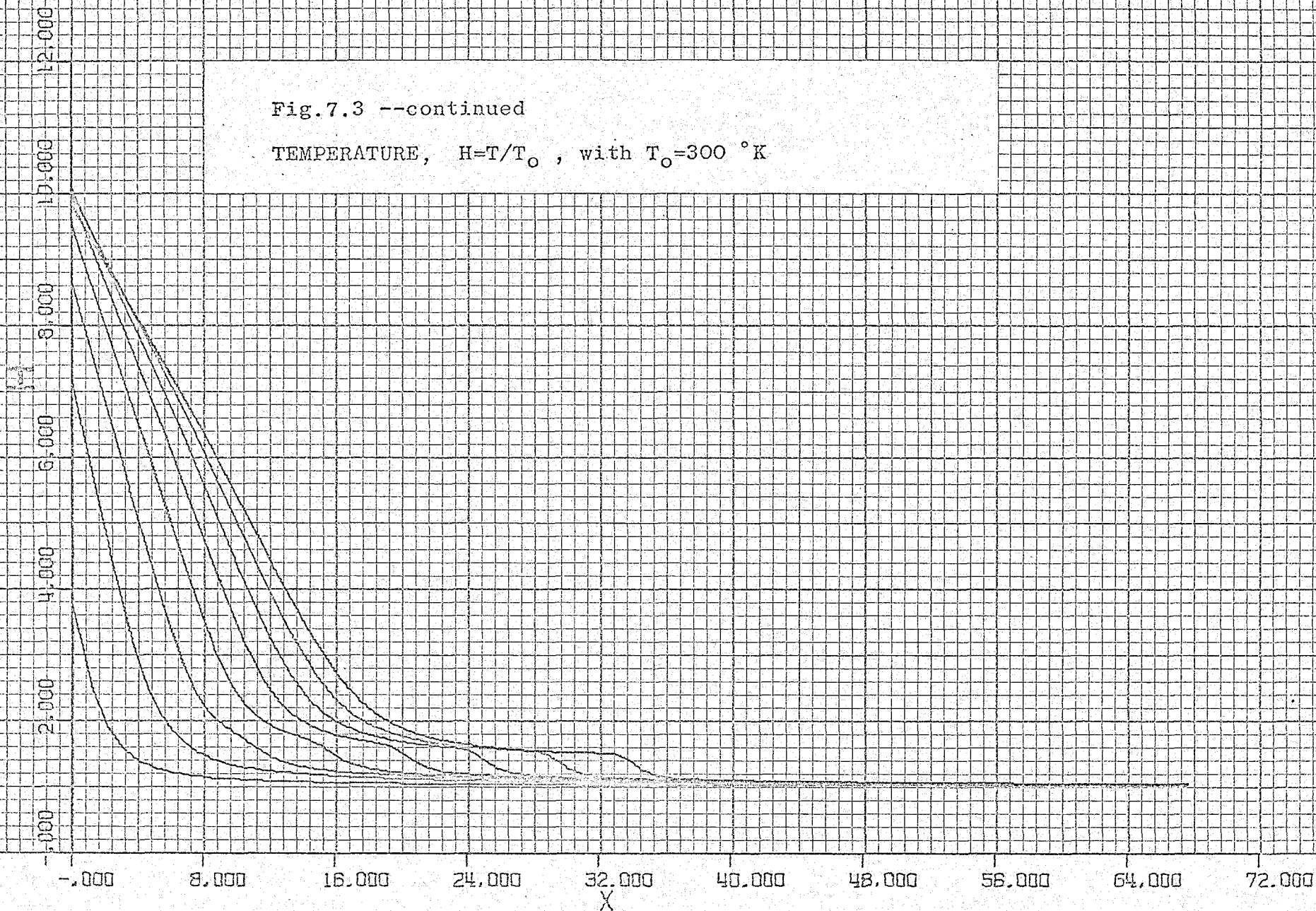


Fig.7.3 --continued

TEMPERATURE, $H=T/T_0$, with $T_0=300$ °K



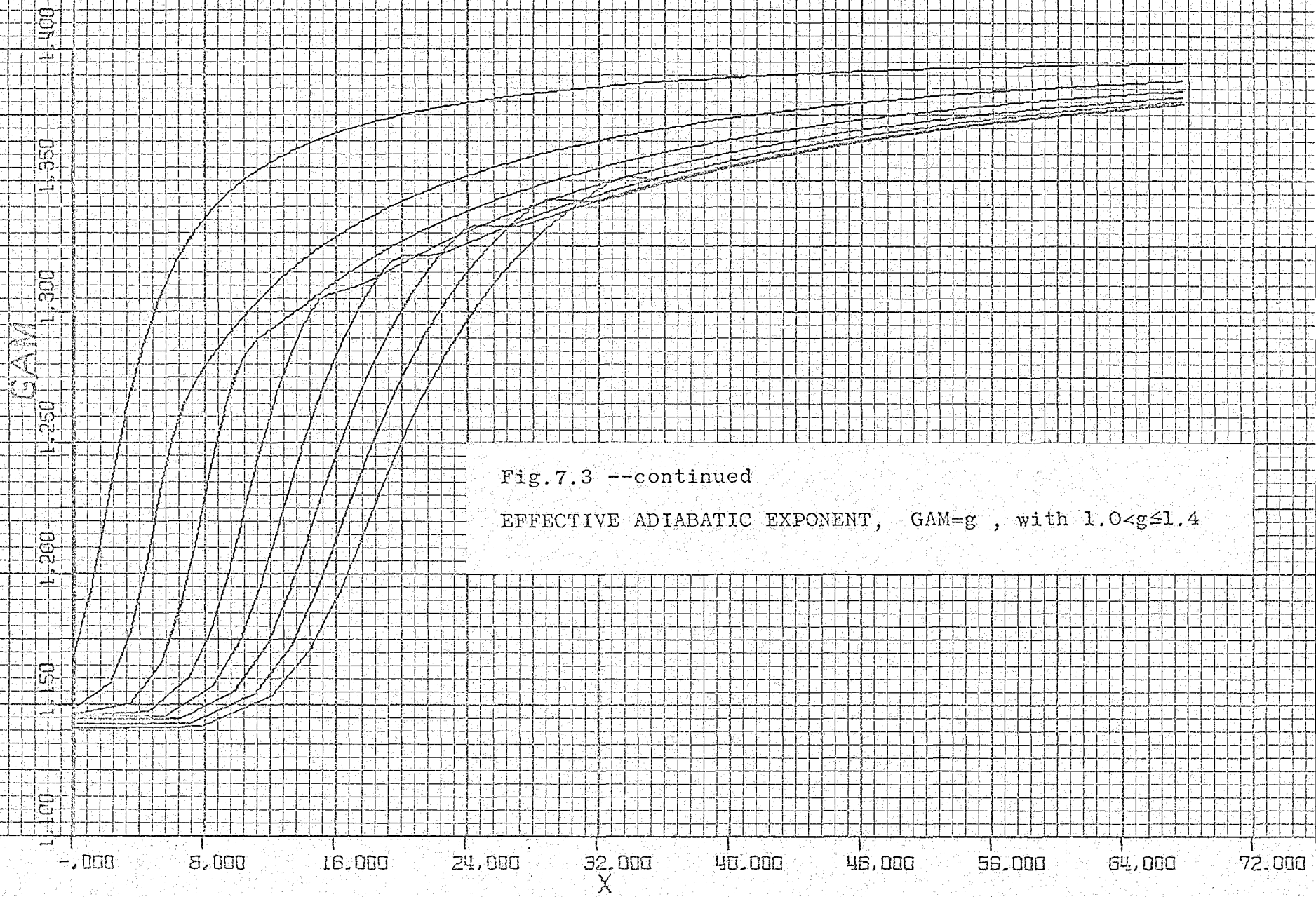


Fig.7.3 --continued
 EFFECTIVE ADIABATIC EXPONENT, $GAM=g$, with $1.0 < g \leq 1.4$

7.3.2 Structure of a steady dissociation front.---

The results of Chapter 3 indicate that a steady photon flux $F_0 = 4.72 \times 10^{22}$ ph/cm²sec (with an energy of 8.8 eV) is required to produce a weak D-type radiation front preceded by a Mach 3 shock at an initial pressure of 0.01 atm oxygen. We applied the method of finite differences to calculate the evolution of the flow for this case. The constants, difference intervals and the computer programme for these calculations are given in Appendix E.

Again it was impracticable to carry on with the calculations until steady state was reached. However, the plot of the pressure as a function of distance X, see Fig. 7.4, indicates that within 15 μ sec the pressure is 7.2 times the initial value. At this point the degree of dissociation at the window is only 36%, the temperature is 4000 °K and the compression ratio (final : initial density) is 0.39. The maximum particle velocity is $1.4 c_0 = 460$ m/sec. Although the radiation front is in the initial stages of development, it already exhibits some of the properties predicted in Chapter 3.

These results must be considered as preliminary since considerable difficulty was encountered in preventing the calculations from going into oscillations and as many as 15 iterations were necessary to obtain self-consistent values. In fact, such oscillations are already in evidence in the computer profiles shown in Fig. 7.4.

Fig.7.4 Computer profiles, 0.01 atm.

Method of finite differences, applied to conditions for a weak D-type radiation front preceded by a Mach 3 shock.

Photon flux, $F_0 = 4.72 \times 10^{22}$ ph/cm² sec.

Time, $t = N\Delta t$, with $\Delta t = 0.303 \mu\text{sec}$.

Distance from window, $x = 0.249 X$ [cm].

Curves plotted for $(N/10) = 1, 2, \dots, 5$.

Fig.7.4 --continued

PRESSURE, $P=p/p_0$, with $p_0=0.01$ atm.

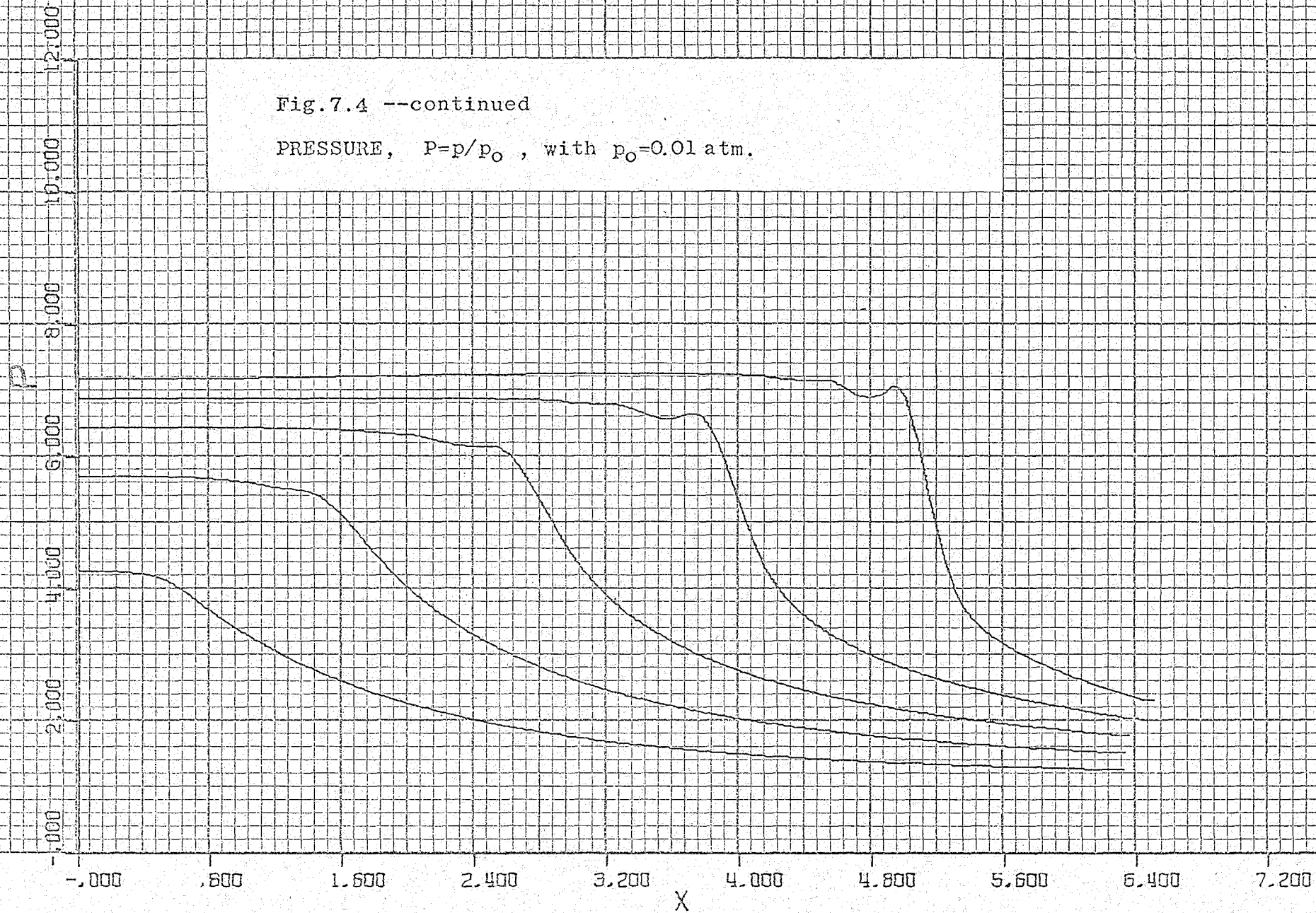


Fig.7.4 --continued

PARTICLE VELOCITY, $U=u/c_0$, with $c_0=330$ m/sec

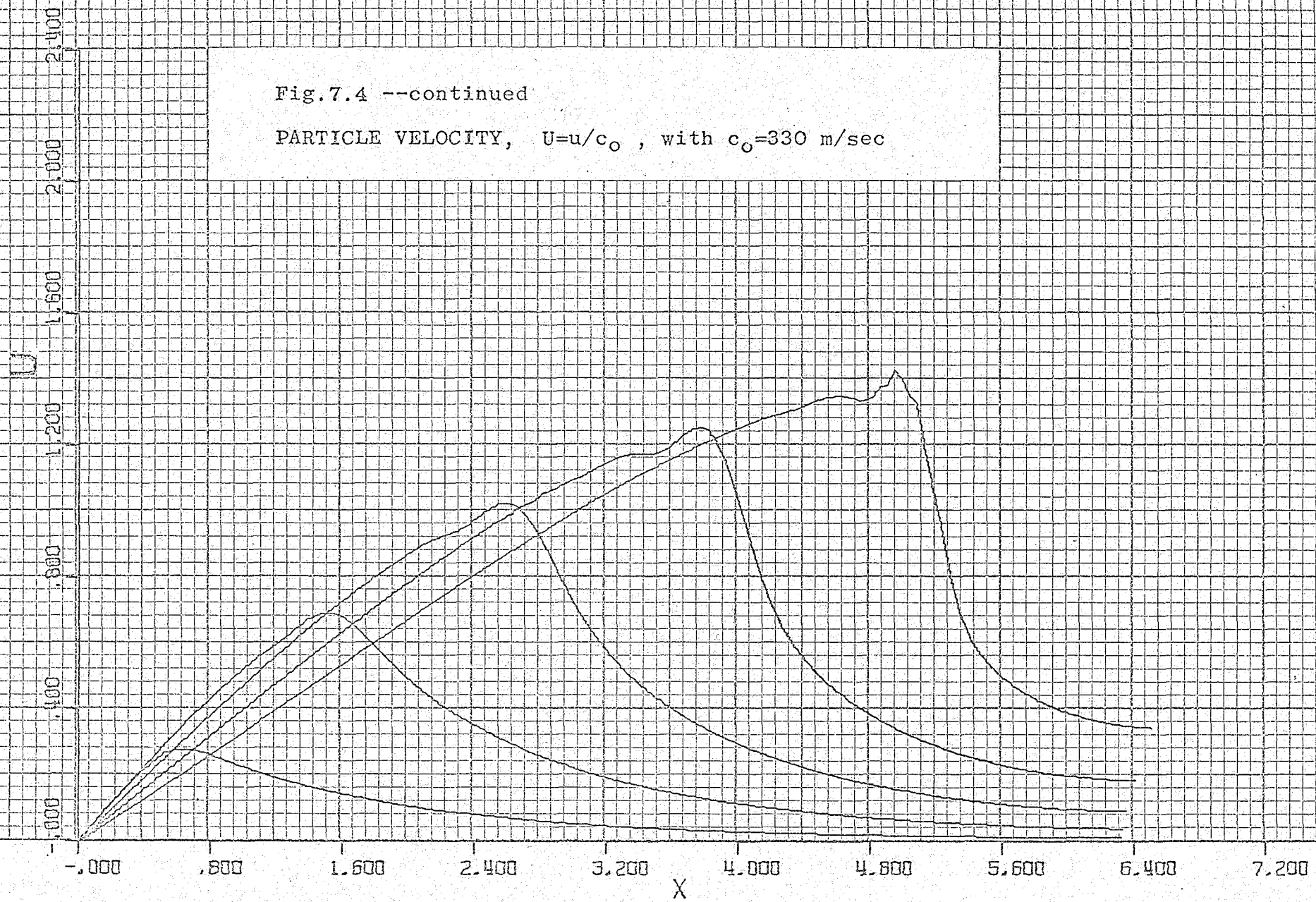


Fig.7.4 --continued

SPECIFIC VOLUME, $V = \rho_0 / \rho$, with $\rho_0 = 1.43 \times 10^{-5} \text{ gm/cm}^3$

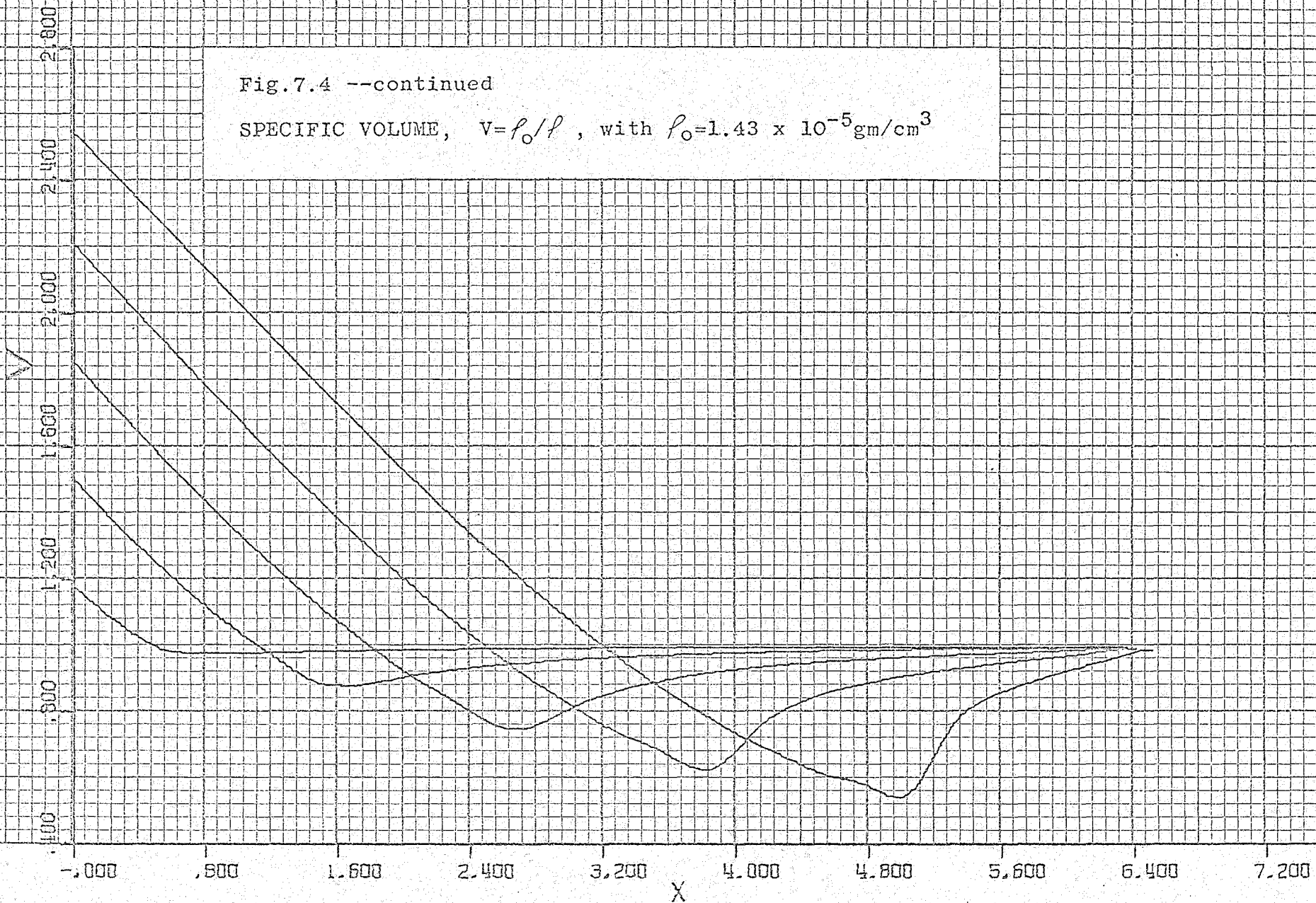


Fig.7.4 --continued

DEGREE OF DISSOCIATION, $Y=y$, with $0 \leq y \leq 1.0$

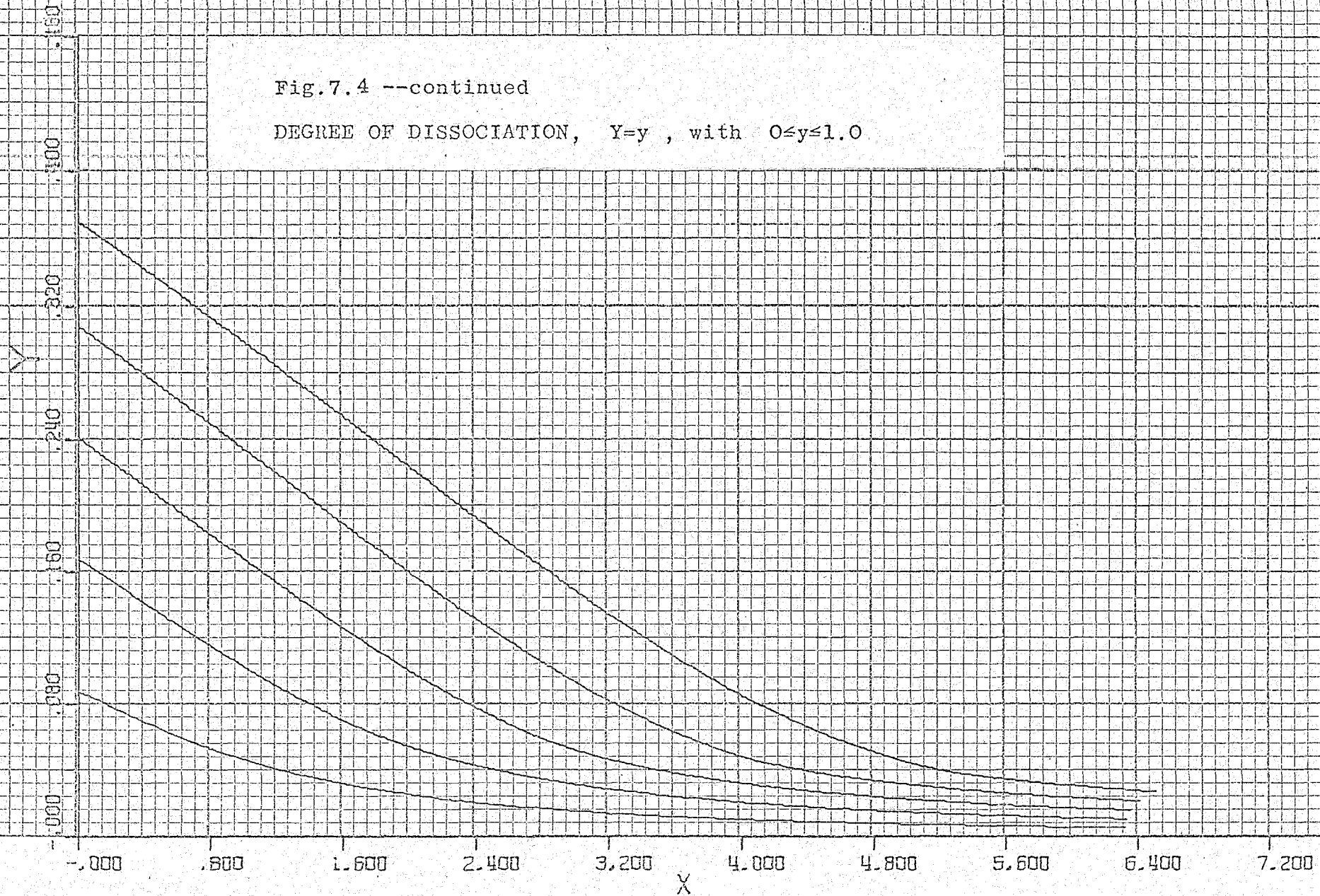


Fig.7.4 --continued

ENERGY INPUT, $Q=(M/\alpha \epsilon_0 f_0 c_0)q$, with $\alpha=14.94 \times 10^{-18} \text{cm}^2$,
 $\epsilon_0=1.94 \times 10^9 \text{ergs/gm}$, $M=53.3 \times 10^{-24} \text{gm}$

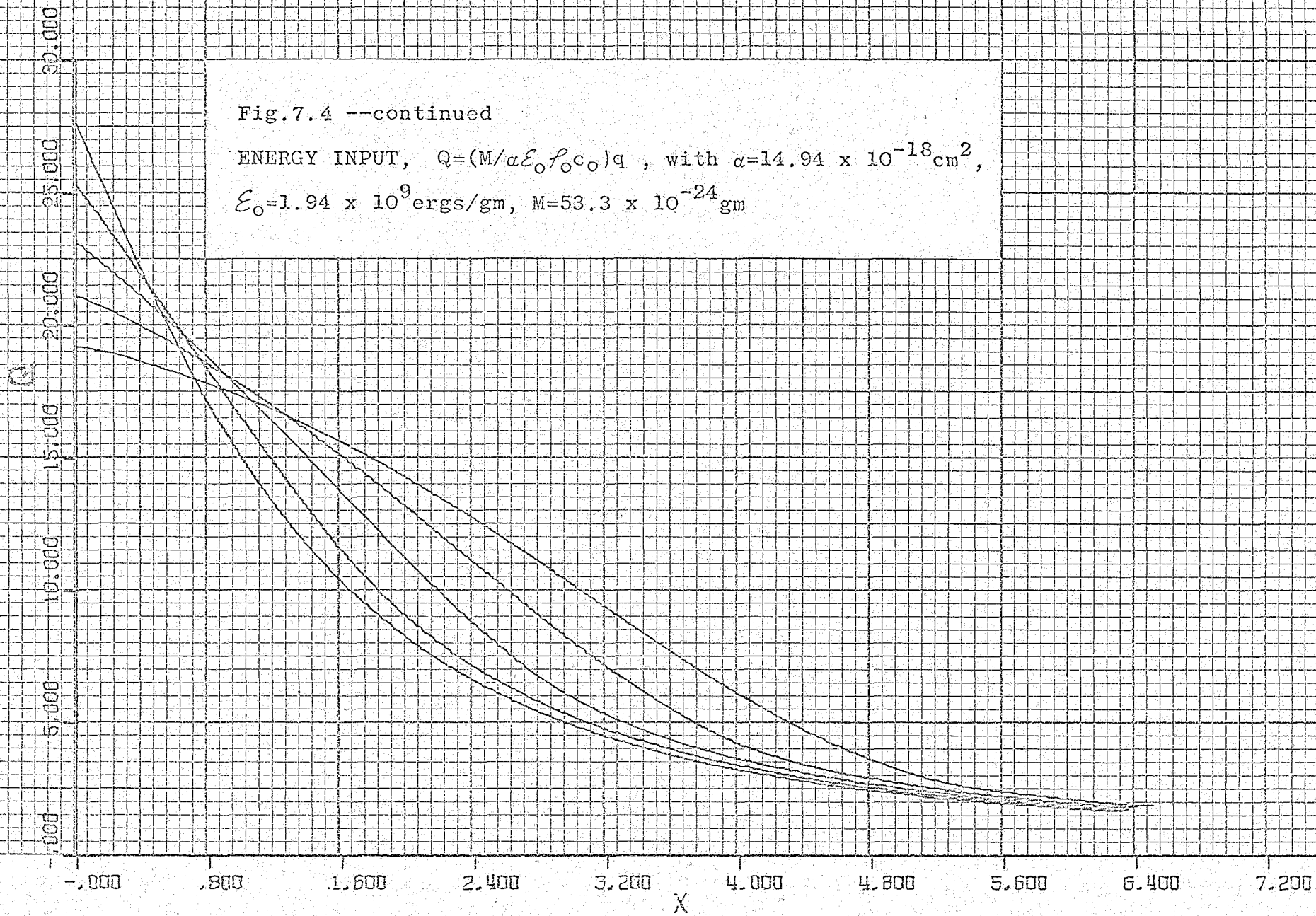
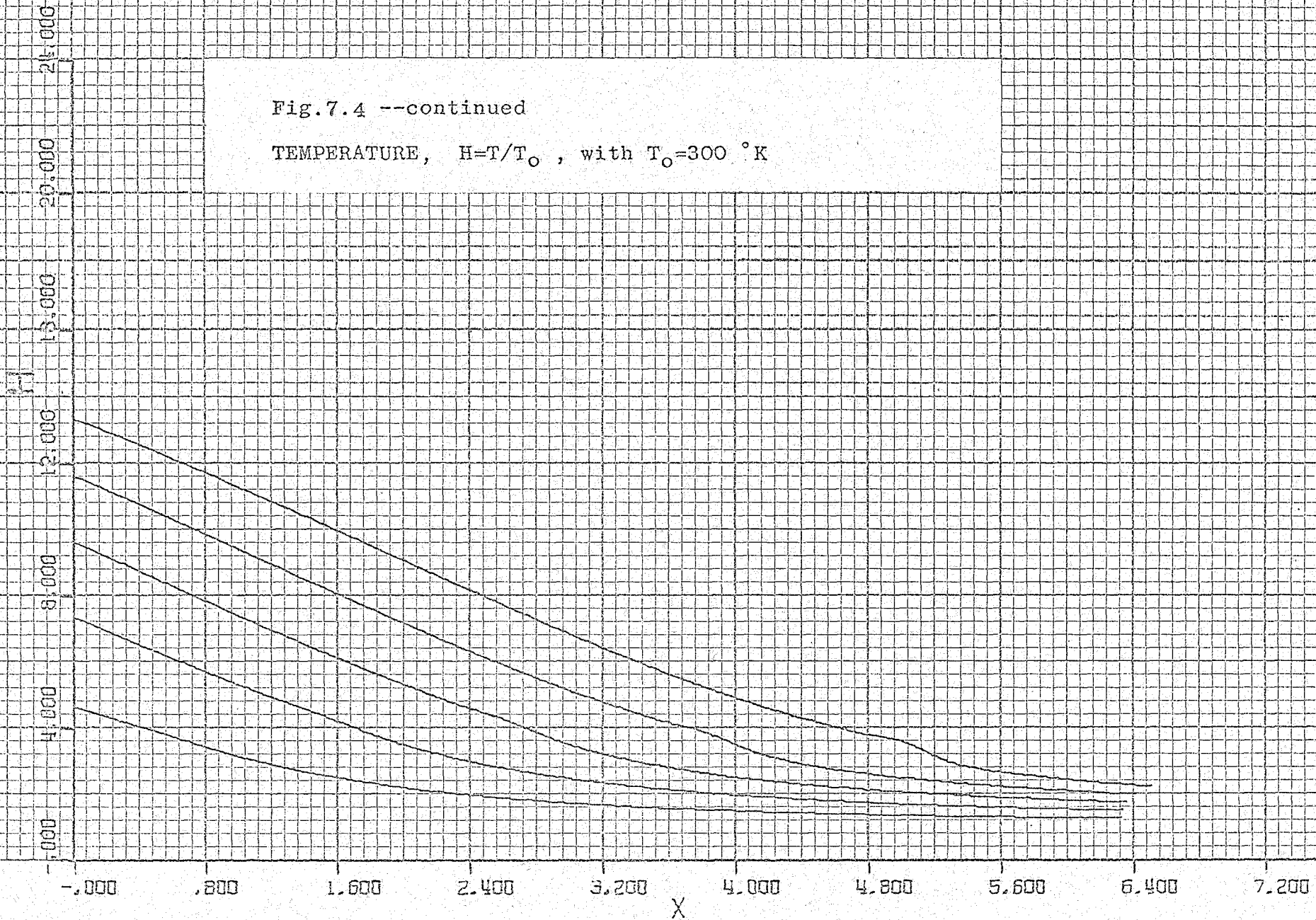


Fig.7.4 --continued

TEMPERATURE, $H=T/T_0$, with $T_0=300$ °K



CHAPTER 8

SUMMARY AND CONCLUSIONS

The object of this thesis was to investigate both theoretically and experimentally phenomena associated with radiation fronts for the experimentally realistic situation of ionizing or dissociating radiation, passing through a transparent window into a tube containing the absorbing gas.

Five different types of steady radiation fronts may occur for the experimental situation under consideration. At one extreme of high radiation intensity and low particle density there is little particle motion associated with the front; at the other extreme of relatively low intensities and high particle densities the particle motion is dominant and a shock front propagates ahead of the radiation front. The speed of the various discontinuities and all thermodynamic quantities may be calculated either if the detailed structure of the radiation front and mechanisms occurring within it are known or if the temperature behind the radiation front is assumed. Conversely a measurement of this temperature would yield important information about these mechanisms.

It was shown that for the case of no recombination or collisional dissociation, the structure of a steady

radiation front produced by monochromatic radiation could be described by a simple analytical expression in terms of Lagrangian co-ordinates. This expression depends only on the absorber density and on the absorption coefficient, α . A simple relativistic correction must be made if the velocity of the radiation front is near that of light; this causes an apparent steepening of the front.

A treatment of the structure of a dissociation front in oxygen for a simplified reaction scheme was outlined. It was pointed out that, in general, it is necessary to consider all the reactions within the radiation front. A numerical solution was attempted for a weak D-type front preceded by a Mach 3 shock but was unsuccessful.

For an experimental investigation of radiation fronts an intense pulsed light source, which consists of an arc discharge through a narrow channel in polyethylene, was constructed. The average intensity of this "Bogen" light source (in a solid angle of 0.1 sterad, at 5000 Å and operated at a discharge voltage of 3.0 kV) was measured to be $(1.9 \pm 0.2) \times 10^3$ times as bright as a standard carbon arc. Along the axis the intensity is about three times larger than this value. This indicates that the effective black body temperature of the source is from 60,000 °K to 150,000 °K.

Experiments were carried out at low and high absorber densities, N_0 . An experiment in iodine at a low density, N_0 , illustrated the beginning of the formation of a radiation

front. Although the measurements were quite crude the agreement with theory was quite reasonable. The author suggests a similar type of experiment be attempted with a strong d.c. light source.

Shock fronts in oxygen at a high density, N_0 , were detected by means of piezoelectric pressure probes. At high pressures (1 atm) the shocks formed very near the lithium fluoride window, while at low pressures (0.03 atm) the point of formation was about one cm from the window. The speed of propagation of the shocks was 364 ± 8 m/sec for all pressures, at least at distances far from the LiF window.

Attempts to detect photoionization in the test chamber showed only that photons in the wavelength region from 1200 \AA to 2000 \AA were especially efficient in knocking out electrons from brass or dielectric material. Attempts to detect ionization fronts proved fruitless.

It was shown how the development of a radiation front may be considered as unsteady one-dimensional flow with energy input and treated by the method of characteristics at constant time intervals or by the method of finite differences. These theories were applied to calculate the evolution of the shocks which were observed in oxygen. The theoretical results agreed well with the experimental results. It was also pointed out that if sufficient computer time were available and a constant energy input were

used, these methods could be used to obtain steady state solutions. (complete with thermodynamic quantities, velocities and the front structure) which we had attempted to calculate previously. It had been hoped that it would be possible to compare the results of such a calculation with the structure obtained by the method outlined in Chapter 4 (an attempt at which proved unsuccessful). Since this was not practicable the author hopes that he has at least pointed out a possible mode of attack for future work in this field.

In conclusion, the author would like to point out that future work in this field depends upon the development of extremely intense sources of radiation both d.c. and pulsed. The author can only dream in anticipation of a gigawatt laser, radiating for tens of microseconds and adjustable to any frequency desired.

A P P E N D I X A

NUMERICAL CALCULATION OF A STEADY RADIATION

FRONT IN OXYGEN

The programme used to calculate the structure of an idealized radiation front in oxygen for a black body spectrum $F(\nu)$ and absorption cross section $\alpha(\nu)$ (see section 3.1.2) is given below. For the calculations we use the photoabsorption cross section between 1280 \AA and 1800 \AA as given by Metzger and Cook, Fig. B.3, Appendix B and assume a frequency distribution of a black body source at $6 \times 10^4 \text{ }^\circ\text{K}$ as given in eq'ns (4.10) and eq'n (D.7), Appendix D.

First the total photon flux is calculated by Simpson's rule and then standard Runge-Kutta subroutine is applied to eq'ns (3.21) and (3.24) to calculate the photon flux, F/F_0 and co-ordinate x , at selected intervals Δz . The initial value of $x = 0$ is chosen arbitrarily at a point where $F/F_0 \approx \frac{1}{2}$. The terminology in the programme is as follows: $h\nu/kT = \xi \rightarrow X$; $x \rightarrow Y(2)$; $z \rightarrow Y(1)$; and $\Delta z \rightarrow DZ$.

\$JOB 79296 ROB MORRIS

\$FORTRAN

C IDEALIZED RADIATION FRONT FOR BLACK BODY RADIATION AT 60000 KELVIN

C CORRESPONDING TO WEAK R-TYPE DISSOCIATION FRONT IN OXYGEN

C --- USING RUNGA-KUTTA SUBROUTINE

DIMENSION Y(10),F(10),Q(10)

COMMON FJ,FW,DX,A(21),X(21),FO(21)

DATA A/0.00251,0.00871,0.0274,0.0498,0.1070,0.1890,0.301,
10.416,0.548,0.672,0.784,0.894,0.963,1.0,0.985,0.894,

2 0.647,0.221,0.0746,0.0498,0.03737

T=6.0

X(1)=8.0/T

DX=0.16/T

DO 10 I=1,20

10 X(I+1)=X(I)+DX

DO 11 I=1,21

11 FO(I)=(X(I)*X(I))/(EXP(X(I))-1.0)

FOT=FO(1)-FO(21)

DO 12 K=1,10

12 FOT=FOT+4.0*FO(2*K)+2.0*FO(2*K+1)

FW=FOT*DX/3.0

WRITE (6,60) FW

60 FORMAT(1X,10E12.4)

DZ=-0.06

DO 2 J=1,2

Y(1)=4.518876

Y(2)=0.0

DO 1 I=1,75

CALL RK(Y,F,Q,DZ,2,1)

1 WRITE (6,60) Y(1),Y(2), FJ

2 DZ=-2.0*DZ

STOP

END

SUBROUTINE AUX RK(Y,F)

COMMON FJ,FW,DX,A(21),X(21),FO(21)

DIMENSION Y(10),F(10),FY(21)

DO 21 I=1,21

21 FY(I)=FO(I)*(EXP(-A(I)*Y(1)))

FYT=FY(1)-FY(21)

DO 22 K=1,10

22 FYT=FYT+4.0*FY(2*K)+2.0*FY(2*K+1)

FZ=FYT*DX/3.0

FJ=FZ/FW

F(2)=1.0/(1.0-FJ)

RETURN

END
\$ENTRY

7
5
9
7
8
6
10
11
12
↑

↓
12
11
10
9
8
7
6
5
4
3

A P P E N D I X B

Fig.B.1 Scale drawing of Bogen light source consisting of cylindrically symmetric electrodes separated by epoxy and strengthened with fibreglass.

Figs.B.2 and B.3 Absorption cross sections for iodine and oxygen reproduced directly from the literature.

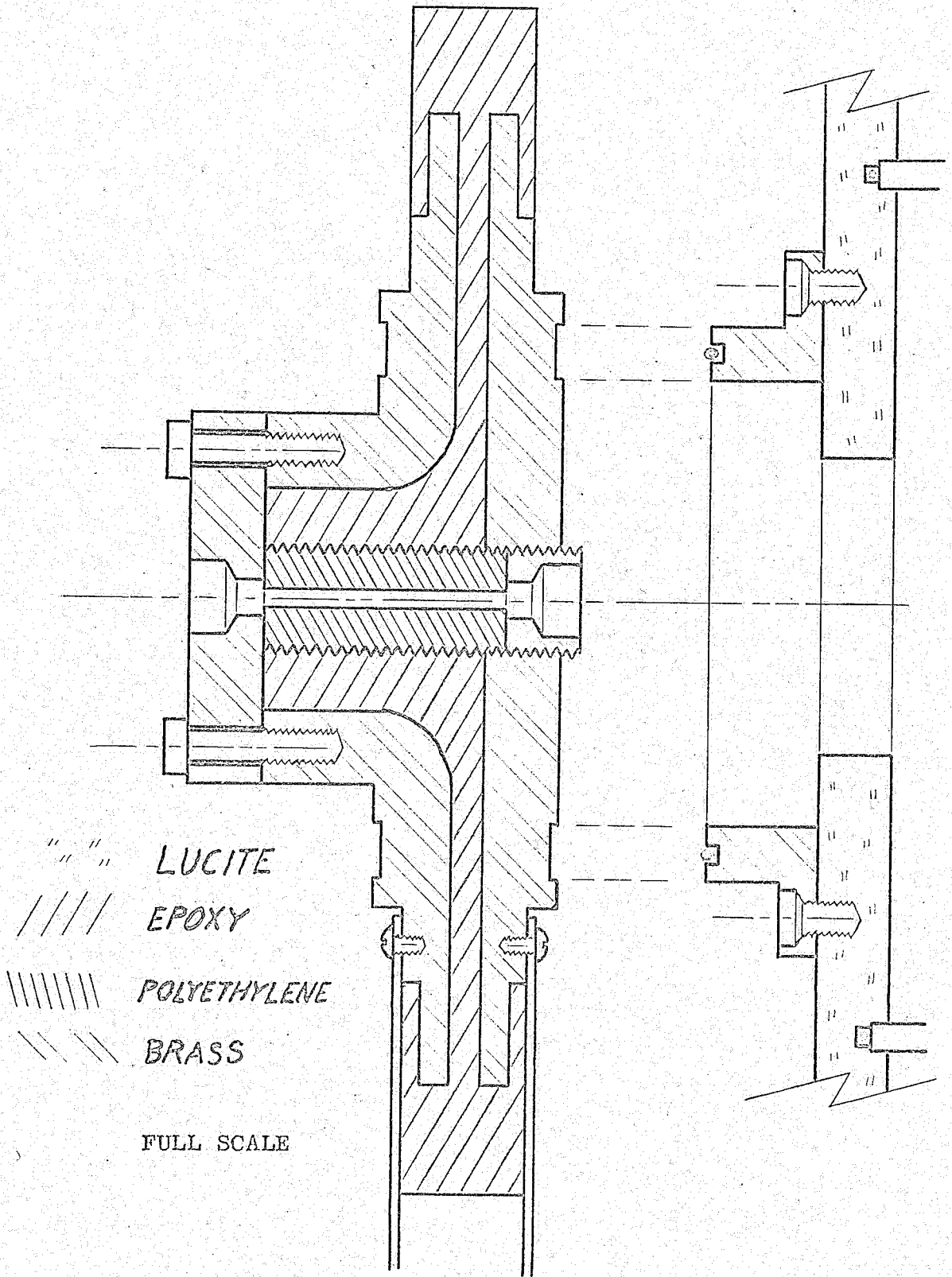


Fig. B.1 Scale drawing of Bogen light source.

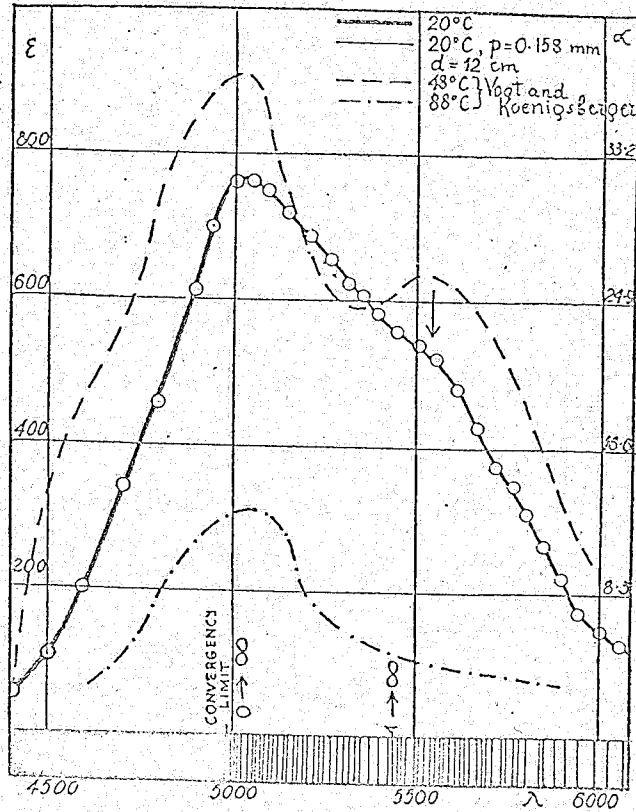


FIG. 1.—Extinction-curves of iodine vapour.

Fig.B.2 Iodine absorption cross sections (Rabinowitch and Wood (1936))

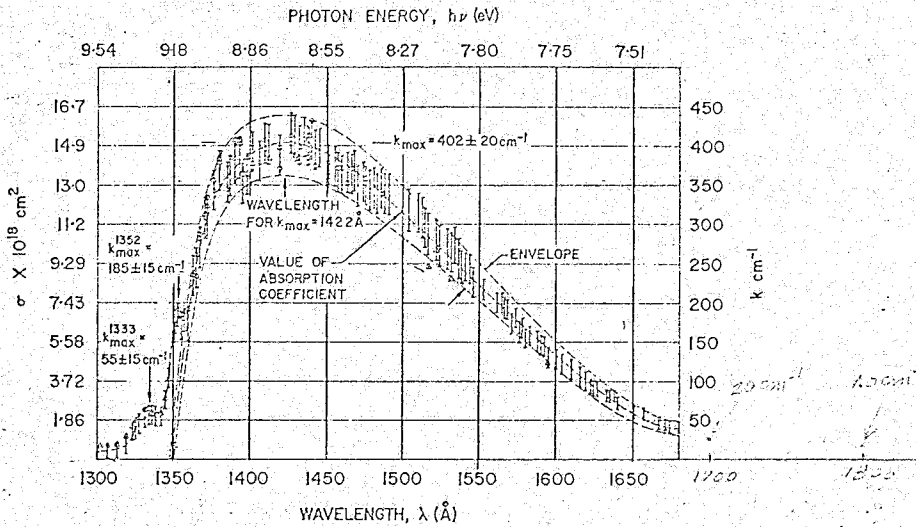


FIG. 6. O_2 absorption. A few examples of results obtained by the first and second arrangements are indicated by circles and triangles.

Fig.B.3 Oxygen absorption cross sections (Metzger and Cook (1964))

A P P E N D I X C

EQUATIONS FOR SPECIAL REACTION SCHEME

The reaction eq'ns (4.5) are written to indicate different groups of particles (O atoms, O₂ molecules, O₃ molecules, O₂* molecules). We can write one conservation equation for each group. The equations corresponding to eq'n (4.8) in the simplified case considered in Chapter 4 (using the subscripts i = 1, 2, 3, 4 to indicate O, O₂, O₃, O₂* particles respectively) are

$$\begin{aligned} \frac{\partial N_1}{\partial t} + \frac{\partial (u N_1)}{\partial x} = & 0 + 2 \left. \frac{\partial F}{\partial x} \right|_{2 \rightarrow 1} + 2 \left. \frac{\partial F}{\partial x} \right|_{4 \rightarrow 1} + \left. \frac{\partial F}{\partial x} \right|_{3 \rightarrow 1+4} \\ & + \sum_i k_{di} N_4 N_i - \sum_i k_{ri} N_i^2 N_i \\ & - \sum_i k_{ri} N_1 N_2 N_i - \sum_i k_{ri} N_1 N_4 N_i \quad , \quad \text{C.1} \end{aligned}$$

$$\begin{aligned} \frac{\partial N_2}{\partial t} + \frac{\partial (u N_2)}{\partial x} = & - \left. \frac{\partial F}{\partial x} \right|_{2 \rightarrow 1} - \left. \frac{\partial F}{\partial x} \right|_{2 \rightarrow 4} \\ & - \sum_i k_i N_2 N_i + \sum_i k_i N_4 N_i \\ & - \sum_i k_{ri} N_1 N_2 N_i \quad , \quad \text{C.2} \end{aligned}$$

$$\begin{aligned} \frac{\partial N_3}{\partial t} + \frac{\partial (u N_3)}{\partial x} = & - \left. \frac{\partial F}{\partial x} \right|_{3 \rightarrow 1+4} \\ & + \sum_i k_{ri} N_1 N_2 N_i + \sum_i k_{ri} N_1 N_4 N_i \quad , \quad \text{C.3} \end{aligned}$$

the vibrational and translational degrees of freedom were in equilibrium. Furthermore in such a case it would be necessary to use a photoabsorption cross section which had been measured as a function of wavelength and as a function of temperature (i.e. the photoabsorption cross section would be temperature dependent).

As for the simplified case treated in Chapter 4, the energy input for each group of particles may be obtained directly from eq'ns (C.7) to (C.10) (see eq'ns (4.18) and (4.19)). Thus we obtain

$$P_{g_1} = 0$$

C.13

$$P_{g_2} = P(g_2^1 + g_2^4) = N_2 \int_V (\alpha_2^1(\nu) + \alpha_2^4(\nu)) h\nu F(\nu, 0, t) e^{-\int_0^x \sum_i \alpha_i N_i dx} dV,$$

C.14

$$P_{g_3} = N_3 \int_V \alpha_3(\nu) h\nu F(\nu, 0, t) e^{-\int_0^x \sum_i \alpha_i N_i dx} dV,$$

C.15

$$P_{g_4} = N_4 \int_V \alpha_4(\nu) h\nu F(\nu, 0, t) e^{-\int_0^x \sum_i \alpha_i N_i dx} dV,$$

C.16

where $P_{g_1} = 0$ since $\alpha_1(\nu) = 0$. The total rate of energy input is simply the sum of these individual contributions

$$P(x, t) g(x, t) = P(x, t) (g_1 + g_2 + g_3 + g_4). \quad C.17$$

This treatment of the more general reaction scheme in eq'n (4.5) indicates that it is necessary to consider all the intermediate steps in a chain reaction process. In general the energy flux contributing to the front is larger than if these steps were ignored, because the intermediate

particles absorb photons in a different part of the energy spectrum than the initial pure gas.

A P P E N D I X D

METHOD OF CHARACTERISTICS AT FIXED TIME INTERVALS

An excellent treatment of the equations of unsteady flow with no energy input by the method of characteristics is given by Hoskins (1964) in a form directly applicable for calculations on a computer. Here, we will extend Hoskin's treatment to include energy input.

Fig. D.1 shows the typical mesh in Lagrangian space and time. In order to determine conditions at the

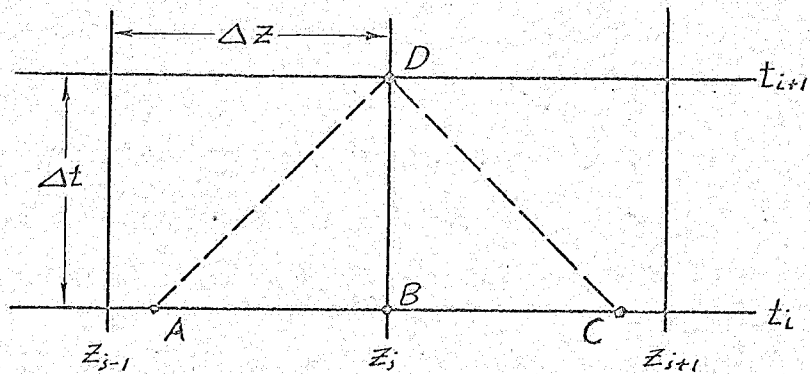


Fig. D.1 Calculation of an ordinary point D.

point D on the t_{i+1} baseline we require values of the flow variables at A and B on the t_i baseline which may be obtained by linear or quadratic interpolation between the known values at z_{j-1} , z_j and z_{j+1} . The equations to be solved as given in section 1 of Chapter 7 may be written in dimensionless units by making the

substitutions

$$\bar{Z} = \alpha_m \frac{\rho_0}{M} z$$

$$\bar{t} = \alpha_m \frac{\rho_0}{M} c_0 t$$

for the length and time dimensions, where α_m is some convenient reference cross section as defined following eq'n (3.20). The velocities are made dimensionless by dividing by the speed of sound in oxygen at 300 °K, $c_0 = 330$ m/sec. The thermodynamic quantities are made dimensionless by dividing by their initial values at $t = 0$. Thus,

$$\bar{P} = p/p_0, \quad \bar{\rho} = \rho/\rho_0, \quad \bar{h} = h/h_0, \quad \bar{u} = u/c_0, \quad \bar{c} = c/c_0.$$

The rate of energy input q is made dimensionless with respect to the equation in which it occurs. Since the effective adiabatic exponent g is already dimensionless we use $g_0 = 1.4$.

These dimensionless equations may be written in finite difference form. Eq'ns (7.11) and (7.3) evaluated along the Mach lines are written

$$(P_D - P_A) + g_0 [P_C]_{AD} (u_D - u_A) = \frac{\Delta t}{g_0 - 1} \left[(g-1) \rho g \right]_{AD} + \left[\frac{P}{g-1} \right]_{AD} (g_D - g_A) \quad \text{D.1}$$

$$(Z_D - Z_A) = [P_C]_{AD} \Delta t \quad \text{D.2}$$

$$(P_D - P_C) - g_0 [P_C]_{CD} (u_D - u_C) = \frac{\Delta t}{g_0 - 1} \left[(g-1) \rho g \right]_{CD} + \left[\frac{P}{g-1} \right]_{CD} (g_D - g_C)$$

$$(Z_D - Z_C) = - [P_C]_{CD} \Delta t \quad \text{D.3}$$

D.4

Along the pathline BD, eq'ns (7.5) and (7.4) are

$$(h_0 - h_B) = \left(\frac{g_0 - 1}{g_0}\right) \left[\frac{1}{P}\right]_{BD} (P_0 - P_B) + \left[\frac{\Delta t}{g_0}\right] [\delta]_{BD} \quad \text{D.5}$$

$$Z_0 = Z_B \quad \text{D.6}$$

The rate of energy input corresponding to eq'n (4.19') is

$$q = G(t) g_0 (g_0 - 1) * \text{CONS} * (1 - \gamma) \frac{\int_{s_1}^{s_2} \frac{A(s) s^3}{e^s - 1} e^{-A(s) \int_0^z (1 - \gamma) dz} dz}{\int_{s_1}^{s_2} \frac{s^3}{e^s - 1} ds} \quad \text{D.7}$$

where

$$\text{CONS} = \frac{E_0}{\rho_0 c_0^3}, \quad \text{D.7'}$$

and where we have used $s = h \nu / kt$, $A(s) = \alpha(s) / \alpha_m$, E_0 is the energy flux entering the gas as defined in eq'n (4.18), $G(t)$ is the dimensionless time dependence of the energy flux normalized (in our case) such that $E_0 = E_{\max}$ when $G(t) = 1.0$.

The conservation equation for O_2 particles (or dissociation equation) as given by eq'n (4.14) may be evaluated along a pathline to be

$$\frac{\partial N}{\partial t} = \left(\frac{M F_0}{\rho_0 c_0}\right) (1 - \gamma) \frac{\int_{s_1}^{s_2} A(s) \frac{s^2}{e^s - 1} e^{-A(s) \int_0^z (1 - \gamma) dz} dz}{\int_{s_1}^{s_2} \frac{s^2}{e^s - 1} ds} + \left(\frac{\rho_0 h_{d2}}{M}\right) (P) [(1 - \gamma)(1 + 5\gamma)] - \left(\frac{\rho_0^2 h_{d2}}{M^2}\right) (P^2) [(4\gamma^2)(1 + 5\gamma)], \quad \text{D.8}$$

where we have substituted for k_{df} and k_{r1} from eq'n (4.17). In this equation M is the mass of the oxygen molecule and F_0 is the photon flux entering the gas. Substituting from eq'n (4.17) for k_{d2} and k_{r2} eq'n(D.8) becomes

$$\frac{dy}{dz} = G(z) * AONS * (1-y) \frac{\int_{s_1}^{s_2} A(s) \frac{s^2}{e^s - 1} e^{-A(s)} \int_0^z (1-y) dz ds}{\int_{s_1}^{s_2} \frac{s^2}{e^s - 1} ds} + BONS * \left(\frac{p e^{-198/T}}{T^{3/2}} \right) [(1-y)(1+5y)] - DONS * \left(\frac{p^2}{T} \right) [4y^2(1+5y)] \quad D.9$$

where the temperature $T \rightarrow \bar{T} = T/T_0 = T/300$ °K and where AONS, BONS and DONS are

$$AONS \equiv \frac{MF_0}{\rho_0 C_0} = \frac{M C_0^2}{\langle h\nu \rangle} * CONS \quad D.10$$

$$BONS \equiv \left(\frac{3.06 \times 10^{-3}}{\alpha_m C_0 T^{3/2}} \right) \quad D.11$$

$$DONS \equiv \left(\frac{\rho_0 * 4.4 \times 10^{-30}}{M \alpha_m C_0 T_0} \right) \quad D.12$$

The equation of state relates the various thermodynamic quantities

$$V \equiv \frac{1}{\rho} = \frac{\rho_0}{\rho_0 - 1} \left(\frac{\rho - 1}{\rho} \right) \frac{h}{\rho} \quad D.13$$

$$T = \left(\frac{1}{1+y} \right) \frac{p}{\rho} \quad D.14$$

where

$$y = 1 + \frac{1+y}{\left(\frac{5}{2} + \frac{1}{2}y \right) + (1-y) \left(\frac{743}{T} \right) \left(e^{\frac{743}{T}} - 1 \right)^{-1} + 198 \left(\frac{y}{T} \right)} \quad D.15$$

Finally the speed of sound and the position in Eulerian co-ordinates are

$$c = \left[\frac{1}{\gamma_0 - 1} (\gamma - 1) h \right]^{\frac{1}{2}} \quad \text{D.16}$$

and

$$x_D = x_B + [u]_{BD} \Delta t \quad \text{D.17}$$

The procedure for obtaining a solution at the point D is to calculate approximate values of y_D and q_D from eq'ns (D.8) and (D.7). Next one calculates u_D and p_D from eq'ns (D.1) and (D.3) (using values of the thermodynamic quantities at points A and C which are located approximately from eq'ns (D.2) and (D.4)). Next one calculates h_D , g_D , ρ_D , T_D from eq'ns (D.5), (D.15), (D.13) and (D.14) respectively.

Finally c_D is obtained from eq'n (D.16). Using these calculated values the whole iterative procedure is repeated until all the quantities have converged to the desired accuracy. Finally the position x_D is obtained from eq'n (D.17).

The point of formation of a shock is located by calculating the point where the right flowing Mach lines first intersect. The shocks may be treated according to the procedure outlined by Hoskin (1964).

For the case of no energy input, the choice of the difference intervals Δt and Δz depends upon how well a straight line approximates the actual curved Mach lines (i.e. upon the relative change in the variables across these

intervals). If energy input is included then we have an additional constraint in that the interval Δz must be small enough such that the energy absorbed in the interval is small compared to the energy incident upon it (i.e. such that straight line segments may be used to approximate the exponential-like decay curves, see Fig. 3.3). From practical experience we found that it is best to use $\Delta t = \frac{1}{2} \Delta z$ (in dimensionless units) and also that the product $\Delta z * \text{CONS}$ should not exceed 10.

The procedure outlined above was used in section 7.3.1 to calculate the development of the shock fronts observed experimentally in oxygen in section 6.2. The calculations were carried out for initial pressure of 1.0 atm and 0.1 atm. The peak photon flux was assumed to be 1.16×10^{22} ph/520 Å cm²sec and the time variation was taken to simulate the shape of the Bogen light pulse.

The values of the constants and difference intervals which were used for each case were:

<u>1.0 atm</u>	<u>0.1 atm</u>
$f_0/M = 1.69 \times 10^{19} \text{ cm}^{-3}$	$f_0/M = 1.69 \times 10^{18} \text{ cm}^{-3}$
AONS = 0.0131	AONS = 0.131
BONS = 0.1195×10^7	BONS = 0.1195×10^7
CONS = 3.0	CONS = 30.0
DONS = 0.80	DONS = 0.08
$\Delta t = 1.32 \rightarrow (0.1 \text{ } \mu\text{sec})$	$\Delta t = 0.264 \rightarrow (0.2 \text{ } \mu\text{sec})$
$\Delta z = 2.64 \rightarrow (0.00657 \text{ cm})$	$\Delta z = 1.056 \rightarrow (0.0263 \text{ cm})$

The computer programme used in the calculations is given on the following pages. The symbols used correspond to the terminology used above except for the following: temperature, $T \rightarrow H$; $h \neq /kT \approx \mathcal{J} \rightarrow S$; density, $\rho \rightarrow R$; effective adiabatic exponent, $g \rightarrow GAM$; enthalpy, $h \rightarrow HH$; time, $t \rightarrow T$; $\Delta t \rightarrow D$; $\Delta z \rightarrow DZ$; Eulerian spatial co-ordinate, $x \rightarrow X$. The symbols XX , UU and CC refer to the position, particle velocity and speed of sound of \mathcal{N} (right flowing) Mach lines.

ADDENDUM: In section 7.1.1 we stated that for calculations in this thesis we would neglect the term $(\partial g / \partial t)_z$ in eq'n (7.11). It was found that this resulted in the calculated density being consistently too high (violating the principle of conservation of mass). To overcome this difficulty we were forced to include this term. As shown in eq'ns (D.1) and (D.3) we assumed that $(\Delta g)_z$ at the midpoint of the Mach lines AD and CD was equal to $(\Delta g)_z = (g_D - g_B)$ along the pathline BD (see Fig. 7.1).

\$PAUSE MOUNT TAPE
\$JOB 79087 H.A.BALDIS
\$PAGE 100
\$TIME 10

\$IBFTC MAIN

C METHOD OF CHARACTERISTICS AT FIXED TIME INTERVALS

C PRESSURE=0.1 ATM

C F FROM BOGEN LIGHT SOURCE

DIMENSION SAM(8,65, 8),DX(20),XMIN(20)

DIMENSION S(21),FO(21),FL(21),FY(21),FYL(21),A(21)

DATA A/0.00251,0.00871,0.0274,0.0498,0.1070,0.1890,0.301,
10.416,0.548,0.672,0.784,0.894,0.963,1.0,0.985,0.894,

2 0.647,0.221,0.0746,0.0498,0.0373/

TW=6.0

S(1)=8.0/TW

DS=0.16/TW

DO 10 I=1,20

10 S(I+1)=S(I)+DS

DO 11 I=1,21

FL(I)=(S(I)*S(I))/(EXP(S(I))-1.0)

11 FO(I)=S(I)*FL(I)

FLT=FL(1)-FL(21)

FOT=FO(1)-FO(21)

DO 12 K=1,10

FLT=FLT+4.0*FL(2*K)+2.0*FL(2*K+1)

12 FOT=FOT+4.0*FO(2*K)+2.0*FO(2*K+1)

FWL=FLT*DS/3.0

FW=FOT*DS/3.0

60 FORMAT (1X,7E12.4)

WRITE(6,60) FW,FWL

DIMENSION X(99,3),U(99,3),Y(99,3),V(99,3),R(99,3),P(99,3),C(99,3),

1 H(99,3),Q(99,3),HH(99,3),GAM(99,3),XX(99,3),UU(99,3),CU(99,3)

DATA X(1,1),U(1,1),Y(1,1),V(1,1),R(1,1),P(1,1),H(1,1),HH(1,1),

9 XX(1,1),UU(1,1),CU(1,1),C(1,1),GAM(1,1)/

8 0.0,0.0,0.0,1.0,1.0,1.0,1.0,1.0,0.0,0.0,1.0,1.0,1.4/

DATA M,L/65,80/

Q(1,1)=0.0

M1=M-1

M2=M-2

AONS=0.131

BONS=0.1195E+07

CONS=30.0

DONS=0.080

DT=0.264

DZ=1.056

DZA=0.528

DO 1 I=1,M

U(I+1,1)=U(I,1)

Y(I+1,1)=Y(I,1)

Q(I+1,1)=Q(I,1)

V(I+1,1)=V(I,1)

R(I+1,1)=R(I,1)

P(I+1,1)=P(I,1)

H(I+1,1)=H(I,1)

C(I+1,1)=C(I,1)

HH(I+1,1)=HH(I,1)

UU(I+1,1)=UU(I,1)

CU(I+1,1)=CU(I,1)

GAM(I+1,1)=GAM(I,1)

XX(I+1,1)=XX(I,1)+DZ

1 X(I+1,1)=X(I,1)+DZ

DIMENSION GT(29),TT(29),G(100),T(100),T5(100)

DATA GT/0.0,.0484,.0968,.219,.387,.580,.813,.981,1.0,.990,

1 .968,.935,.903,.865,.826,.739,.658,.583,.516,.462,

2 .426,.387,.355,.332,.313,.200,.1096,.0452,0.0/

DATA TT/0.0,2.64,5.28,7.92,10.56,13.20,15.84,18.48,21.12,23.76,

1 26.40,29.04,31.68,34.32,36.96,42.24,47.52,52.80,58.08,63.36,

2 68.64,73.92,79.20,84.48,89.76,116.16,142.56,168.96,195.36/

G(1)=0.0

T(1)=0.0

T5(1)=0.0

ATM=0.1

DO 554 J=2,29

554 T5(J)=ATM*TT(J)

DO 557 I=2,L

T(I)=T(I-1)+DT

DO 556 J=2,29

555 IF (T(I).GE.T5(J)) GO TO 556

G(I)=GT(J)-(T5(J)-T(I))*(GT(J)-GT(J-1))/(T5(J)-T5(J-1))

GO TO 557

556 G(I)=0.0

557 CONTINUE

LLL=L/10

DO 3 NN=1,LLL

DO 3 NM=1,10

N=NM+(NN-1)*10

DO 4 J=1,M

GAM(J,2)=GAM(J,1)

U(J,2)=U(J,1)

C(J,2)=C(J,1)

4
5
6
7
8
9
10
11

```
R(J,2)=R(J,1)
V(J,2)=V(J,1)
H(J,2)=H(J,1)
P(J,2)=P(J,1)
CA=C(J,1)
CC=CA
NUMB=I
Y(J,2)=Y(J,1)
100 CONTINUE
VT=0.5*(V(J,2)+V(J,1))
HT=0.5*(H(J,2)+H(J,1))
HEX=198.0/HT
IF (HEX.GT.88.0) GO TO 88
HTV=(EXP(-HEX))/(VT*HT**1.5)
GO TO 89
HTV=0.0
88 HTW=1.0/(HT*VT*VT)
89 YI=0.5*(Y(J,2)+Y(J,1))
YI=1.0-YI
YTV=YI*(1.0+5.0*YI)
YTW=4.0*YI*YI*(1.0+5.0*YI)
IF ('J.NE.I') GO TO 888
ZIN=0.0
ZON=0.0
GO TO 889
888 ZON=ZOM+(1.0-0.5*(Y(J,2)+Y(J-1,2)))*DZ
889 ZIN=ZIM+(1.0-0.25*(Y(J,2)+Y(J-1,2)+Y(J,1)+Y(J-1,1)))*DZ
DO 21 I=1,21
AEX=A(I)*EXP(-A(I)*ZIN)
AOX=A(I)*EXP(-A(I)*ZON)
FYL(I)=FL(I)*AEX
FY(I)=FO(I)*AOX
FYLT=FYL(I)-FYL(21)
FYT=FY(I)-FY(21)
DO 22 K=1,10
FYL=FYL+4.0*FYL(2*K)+2.0*FYL(2*K+1)
FYT=FYT+4.0*FY(2*K)+2.0*FY(2*K+1)
FI=YI*FYLT*DS/(3.0*FWL)
YYYY=Y(J,2)
GTN=0.5*(G(N)+G(N-1))
Y(J,2)=Y(J,1) +DI*(AONS*GIN *FI+BONS*Hiv*Yiv-DONS*Hiw*Yiw)
FJ=(1.0-Y(J,2))*FY*DS/(3.0*FW)
Q(J,2)=0.56*CONS*FJ*G(N)
999 UUUU=U(J,2)
IF (J.EQ.1) GO TO 76
```

1
2
3
4
5
6
7
8
9
10
11
12

```

AAR=0.25*(CA+C(J,2))*(R(J,1)-R(J-1,1))*DI/DZ
RA=(R(J,1)-R(J,2))*AAR/(1.0+AAR)
AAC=0.25*(RA+R(J,2))*(C(J,1)-C(J-1,1))*DI/DZ
CA=(C(J,1)-C(J,2))*AAC/(1.0+AAC)
RR=0.5*(RA+R(J,2))
CR=0.5*(CA+C(J,2))
DZA=RR*CR*DI/DZ
PA=P(J,1)-DZA*(P(J,1)-P(J-1,1))
UA=U(J,1)-DZA*(U(J,1)-U(J-1,1))
QA=Q(J,1)-DZA*(Q(J,1)-Q(J-1,1))
GAMA=GAM(J,1)-DZA*(GAM(J,1)-GAM(J-1,1))
QR=0.5*(QA+Q(J,2))
PR=0.5*(PA+P(J,2))
GAMR=0.5*(GAMA+GAM(J,2))
PGQR=PA+2.5*(GAMR-1.0)*RR*QR*DI+PR*(GAM(J,2)-GAM(J,1))/(GAMR-1.0)
IF (J.EQ.M) GO TO 78
76 CCR=0.25*(CC+C(J,2))*(R(J,1)-R(J+1,1))*DI/DZ
RC=(R(J,1)-R(J,2))*CCR/(1.0+CCR)
CCC=0.25*(RC+R(J,2))*(C(J,1)-C(J+1,1))*DI/DZ
CC=(C(J,1)-C(J,2))*CCC/(1.0+CCC)
RL=0.5*(RC+R(J,2))
CL=0.5*(CC+C(J,2))
DZC=RL*CL*DI/DZ
PC=P(J,1)-DZC*(P(J,1)-P(J+1,1))
UC=U(J,1)-DZC*(U(J,1)-U(J+1,1))
QC=Q(J,1)-DZC*(Q(J,1)-Q(J+1,1))
GAMC=GAM(J,1)-DZC*(GAM(J,1)-GAM(J+1,1))
QL=0.5*(QC+Q(J,2))
PL=0.5*(PC+P(J,2))
GAML=0.5*(GAMC+GAM(J,2))
PGQL=PC+2.5*(GAML-1.0)*RL*QL*DI+PL*(GAM(J,2)-GAM(J,1))/(GAML-1.0)
IF (J.EQ.1) GO TO 77
U(J,2)=(RR*CR*UA+RL*CL*UC+(PGQR-PGQL)/1.4)/(RR*CR+RL*CL)
78 IF (J.EQ.M) U(J,2)=0.5*(U(J-1,2)+U(J,1))
PRR=PGQR-1.4*RR*CR*(U(J,2)-UA)
PLL=PGQL+1.4*RL*CL*(U(J,2)-UC)
IF (J.EQ.M) PLL=PRR
IF (J.EQ.1) PRR=PLL
P(J,2)=0.5*(PRR+PLL)
QT=0.5*(Q(J,2)+Q(J,1))
NUMC=1
VT=0.5*(V(J,2)+V(J,1))
HH(J,2)=HH(J,1)+VT*(P(J,2)-P(J,1))/3.5+QT*DI/1.4
EVIB=7.43/H(J,2)*(EXP(7.43/H(J,2))-1.0)
GA=2.5+0.5*Y(J,2)+(1.0-Y(J,2))*EVIB+198.0*Y(J,2)/H(J,2)

```

101

GAM(J,2)=1.0+(1.0+Y(J,2))/GA
V(J,2)=3.5*(GAM(J,2)-1.0)*HH(J,2)/(GAM(J,2)*P(J,2))
R(J,2)=1.0/V(J,2)

H(J,2)=P(J,2)*V(J,2)/(1.0+Y(J,2))

NUMC=NUMC+1

IF (NUMC.LE.2) GO TO 101

CCCC=C(J,2)

C(J,2)=SQRT((GAM(J,2)-1.0)*HH(J,2)/0.4)

NUMB=NUMB+1

IF (ABS(U(J,2)-UUUU).GT..001*U(J,2)) GO TO 100

IF (ABS(Y(J,2)-YYYY).GT..001*Y(J,2)) GO TO 100

IF (ABS(C(J,2)-CCCC).GT..001*C(J,2)) GO TO 100

X(J,2)=X(J,1)+0.5*(U(J,2)+U(J,1))*DT

ZOM=ZON

ZIM=ZIN

4 CONTINUE

DO 86 K=1,M1

XX(K,2)=XX(K,1)+(UU(K,1)+CU(K,1))*DT

DO 82 JJ=1,M

82 IF(X(JJ,2).GT.XX(K,2)) GO TO 83

DO 84 I=1,M2

LL=M-I

UU(LL,2)=UU(LL-1,2)

CU(LL,2)=CU(LL-1,2)

84 XX(LL,2)=XX(LL-1,2)

UU(1,2)=0.0

CU(1,2)=C(1,2)

XX(1,2)=0.0

GO TO 86

83 XF=X(JJ,2)

XE=X(JJ-1,2)

XFE=XF-XE

UF=U(JJ,2)

UE=U(JJ-1,2)

UFE=UF-UE

CF=C(JJ,2)

CE=C(JJ-1,2)

CFE=CF-CE

BES=0.5*DT*(UFE+CFE)/XFE

CES=0.5*DT*(UU(K,1)+CU(K,1)+UE+CE)

XX(K,2)=(XX(K,1)+CES-BES*XE)/(1.0-BES)

TXX=(XX(K,2)-XE)/(XF-XE)

UU(K,2)=UE+TXX*UFE

CU(K,2)=CE+TXX*CFE

86 CONTINUE

```

61  FORMAT (1X,11E11.4)
62  FORMAT (1X,I6)
    WRITE (6,62) N
    WRITE (6,61) (U(I,2),C(I,2),X(I,2),Y(I,2),Q(I,2),P(I,2),R(I,2),
1    H(I,2),HH(I,2),GAM(I,2),XX(I,2),I=1,M1)
    RNM=NM
    IF(RNM-10.)70,71,71
71  DO 72 I=1,M
    SAM(NN,I,1)=X(I,2)
    SAM(NN,I,2)=U(I,2)
    SAM(NN,I,3)=P(I,2)
    SAM(NN,I,4)=Y(I,2)
    SAM(NN,I,5)=Q(I,2)
    SAM(NN,I,6)=R(I,2)
    SAM(NN,I,7)=H(I,2)
72  SAM(NN,I,8)=GAM(I,2)
70  CONTINUE
    DO 32 I=1,M
    Y(I,3)=Y(I,1)
32  Q(I,3)=Q(I,1)
    DO 33 I=1,M
    X(I,1)=X(I,2)
    U(I,1)=U(I,2)
    Y(I,1)=Y(I,2)
    V(I,1)=V(I,2)
    R(I,1)=R(I,2)
    P(I,1)=P(I,2)
    Q(I,1)=Q(I,2)
    H(I,1)=H(I,2)
    HH(I,1)=HH(I,2)
33  GAM(I,1)=GAM(I,2)
    DO 34 I=1,M1
    XX(I,1)=XX(I,2)
12  UU(I,1)=UU(I,2)
11  CU(I,1)=CU(I,2)
10  34
9    3
8    CONTINUE
7    WRITE(7)SAM
6    CALL PLOTS
5    M8=M*8
4    CALL SCALE(SAM(1,1,1),M8,10.,XMIN(1),DX(1),1)
3    DO 200 I=2,8
    CALL SCALE(SAM(1,1,I),M8,6.0,XMIN(I),DX(I),1)
    CALL AXIS(0.,0,0.,1HX,-1.9,0.,0.,XMIN(I),DX(I))
    CALL AXIS(0.,0.,1H , 0,6.,90.,XMIN(I),DX(I))
    DO 201 J=1,8

```

```
CALL PLOT(SAM(J,1,I),SAM(J,1,I),+3)
DO 202 K=1,M
202 CALL PLOT(SAM(J,K,1),SAM(J,K,I),+2)
201 CONTINUE
CALL PLOT(12.0,0.0,-3)
200 CONTINUE
CALL PLOTND
STOP
END
$ENTRY
```

5
9
7
8
6
10
11
12
↑
10

12
11
10
9
8
7
6
5
4
3

A P P E N D I X E

METHOD OF FINITE DIFFERENCES

The method of finite differences to calculate fluid flow in one space variable is illustrated in Fig. E.1. The general procedure is to calculate the state of the fluid at

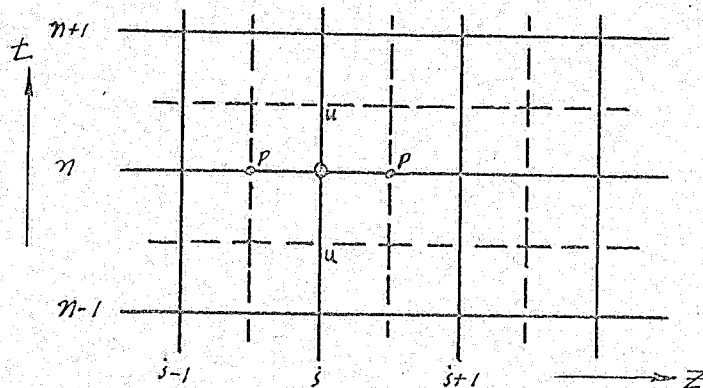


Fig. E.1 Lagrangian mesh for finite difference calculations

constant time t_0 in each cell in the z direction with special techniques being employed at the beginning and end of the interval. One then repeats the procedure at intervals of time Δt . Each cycle depends upon quantities calculated during the preceding cycle. Thus the state and dynamics of the gas can be calculated as a function of z (or x) at any time, t .

The procedure which we describe below is similar to that described by Richtmyer and Morton (1967), Chapter 12, (together with comments on "centering", stability criteria,

etc.) and a potential user should refer to this reference before attempting to use it. Since our equations contain the rate of energy input q and our centering is slightly different from that of Richtmeyer and Morton and we present these equations in difference form in dimensionless units. (These equations are very similar to those presented in Appendix D.) They are:

$$\frac{U_j^{n+1} - U_j^n}{\Delta t} = \left(-\frac{1}{g_0}\right) \left(\frac{P_{j+\frac{1}{2}}^{n+\frac{1}{2}} - P_{j-\frac{1}{2}}^{n+\frac{1}{2}} + QS_{j+\frac{1}{2}}^n - QS_{j-\frac{1}{2}}^n}{\Delta z} \right) \quad \text{E.1 (a)}$$

$$U_i^{n+1} = 0 \quad \text{E.1 (b)}$$

$$\frac{X_j^{n+1} - X_j^n}{\Delta t} = U_j^{n+\frac{1}{2}} \quad \text{E.2}$$

$$V_{j+\frac{1}{2}}^{n+1} = \frac{X_{j+1}^{n+1} - X_j^{n+1}}{\Delta z} \quad \text{E.3}$$

$$\frac{Y_{j+\frac{1}{2}}^{n+1} - Y_{j+\frac{1}{2}}^n}{\Delta t} = \text{ADNS} * G^{n+\frac{1}{2}} * (1 - Y_{j+\frac{1}{2}}^{n+\frac{1}{2}}) \frac{\int_{s_1}^{s_2} \frac{d(s)}{e^{s-1}} e^{-\lambda(s) \int_0^z (1 - Y_{j+\frac{1}{2}}^{n+\frac{1}{2}}) dz} ds}{\int_{s_1}^{s_2} \frac{s^2}{e^{s-1}} ds} \quad \text{E.4}$$

$$+ \text{BONS} * \left(\frac{\text{EXP}(-198.0 / T_{j+\frac{1}{2}}^{n+\frac{1}{2}})}{(T_{j+\frac{1}{2}}^{n+\frac{1}{2}})^{\frac{3}{2}} V_{j+\frac{1}{2}}^{n+\frac{1}{2}}} \right) \left[(1 - Y_{j+\frac{1}{2}}^{n+\frac{1}{2}}) (1 + 5.0 * V_{j+\frac{1}{2}}^{n+\frac{1}{2}}) \right]$$

$$- \text{DNS} * \frac{1}{(T_{j+\frac{1}{2}}^{n+\frac{1}{2}}) (V_{j+\frac{1}{2}}^{n+\frac{1}{2}})^2} \left[4.0 * (Y_{j+\frac{1}{2}}^{n+\frac{1}{2}})^2 (1.0 + 5.0 * Y_{j+\frac{1}{2}}^{n+\frac{1}{2}}) \right],$$

$$Q_{j+\frac{1}{2}}^{n+\frac{1}{2}} = g_0 (g_0 - 1) * \text{CONS} * G^{n+\frac{1}{2}} * (1.0 - Y_{j+\frac{1}{2}}^{n+\frac{1}{2}}) \frac{\int_{s_1}^{s_2} \frac{d(s)}{e^{s-1}} e^{-\lambda(s) \int_0^z (1 - Y_{j+\frac{1}{2}}^{n+\frac{1}{2}}) dz} ds}{\int_{s_1}^{s_2} \frac{s^3}{e^{s-1}} ds} \quad \text{E.5}$$

$$(E_{j+\frac{1}{2}}^{n+1} - E_{j+\frac{1}{2}}^n) = -(g_0 - 1) (P_{j+\frac{1}{2}}^{n+\frac{1}{2}} + QS_{j+\frac{1}{2}}^n) (V_{j+\frac{1}{2}}^{n+1} - V_{j+\frac{1}{2}}^n) + Q_{j+\frac{1}{2}}^{n+\frac{1}{2}} \Delta t \quad \text{E.6}$$

$$P_{j+\frac{1}{2}}^{n+1} = \left(\frac{1}{g_0 - 1} \right) \left(\frac{E_{j+\frac{1}{2}}^{n+1}}{V_{j+\frac{1}{2}}^{n+1}} \right) \left[\frac{(1.0 + Y_{j+\frac{1}{2}}^{n+1})}{(2.5 + 0.5 Y_{j+\frac{1}{2}}^{n+1}) + (1.0 - Y_{j+\frac{1}{2}}^{n+1}) \left(\frac{7.43}{T_{j+\frac{1}{2}}^{n+1}} \right) \left(\text{EXP}(7.43/T_{j+\frac{1}{2}}^{n+1}) - 1 \right)^{-1}} + 198.0 \left(\frac{V_{j+\frac{1}{2}}^{n+1}}{T_{j+\frac{1}{2}}^{n+1}} \right) \right]$$

$$T_{j+\frac{1}{2}}^{n+1} = \frac{P_{j+\frac{1}{2}}^{n+1} V_{j+\frac{1}{2}}^{n+1}}{1.0 + Y_{j+\frac{1}{2}}^{n+1}} \quad \text{E.7}$$

$$QS_{j+\frac{1}{2}}^n = \frac{g_0 * AA * (U_{i+1}^n - U_i^n)^2}{V_i^n} \quad \text{if } (U_{i+1}^n - U_i^n) < 0 \quad \text{E.8}$$

$$= 0 \quad \text{if } (U_{i+1}^n - U_i^n) \geq 0 \quad \text{E.9}$$

The various constants found in these equations are defined in Appendix D. The superscript $n + \frac{1}{2}$ indicates an average value (e.g. $P_{j+\frac{1}{2}}^{n+\frac{1}{2}} = 0.5(P_{j+\frac{1}{2}}^{n+1} + P_{j+\frac{1}{2}}^n)$). On the other hand the subscript $j + \frac{1}{2}$ does not indicate an average value; it implies that the value of P is calculated in the middle of the interval between j and j + 1 (see Fig. E.1).

The calculation procedure used is as follows:

1. Calculate U_j^{n+1} and X_j^{n+1} from eq'n's (E.1) and (E.2) for all values of j (using a special procedure at both ends).
2. Calculate V_j^{n+1} (appearing as $V(J-1, 2)$ in programme) from eq'n (E.3)
3. Calculate Y_j^{n+1} from eq'n (E.4) using approximate or average values for Y_j^n , T_j^n , $V_{j+\frac{1}{2}}^{n+\frac{1}{2}}$. A special procedure is needed for $\int_{j_1}^{j_2} (\quad) d\delta$.

4. Calculate $Q_{j+\frac{1}{2}}^n$ from eq'n (E.5). (Note Q is calculated in the middle of the time interval.)
5. Calculate $E_{j+\frac{1}{2}}^n$ from eq'n (E.6).
6. Use an iterative procedure to calculate $P_{j+\frac{1}{2}}^n$ and $H_{j+\frac{1}{2}}^n$ from eq'ns (E.7) and (E.8)
7. Repeat steps 2 to 6 for all values of j .
8. If necessary (because of instabilities or to shorten the number of iterations required) calculate weighted values of $P_{j+\frac{1}{2}}^n$ and $H_{j+\frac{1}{2}}^n$ (i.e. average or weigh the results of step 6 with those obtained in a previous iteration).
9. Check the self-consistency of the results obtained and if there is insufficient accuracy, store the values and return to step 1.
10. If sufficient accuracy is obtained calculate $QS_{j+\frac{1}{2}}^n$ for all values of j .
11. Increase time index and return to step 1.

We have not examined the stability criteria for our case in detail. In general, however, we find that the increase in the variables per Δt interval should not exceed about 30% (even in this case we are not sure about the accuracy of the results since we use a large value for the artificial viscosity).

The procedure outlined above was used in section 7.3.2 in an attempt to simulate the development of a steady weak D-type front preceded by a Mach 3 shock. The conditions for this case were the same as used in Fig. 3.6 ---

initial pressure of 0.01 atm and a photon flux, $F_0 = 4.72 \times 10^{21}$ photons/cm²sec for which the various constants were

$$\text{AONS} = 0.532$$

$$\text{BONS} = 0.1195 \times 10^7$$

$$\text{CONS} = 121.8$$

$$\text{DONS} = 0.008$$

$$\text{DT} = 0.04$$

$$\text{DZ} = 0.08$$

The value of $a^2 = 8$ was chosen for the numerical constant appearing in the artificial viscosity, see eq'n (7.12).

The computer programme used for these calculations is given on the following pages. Most of the symbols used in the programme are virtually the same as used in Appendix D. The artificial viscosity is $Q_s \rightarrow QS$ and $a^2 \rightarrow AA$.

```
$PAUSE MOUNT TAPE
$JOB 79296 ROB MORRIS
$PAGE 100
$TIME 10
```

```
$IBFTC MAIN
```

```
C METHOD OF FINITE DIFFERENCES
```

```
C PRESSURE=0.01 ATM
```

```
C WEAK D-TYPE + MACH 3 SHOCK
```

```
DIMENSION SAM ( 5,80, 8),DX(20),XMIN(20)
```

```
DIMENSION S(21),FO(21),FL(21),FY(21),FYL(21),A(21)
```

```
DATA A/0.00251,0.00871,0.0274,0.0498,0.1070,0.1890,0.301,
10.416,0.548,0.672,0.784,0.894,0.963,1.0,0.985,0.894,
```

```
2 0.647,0.221,0.0746,0.0498,0.0373/
```

```
TW=6.0
```

```
S(1)=8.0/TW
```

```
DS=0.16/TW
```

```
10 DO 10 I=1,20
```

```
S(I+1)=S(I)+DS
```

```
DO 11 I=1,21
```

```
FL(I)=(S(I)*S(I))/(EXP(S(I))-1.0)
```

```
11 FO(I)=S(I)*FL(I)
```

```
FLT=FL(1)-FL(21)
```

```
FOT=FO(1)-FO(21)
```

```
DO 12 K=1,10
```

```
FLT=FLT+4.0*FL(2*K)+2.0*FL(2*K+1)
```

```
12 FOT=FOT+4.0*FO(2*K)+2.0*FO(2*K+1)
```

```
FWL=FLT*DS/3.0
```

```
FW=FOT*DS/3.0
```

```
60 FORMAT (1X,7E12.4)
```

```
WRITE(6,60) FW,FWL
```

```
DIMENSION X(90,3),U(90,3),Y(90,3),V(90,3),E(90,3),P(90,3),
```

```
1 H(90,3),Q(90,3),QS(90,3)
```

```
12 DATA X(1,1),U(1,1),Y(1,1),V(1,1),E(1,1),P(1,1),H(1,1)/
```

```
9 0.0,0.0,0.0,1.0,1.0,1.0,1.0/
```

```
10 DATA M,L/80,50/
```

```
9 AONS=0.532
```

```
8 BONS=0.1195E+07
```

```
7 CONS=121.8
```

```
6 DONS=0.008
```

```
5 G=1.0
```

```
4 DT=0.04
```

```
3 DZ=0.08
```

```
AA=8.0
```

```
QS(1,1)=0.0
```

```
DO 1 I=1,M
```

9
7
8
6
01
11
12
↑

```

U(I+1,1)=U(I,1)
Y(I+1,1)=Y(I,1)
V(I+1,1)=V(I,1)
E(I+1,1)=E(I,1)
P(I+1,1)=P(I,1)
H(I+1,1)=H(I,1)
QS(I+1,1)=QS(I,1)
1 X(I+1,1)=X(I,1)+DZ
  LLL=L/10
  DO 3 NN=1,LLL
  DO 3 NM=1,10
  N=NM+(NN-1)*10
  X(1,2)=0.0
  U(1,2)=0.0
  NUMB=1
  DO 4 J=2,M
  Y(J-1,2)=Y(J-1,1)
  H(J-1,2)=H(J-1,1)
  P(J-1,2)=P(J-1,1)
  M1=M-1
  100 DO 5 J=2,M1
  PL=0.5*(P(J-1,2)+P(J-1,1))
  PR=0.5*(P(J,2)+P(J,1))
  U(J,2)=U(J,1)-(PR-PL+QS(J,1)-QS(J-1,1))*DI/(1.4*DZ)
  IF (NUMB.NE.1) U(J,2)=(U(J,2)+U(J,3))*0.5
  5 X(J,2)=X(J,1)+(U(J,2)+U(J,1))*DI*0.5
  U(M,2)=1.5*U(M-1,2)-0.5*U(M-2,2)
  X(M,2)=X(M,1)+0.5*(U(M,2)+U(M,1))*DI
  DO 6 J=2,M
  V(J-1,2)=(X(J,2)-X(J-1,2))/DZ
  HT=0.5*(H(J-1,2)+H(J-1,1))
  VT=0.5*(V(J-1,2)+V(J-1,1))
  PT=0.5*(P(J-1,2)+P(J-1,1))+QS(J-1,1)
  HEX=198.0/HT
  IF (HEX.GT.88.0) GO TO 88
  HTV=(EXP(-HEX))/(VT*HT**1.5)
  GO TO 89
  88 HTV=0.0
  89 HTW=1.0/(HT*VT*VT)
  NUMC=1
  IF (NUMC.GE.4) GO TO 104
  YT=0.5*(Y(J-1,2)+Y(J-1,1))
  102 YI=1.0-YT
  YTV=YI*(1.0+5.0*YT)
  YTW=4.0*YT*YT*(1.0+5.0*YT)

```

12
11
10
9
8
7
6
5
4
3

```

ZINT=-0.5*YI
DO 7 I=2,J
7 ZINT=ZINT+1.0-0.5*(Y(I-1,2)+Y(I-1,1))
ZIN=ZINT*DZ
DO 21 I=1,21
21 AEX=A(I)*(EXP(-A(I)*ZIN))
FYL(I)=FL(I)*AEX
FY(I)=FO(I)*AEX
FYLT=FYL(1)-FYL(21)
FYT=FY(1)-FY(21)
DO 22 K=1,10
22 FYLT=FYLT+4.0*FYL(2*K)+2.0*FYL(2*K+1)
FYT=FYT+4.0*FY(2*K)+2.0*FY(2*K+1)
FI=YI*FYL*DS/(3.0*FWL)
Y(J-1,2)=Y(J-1,1)+DT*(AONS*G *FI+BONS*HTV*YTV-DONS*HIW*YTW)
NUMC=NUMC+1
FJ=YI*FYT*DS/(3.0*FW)
Q(J-1,2)=0.56*CONS*FJ*G
104 E(J-1,2)=E(J-1,1)-0.4*PI*(V(J-1,2)-V(J-1,1))+Q(J-1,2)*DI
NUMD=1
103 EVI=2.96*(1.0-Y(J-1,2))/(EXP(7.43/H(J-1,2))-1.0)
GAN=E(J-1,2)-EVI-78.5*Y(J-1,2)
P(J-1,2)=(1.0+Y(J-1,2))*GAN/(V(J-1,2)*(1.0+0.2*Y(J-1,2)))
H(J-1,2)=P(J-1,2)*V(J-1,2)/(1.0+Y(J-1,2))
NUMD=NUMD+1
IF (NUMD.LE.2) GO TO 103
6 CONTINUE
974 IF (NUMB.LE.1) GO TO 31
DO 13 J=2,M
P(J-1,2)=0.5*(P(J-1,2)+P(J-1,3))
13 H(J-1,2)=0.5*(H(J-1,2)+H(J-1,3))
IF (NUMB.GE.10) GO TO 106
DO 8 I=2,M
8 IF (ABS(U(I,2))-U(I,3)).GT.0.01*U(I,2)) GO TO 31
IF (ABS(H(I-1,2))-H(I-1,3)).GT.0.001*H(I-1,2)) GO TO 31
106 DO 105 J=2,M
UQS=U(J,2)-U(J-1,2)
IF (UQS.LT.0.0) GO TO 105
UQS=0.0
105 QS(J-1,2)=1.4*AA*UQS*UQS/V(J-1,2)
Y(M,2)=Y(M1,2)
V(M,2)=V(M1,2)
E(M,2)=E(M1,2)
P(M,2)=P(M1,2)
H(M,2)=H(M1,2)

```

```

Q(M,2)=Q(M1,2)
QS(M,2)=QS(M1,2)
61  FORMAT (1X,9E12.4)
62  FORMAT (1X,2I6)
WRITE (6,62) N,NUMB
C   WRITE (6,61) (X(I,2),U(I,2),Y(I-1,2),V(I-1,2),E(I-1,2),P(I-1,2),
C   1   H(I-1,2),Q(I-1,2),QS(I-1,2), I=2,M)
RNM=NM
IF(RNM-10.)70,71,71
71  DO 72 I=1,M
    SAM(NN,I,1)=X(I,2)
    SAM(NN,I,2)=U(I,2)
    SAM(NN,I,3)=P(I,2)
    SAM(NN,I,4)=Y(I,2)
    SAM(NN,I,5)=Q(I,2)
    SAM(NN,I,6)=V(I,2)
    SAM(NN,I,7)=H(I,2)
72  SAM(NN,I,8)=E(I,2)
70  GO TO 32
31  DO 9 I=2,M
    U(I,3)=U(I,2)
    P(I-1,3)=P(I-1,2)
9   H(I-1,3)=H(I-1,2)
    NUMB=NUMB+1
    GO TO 100
32  DO 20 I=2,M
    X(I,1)=X(I,2)
    U(I,1)=U(I,2)
    Y(I-1,1)=Y(I-1,2)
    V(I-1,1)=V(I-1,2)
    E(I-1,1)=E(I-1,2)
    P(I-1,1)=P(I-1,2)
12  QS(I-1,1)=QS(I-1,2)
11  20 H(I-1,1)=H(I-1,2)
10  3  CONTINUE
9   WRITE (7) SAM
8   CALL PLOTS
7   M8=M*5
6   CALL SCALE(SAM(1,1,1),M8,10.,XMIN(1),DX(1),1)
5   DO 200 I=2,8
4   CALL SCALE(SAM(1,1,I),M8,6.0,XMIN(I),DX(I),1)
3   CALL AXIS (0.0,0.0,1HX,-1,10.,0.0,XMIN(1),DX(1))
    CALL AXIS(0.,0.,1H,0,6.,90.,XMIN(I),DX(I))
    DO 201 J=1,5
    CALL PLOT(SAM(J,1,1),SAM(J,1,I),+3)

```

9
7
8
6
01
11
12
↑
↓

```
DO 202 K=1,M
202 CALL PLOT(SAM(J,K,1),SAM(J,K,I),+2)
201 CONTINUE
CALL PLOT(12.0,0.0,-3)
200 CONTINUE
CALL PLOTND
STOP
END
$ENTRY
```

4
9
7
8
6
01
11
12
↑
13

12
11
10
9
8
7
6
5
4
3

BIBLIOGRAPHY

- Ahlborn, B., Phys. Fluids: 9, 1873 (1966)
- Ahlborn, B. and Salvat, M., Z. Naturforschg. 22 a, 260 (1967)
- Axford, W. I., Phil. Trans. R. Soc. London, A253, 301 (1961)
- Blackman, V., J. Fluid Mech. 1, 61-85 (1956)
- Camac, M., J. Chem. Phys. 34, 448 - 459 (1961)
- Camac, M., and Vaughan, A., J. Chem. Phys. 34, 460-470
- Chandrasekhar, S., "Radiative Transfer", Dover Publication, New York (1960)
- Courant, R., and Friedrichs, K.O., "Supersonic Flow and Shock Waves", Interscience, New York (1948).
- Elton, R. C., Plasma Phys. (J.Nuc.En.Part C) 6, 401 (1964)
- Goldsworthy, F.A., Phil. Trans. R. Soc. London, A253, 277 (1961)
- Hoskin, N. E., Methods in Computational Physics 3, 265 (1964)
- Hurle, I. R., Reports on Prog. Phys. xxx, 149 (1967)
- Kahn, F. D., B.A.N., 12, 187 (1954)
- Kuthe, R., and Neumann, Kl.K., Ber Bunsenges Phys. Chemi. 68, 692 (1964)
- Landolt - Börnstein (1950) II.4, p 717
- Lun'kin, Yu.P., Soviet Phys. - Techn. Phys. 4, 155 (1959)
- Mathews, D. L., Phys. Fluids 2, 170 - 178 (1959)
- Metzger, P. H., and Cook, G. R., J. Quant. Spec. Rad. Trans. 4, 107 (1964)
- Mises, R. v., "Mathematical Theory of Compressible Fluid Flow", Academic Press N.Y. (1958)

- Null, M. R., and Lozier, W. W., J. Opt. Soc. Am. 52, 1156
(1962)
- Oswatitsch, K., "Gas Dynamics", Academic Press, New York
(1957)
- Panarella, E., and Savic, P., Can. J. Phys. 46, 183
(1968)
- Porter, G., and Smith, J., Proc. Roy. Soc. 261, 28 (1961)
- Rabinowitch, E., and Wood, W. D., Trans. Faraday Soc. 32,
540 (1936)
- Ramsden, S. A., and Savic, P., Nature 203, 1217 - 1219
(1964)
- Richmyer, R. D., and Morton, K. W., "Difference Methods
for Initial Value Problems", 2nd ed. Interscience
Publishers, New York (1967)
- Rink, J. P., Knight, H. T., Duff, R. E., J. Chem. Phys. 34,
1942 - 1947 (1961)
- Schwarz, W. M., "Intermediate Electromagnetic Theory", John
Wiley and Sons, New York, (1964)
- Shapiro, A. H., "The Dynamics and Thermodynamics of
Compressible Fluid Flow", Ronald Press Co.,
New York (1954)
- Zel'dovich, Ya. B., and Raizer, Yu. P., "Physics of Shock
Waves and High-Temperature Hydrodynamic Phenomena",
Academic Press, New York (1966)